OSU

The Ohio State University

AN E-PLANE ANALYSIS OF APERTURE-MATCHED HORN ANTENNAS USING THE MOMENT METHOD AND THE UNIFORM GEOMETRICAL THEORY OF DIFFRACTION

D.J. Heedy
W.D. Burnside

The Ohio State University

ElectroScience Laboratory

Department of Electrical Engineering
Columbus, Ohio 43212

Technical Report 716148-1
Grant No. NSG 1613
September 1984

National Aeronautics and Space Administration
Langley Research Center
Hampton, Virginia 23665

NOTICES

When Government drawings, specifications, or other data are used for any purpose other than in connection with a definitely related Government procurement operation, the United States Government thereby incurs no responsibility nor any obligation whatsoever, and the fact that the Government may have formulated, furnished, or in any way supplied the said drawings, specifications, or other data, is not to be regarded by implication or otherwise as in any manner licensing the holder or any other person or corporation, or conveying any rights or permission to manufacture, use, or sell any patented invention that may in any way be related thereto.

50272-101

REPORT DOCUMENTATION PAGE	1. REPORT NO. 716148-1	2.	3. Recipient's Accession No.

4. Title and Subtitle

AN E-PLANE ANALYSIS OF APERTURE-MATCHED HORN ANTENNAS USING THE MOMENT METHOD AND THE UNIFORM GEOMETRICAL THEORY OF DIFFRACTION

5. Report Date September 1984

6.

7. Author(s) D.J. Heedy, W.D. Burnside

8. Performing Organization Rept. No. 716148-1

9. Performing Organization Name and Address

The Ohio State University
ElectroScience Laboratory
1320 Kinnear Road
Columbus, Ohio 43212

10. Project/Task/Work Unit No.

11. Contract(C) or Grant(G) No.

(C)

(G) NSG 1613

12. Sponsoring Organization Name and Address

National Aeronautics and Space Administration
Langley Research Center
Hampton, Virginia 23665

13. Type of Report & Period Covered Technical

14.

15. Supplementary Notes

16. Abstract (Limit: 200 words)

The moment method and the uniform geometrical theory of diffraction are utilized to obtain two separate solutions for the E-plane field pattern of an aperture-matched horn antenna. This particular horn antenna consists of a standard pyramidal horn with the folloiwng modifications: a rolled edge section attached to the aperture edges and a curved throat section. The resulting geometry provides significantly better performance in terms of the pattern, impedance, and frequency characteristics than normally obtainable. The moment method is used to calcualte the E-plane pattern and BSWR of the antenna. However, at higher frequencies, large amounts of computation time are required. The uniform geometrical theory of diffraction provides a quick and efficient high frequency solution for the E-plane field pattern. In fact, the uniform geometrical theory of diffraction may be used to initially design the antenna; then, the moment method may be applied to "fine tune" the design. This procedure has been successfully applied to a comapct range feed design.

17. Document Analysis a. Descriptors

b. Identifiers/Open-Ended Terms

c. COSATI Field/Group

18. Availability Statement	19. Security Class (This Report) UNCLASSIFIED	21. No. of Pages 105
	20. Security Class (This Page) UNCLASSIFIED	22. Price

(See ANSI-Z39.18) *See Instructions on Reverse*

OPTIONAL FORM 272 (4-77)
(Formerly NTIS-35)
Department of Commerce

TABLE OF CONTENTS

LIST OF TABLES

LIST OF FIGURES

Figure Page

CHAPTER I

INTRODUCTION

The use of horn antennas for feeds in compact range measurement systems and other applications creates a need for an efficient means of designing such antennas. Often it is desirable to do as much of the design work as possible "on paper" before constructing a physical model to test. Such an approach is usually cheaper and less time-consuming.

One may make use of one or more analytical techniques to obtain a fairly accurate idea of how closely the particular antenna design will meet the required specifications before building it. For example, aperture integration may be used to find the main beam of the field pattern but it requires a knowledge of the field distribution across the aperture. Unfortunately, the exact distribution cannot be determined without a physical model so an approximate distribution, such as the geometrical optics field, is normally used.

The moment method can provide an "exact" solution to the problem. An integral equation which the fields must satisfy is found. From this equation, a system of N simultaneous linear equations in N unknowns is obtained and solved using linear algebra techniques. Typically, these

N unknowns specify the current distribution associated with the body, and the result may be used to calculate the fields. For bodies which are large with respect to wavelength, the number of unknowns is large, and the computation time necessary to obtain a solution may become intolerable. Thus, the moment method is an excellent low frequency method. It can be used to analyze electrically large structures; however, it may require large amounts of computation time at the higher frequencies.

The uniform geometrical theory of diffraction is a good high frequency method which has the added advantage that it breaks down "gracefully" as the frequency decreases. This method modifies the geometrical optics solution by including a diffracted field such that the total field is smooth and continuous. A diffracted field may be associated with a discontinuity in the incident or reflected field as well as with a discontinuity in the rate of change or "slope" of the fields [1,2,3]. These discontinuities in the fields are the result of discontinuities in the extent or curvature of perfectly conducting bodies.

The uniform geometrical theory of diffraction (herewith referred to as UTD) can in many cases provide accurate results with relatively short computation time. For instance, it has been used to calculate both E-plane and H-plane patterns for the standard pyramidal horn [4,5,6] such as shown in Figure 1.

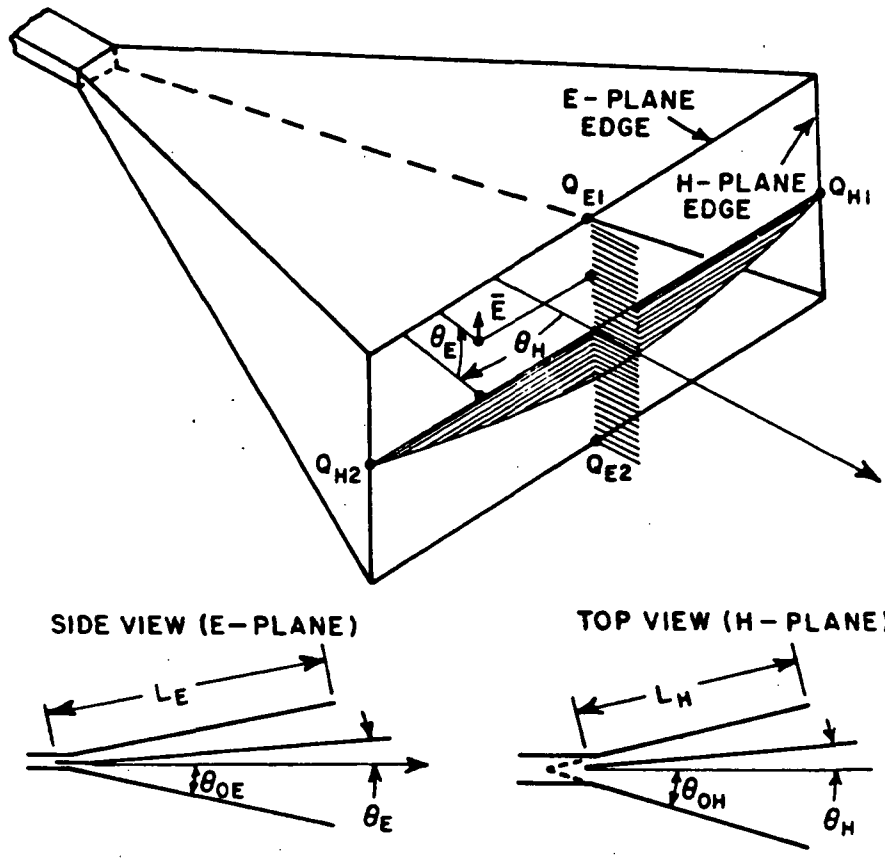

Figure 1. Pyramidal horn geometry.

In this report, an aperture-matched horn antenna with the geometry shown in Figure 2 is considered. In comparison to the standard pyramidal horn, the aperture-matched horn has a smoothly curved surface attached to the aperture edges. In this case the curved section is circular in shape, i.e., the radius of curvature is constant. Another curved section is added between the flared walls of the horn and waveguide junction. Thus, the sharp edges of the pyramidal horn are eliminated. The rolled edges allow much of the energy striking the edge to travel along the curved surface gradually shedding away from the surface into the sidelobe and backlobe regions. The result is a broader main beam with lower sidelobes and backlobes. In addition, the curved surfaces decrease the amount of energy reflected back into the throat of the horn resulting in a lower VSWR (voltage standing wave ratio). This property is important for feed horns in compact range systems where the antenna is used to transmit and/or receive.

The method of moments and the UTD are used to calculate the far field E-plane pattern of the aperture-matched horn antenna. The moment method may be conveniently used to find both E-plane and H-plane patterns at low frequencies when the horn dimensions are small with respect to wavelength. It may also be used at higher frequencies, but the computation time increases. The UTD solution discussed in this report provides good results for the E-plane pattern at higher frequencies with much less computation time. Thus, the pattern

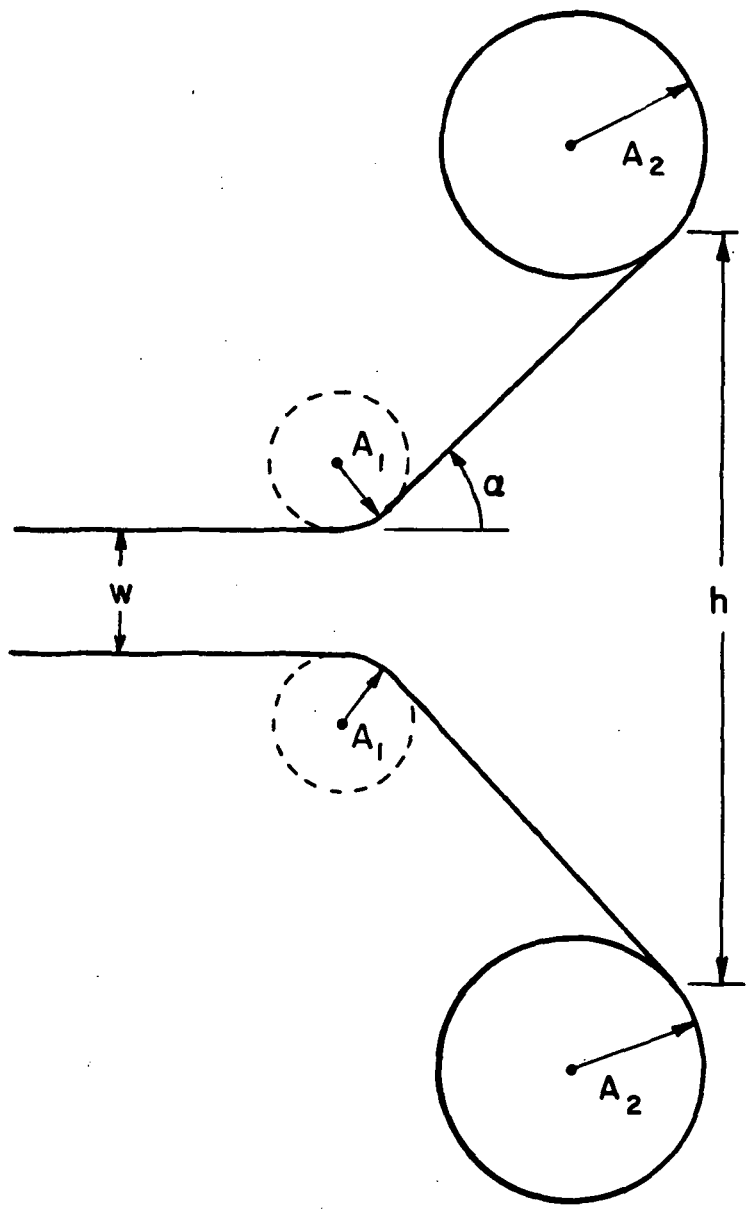

Figure 2. Aperture-matched horn geometry (E-plane side view).

behavior can be examined over a specified bandwidth. Also, the moment method solution is used to calculate the VSWR of the antenna.

Chapter II discusses the moment method solution for the E-plane pattern while Chapter III discusses the UTD solution for the E-plane pattern. In Chapter IV, a number of geometries are considered. The moment method and UTD solutions for the E-plane are compared and a brief analysis of the effects of changing various parameters of the horn geometry on the pattern and VSWR is made. Chapter V is a short summary with appropriate conclusions.

CHAPTER II

BACKGROUND AND THEORY FOR MOMENT METHOD SOLUTION

A moment method solution was obtained by using the reaction concept of Rumsey [7]. Consider the exterior scattering problem illustrated in Figures 3, 4, and 5. Impressed electric and magnetic currents $(\vec{J}_i, \vec{M}_i)$ generate electric and magnetic field intensities $(\vec{E}, \vec{H})$ in the presence of a conducting body in free space.

From the surface-equivalence theorem of Schellkunoff [8], an equivalent problem may be obtained by replacing the body by the following surface current densities:

$$\vec{J}_s = \hat{n} \times \vec{H} \tag{2.1}$$

and

$$\vec{M}_s = \vec{E} \times \hat{n} \tag{2.2}$$

where the unit vector $\hat{n}$ is the outward directed normal to the surface S. By definition, the source currents $(\vec{J}_i, \vec{M}_i)$ generate the incident fields $(\vec{E}_i, \vec{H}_i)$ in free space. The scattered fields are defined as

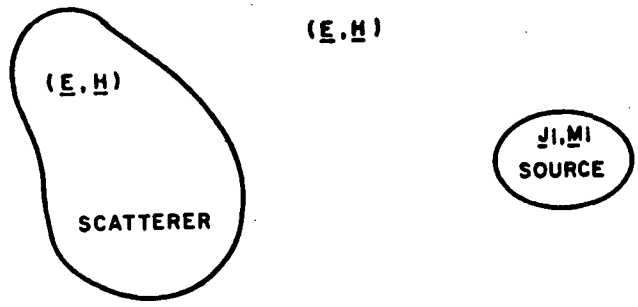

Figure 3. The source $(\vec{J}_i, \vec{M}_i)$ generates the field $(\vec{E}, \vec{H})$ with scatterer.

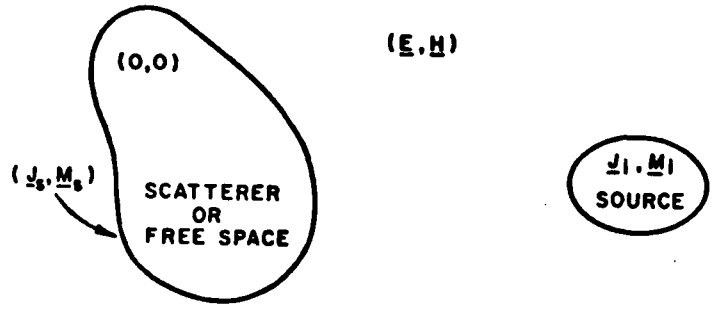

Figure 4. The interior field vanishes when the currents $(\vec{J}_S, \vec{M}_S)$ are introduced on the surface of the scatterer.

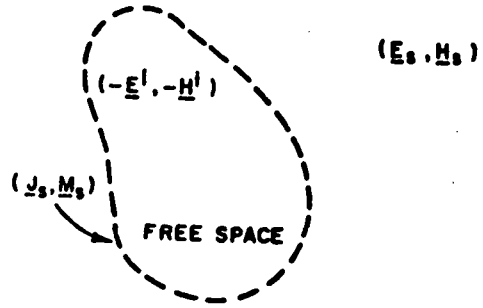

Figure 5. The exterior scattered field may be generated by $(\vec{J}_S, \vec{M}_S)$ in free space.

$$\vec{E}_s = \vec{E} - \vec{E}_i \tag{2.3}$$

and

$$\vec{H}_s = \vec{H} - \vec{H}_i \quad . \tag{2.4}$$

The surface currents generate the scattered fields $(\vec{E}_s, \vec{H}_s)$ exterior to the body and $(-\vec{E}_i, -\vec{H}_i)$ in the interior region.

One now places an electric test source $\vec{J}_m$ in this region as illustrated in Figure 6. Since there is a null field in the interior, the reaction of this test source with the fields of the other sources is zero. By reciprocity, this reaction is equivalent to the reaction of the remaining sources with the field of the test source such that

$$\iint(\vec{J}_s \cdot \vec{E}_m - \vec{M}_s \cdot \vec{H}_m)ds + \iiint(\vec{J}_i \cdot \vec{E}_m - \vec{M}_i \cdot \vec{H}_m)dv = 0 \tag{2.5}$$

where $(\vec{E}_m, \vec{H}_m)$ are the free space fields of the test source. This equation is a statement of the "zero-reaction theorem" of Rumsey [7] and is used to solve this problem.

Let us determine the surface current distributions $(\vec{J}_s, \vec{M}_s)$ from which the scattered fields may be calculated. To do this, one expands these functions in finite series with N unknown expansion coefficients. For our purposes, it is assumed that the body is a perfect conductor of electricity so that $\vec{M}_s$ vanishes. Let us also consider a two-dimensional problem in which $\vec{J}_s$ is only a function of the position ℓ around the

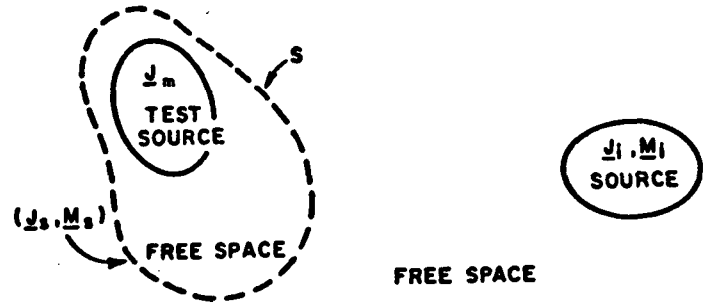

Figure 6. An electric test source $\vec{J}_m$ is positioned in the interior of the scattering region.

contour C of a cylinder. For the TE polarization in which the electric field is transverse to the z-axis, a magnetic line source is used and $\vec{J}_i$ is zero. The integral equation, Equation (2.5), becomes

$$\int_C \vec{J}_s \cdot \vec{E}_m \, d\ell = \iint \vec{M}_i \cdot \vec{H}_m \, ds \quad . \tag{2.6}$$

Let us represent the electric current distribution as

$$\vec{J}_s(\ell) = \sum_{n=1}^{N} I_n \vec{J}_n(\ell) \tag{2.7}$$

where the complex constants (I_n) are samples of the function $\vec{J}_s(\ell)$, and the vector basis functions are denoted by $\vec{J}_n(\ell)$. The test source and the basis functions have unit current density at their terminals.

Substituting Equation (2.7) into Equation (2.6), one obtains the following simultaneous linear equations:

$$\sum_{n=1}^{N} I_n Z_{mn} = V_m \quad \text{with } m = 1,2,3,\ldots N \tag{2.8}$$

where

$$Z_{mn} = -\int_n \vec{J}_n(\ell) \cdot \vec{E}_m d\ell = -\int_m \vec{J}_m(\ell) \cdot \vec{E}_n d\ell \tag{2.9}$$

$$V_m = -\int\int_i \vec{M}_i \cdot \vec{H}_m ds = \int_m \vec{J}_m(\ell) \cdot \vec{E}_i d\ell \tag{2.10}$$

and the integrations extend over the region where the integrand is non-zero.

For computational speed and storage, it is advantageous to have a symmetric impedance matrix Z_{mn}. Furthermore, the test sources should yield a well-conditioned set of simultaneous linear equations. For these reasons, and to obtain closed forms for some of the integrals in Equations (2.9) and (2.10), one uses test sources $\vec{J}_m$ of the same size, shape, and functional form as the expansion functions $\vec{J}_n$. Finally, the interior test sources are placed a small distance δ from the surface S and the limiting form of the integrals is taken as δ tends to zero.

For ease of computation, the basis functions are chosen to be sinusoidal strip dipoles. Such a planar strip dipole is illustrated in Figures 7 and 8. This dipole lies in the xz-plane and has infinite length in the z-direction. The surface-current density is

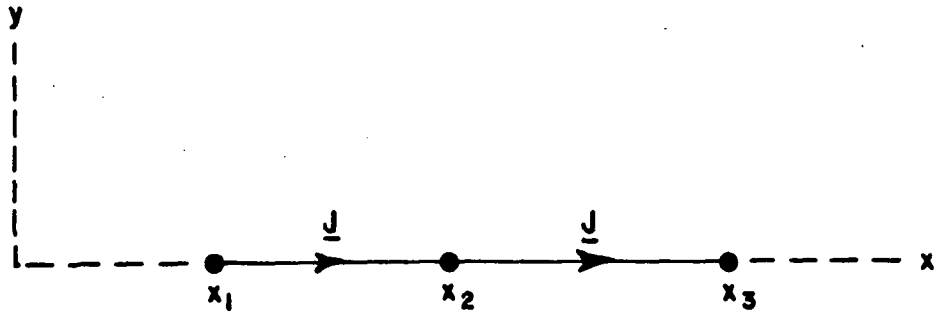

Figure 7. A planar strip dipole with edges at x_1 and x_3 and terminals at x_2.

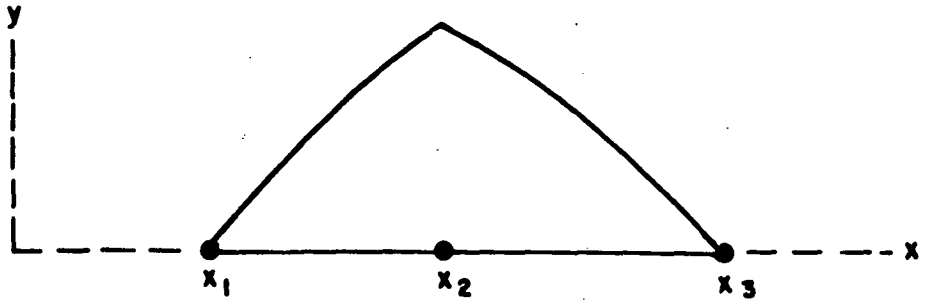

Figure 8. The current-density distribution $\vec{J}$ on the sinusoidal strip dipole.

$$\vec{J} = \hat{x}\,\frac{\sin(k(x-x_1))}{\sin(k(x_2-x_1))} \tag{2.11}$$

for $x_1 < x < x_2$, and

$$\vec{J} = \hat{x}\,\frac{\sin(k(x_3-x))}{\sin(k(x_3-x_2))} \tag{2.12}$$

for $x_2 < x < x_3$. Figure 9 illustrates a strip V-dipole. The distance along the dipole arms is measured by the coordinates s and t, respectively, with the origin at the terminals 0. The surface-current density is

$$\vec{J} = -\hat{s}\,\frac{\sin(k(s_1-s))}{\sin(ks_1)} \tag{2.13}$$

on arm s, and

$$\vec{J} = \hat{t}\,\frac{\sin(k(t_1-t))}{\sin(kt_1)} \tag{2.14}$$

on arm t. The unit vectors $\hat{s}$ and $\hat{t}$ are perpendicular to the z-axis. In both dipoles, the current density vanishes at the end points and is unity at the terminals 0. The current density is continuous across the terminals, but it does have a slope discontinuity there. Note that when $\psi = 180°$, the V-dipole reduces to the planar dipole.

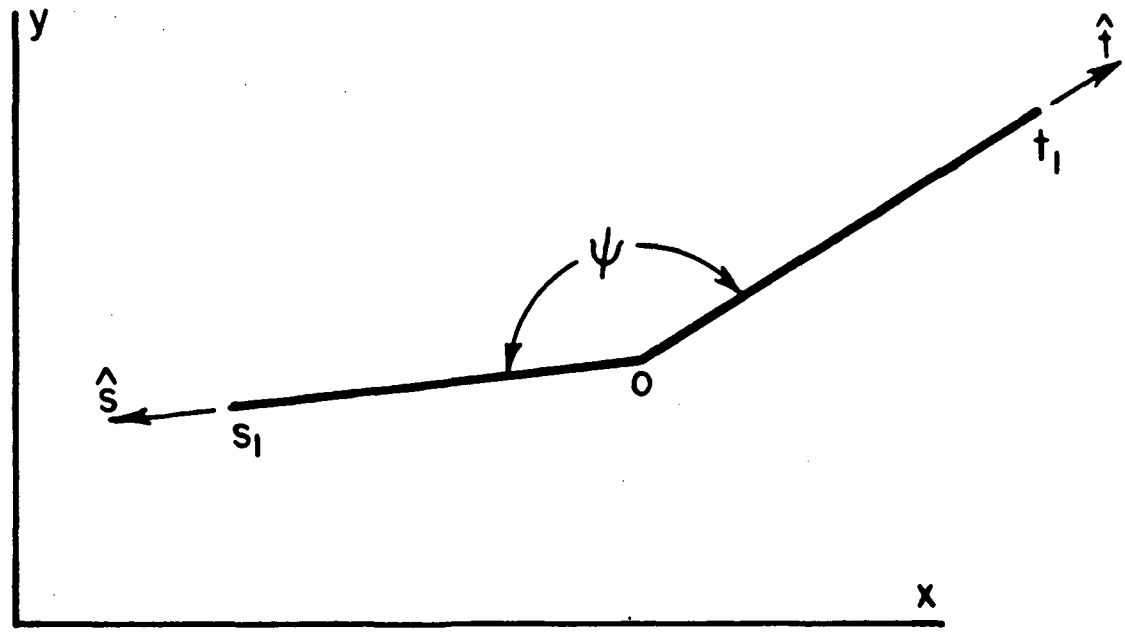

Figure 9. Nonplanar strip dipole with edges at s_1 and t_1 and terminals at 0.

The fields of the sinusoidal strip dipole may be obtained by considering the superposition of two strip monopoles with sinusoidal current distributions and a common end point. The fields of the strip monopole shown in Figure 10 are discussed in reference [9]. Using these results, let us calculate the various elements Z_{mn} of the impedance matrix and the elements V_m of the excitation column in Equation (2.8).

Consider a perfectly conducting polygon cylinder with contour C which may be open or closed. Let $\vec{J}_s(\ell)$ denote the surface-current density induced on the cylinder. In this case, the cylinder is open, so currents will flow on both sides of the thin conducting surface, and $\vec{J}_s$ will denote the total current density.

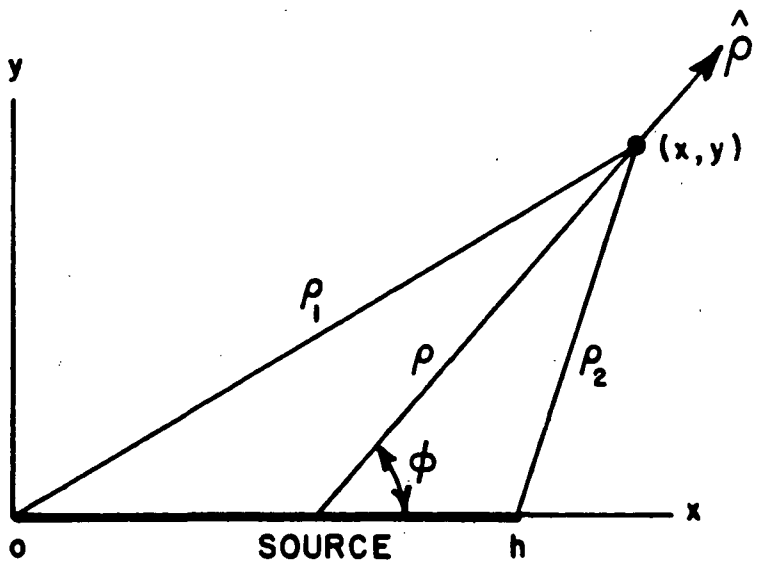

Figure 10. An electric strip monopole and the coordinate system.

Figure 11 illustrates a perfectly conducting polygon cylinder illuminated by a parallel magnetic line source $\vec{M}_i$. Let I_1 and I_2 denote the current density $\vec{J}_s$ at the corners of the polygon. The current density $\vec{J}_s$ vanishes at the edges 0 and 3. Let us define two strip dipole mode currents on the cylinder. Mode 1 extends from point 0 to point 2 and has terminals at point 1. Mode 2 extends from 1 to 3 with terminals at 2. Each mode has a sinusoidal current distribution and unit terminal current as in Equations (2.13) and (2.14). Now let us represent $\vec{J}_s(\ell)$ as the superposition of the two modal currents with weightings I_1 and I_2. This gives a piecewise-sinusoidal expansion for $\vec{J}_s(\ell)$ with two unknown constants I_1 and I_2.

In the exact solution, the tangential electric field vanishes everywhere on contour C. Thus, if one moves an electric test probe to the conducting surface, as in Figure 12, the open-circuit voltage at its terminals will read zero. To determine N current samples, one makes N independent probing tests. The probes may be real (thin-wire V-dipoles) or hypothetical (electric line sources or strip dipoles). Now suppose one adjusts the currents I_n until all the probes read zero. This procedure yields a stationary solution for the currents I_n and, under favorable conditions, tends to the rigorous solution as N increases.

Let Z_{mn} denote the mutual impedance between test-probe m in Figure 12 and mode current I_n in Figure 11. The open-circuit voltage induced in the probe is the sum of the voltage contributions from

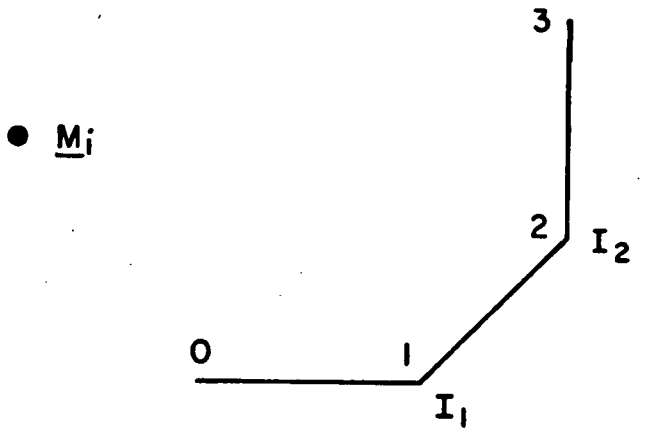

Figure 11. Perfectly conducting polygon cylinder with parallel magnetic line source $\vec{M}_i$.

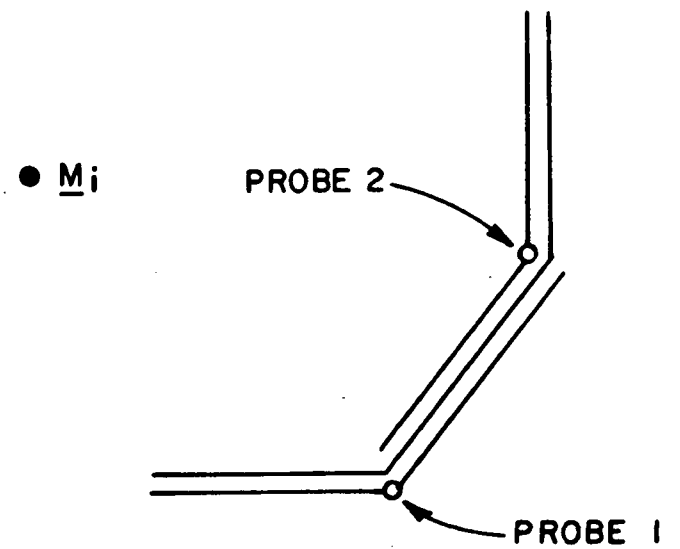

Figure 12. Electric test probes 1 and 2 are moved to the conducting surface.

$\vec{J}_S$ and $\vec{M}_i$. This voltage must vanish at each probe, leading again to Equations (2.8) to (2.10).

Linear algebra techniques are used to solve these simultaneous linear equations and determine the current distribution $\vec{J}_S(\ell)$ and the scattered fields $(\vec{E}_S, \vec{H}_S)$. The theory and method outlined above, as well as the appropriate computer programs, were generously provided by J.H. Richmond [9]. Duality may be used to obtain a solution for the case of TM polarization.

Figures 13 to 16 illustrate the various horn geometries used for the moment method solution. The horn is modelled by a two-dimensional open cylinder composed of a number of strips of infinite length and finite width. For accurate results, the strips should have widths of no more than a quarter of a wavelength. In general, the widths should be small enough to obtain a good convergent solution. For the E-plane, the source is a magnetic line source located on the end wall of the waveguide at the center of the waveguide section.

Figure 13 is a cross-sectional view in the E-plane of a conventional pyramidal horn. The geometry is described by four parameters: input waveguide width w, input waveguide length x_L, half-flare angle α, and aperture width h. The length x_L of the input waveguide should be at least one wavelength to insure that the evanescent modes from the line source have decayed sufficiently. Thus, when the electromagnetic waves reach the throat of the horn, only the dominant waveguide mode is present. The range of values for the half-flare angle α is $0°<\alpha<90°$. The walls of the cylinder are

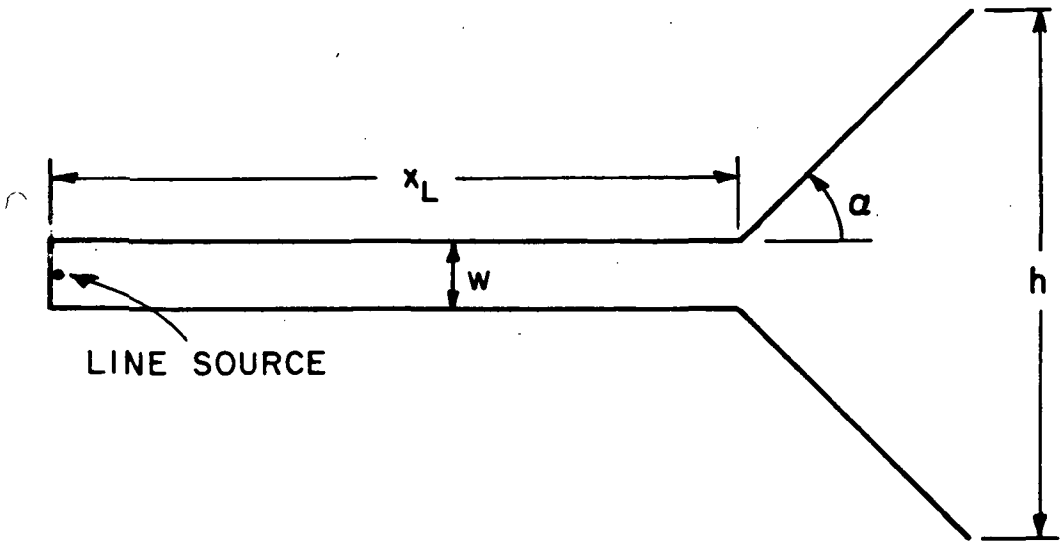

Figure 13. Two-dimensional pyramidal horn geometry for moment method solution.

divided into segments which have widths of approximately $\lambda/8$ on the waveguide section and $\lambda/5$ on the straight flare sections. The segment widths are smaller on the waveguide section because they are located closer to the line source than those on the flare sections. Thus, the fields and currents are stronger on the waveguide section and the smaller segments provide a more accurate model of the actual current distribution.

Figure 14 shows a pyramidal horn with a circularly curved throat section. Note that the junctions between this curved throat section and the waveguide and flare sections are smooth; that is, the waveguide and flare walls are attached tangentially to the circularly curved throat

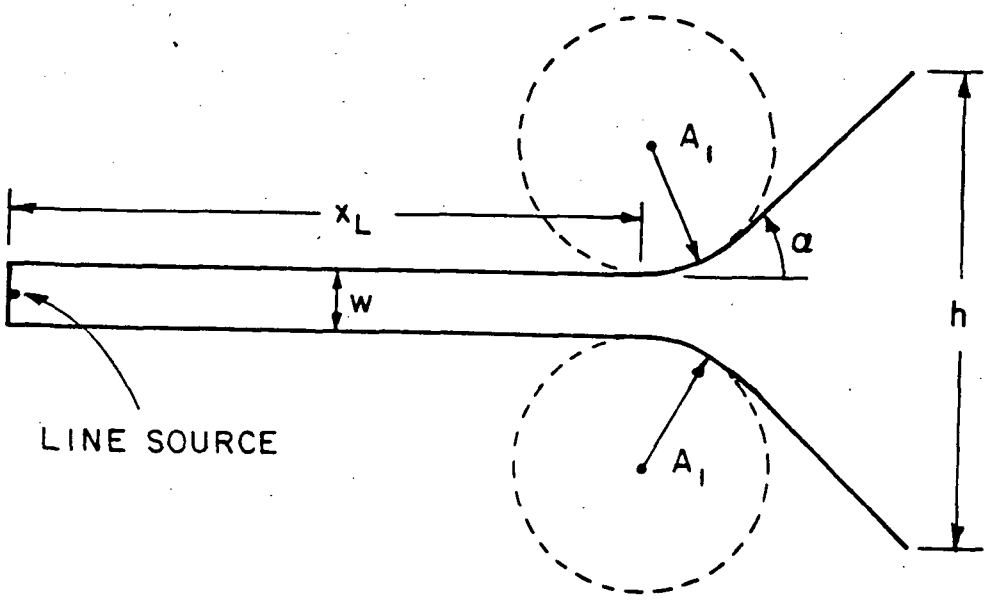

Figure 14. Two-dimensional pyramidal horn with curved throat geometry for moment method solution.

section. This geometry is described by the same parameters as the dihedral horn in addition to the radius of curvature of the throat section A_1. The segments of the throat section have widths of approximately $\lambda/8$ for the same reasons discussed earlier.

Figure 15 is a pyramidal horn with a rolled edge flare section. Note that the rolled edge also has a circular curvature and forms a 180° circular arc. The parameter A_2 denotes the radius of curvature of the rolled edge section. This section has segment widths of approximately $\lambda/5$.

Finally, Figure 16 illustrates the most general geometry treated in this report: an aperture-matched horn with circularly curved throat and rolled edge sections. All six parameters (w, x_L, α, h, A_1, and A_2) are needed to describe this geometry.

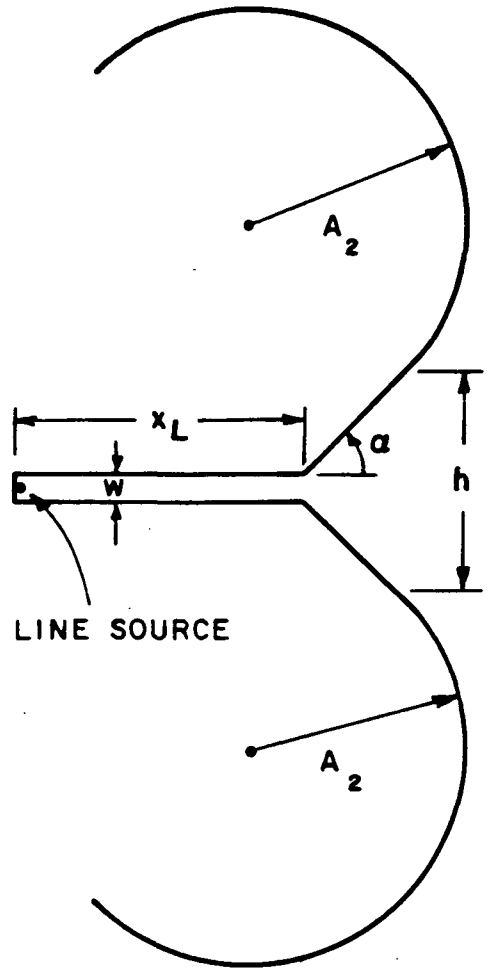

Figure 15. Two-dimensional pyramidal horn with rolled edge geometry for moment method solution.

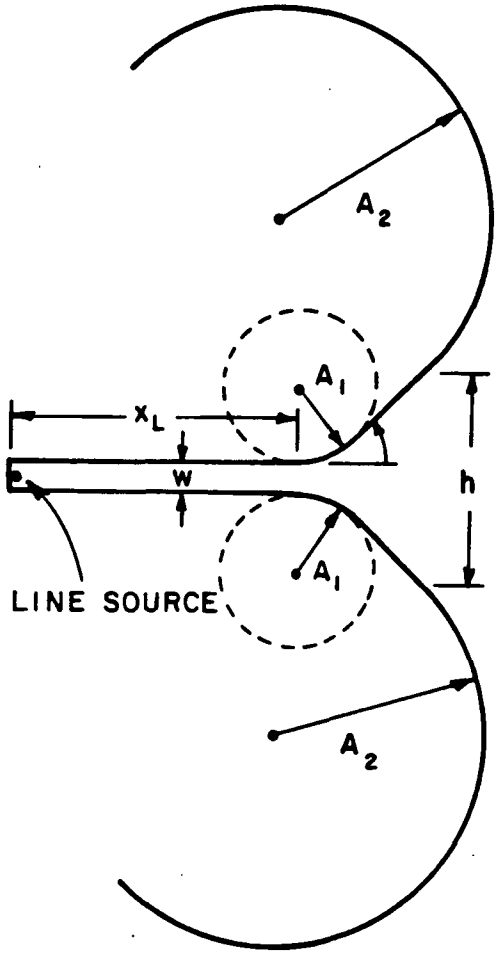

Figure 16. Two-dimensional aperture-matched horn geometry for moment method solution.

One advantage of an aperture-matched horn is a relatively low VSWR. Only a fraction of the incident wave travelling down the waveguide is reflected back to the source. This characteristic makes it desirable to calculate and predict the VSWR for such a horn geometry.

The field in the waveguide section is the sum of an incident wave travelling from the source to the aperture and a reflected field travelling from the aperture to the source. At any given point in the waveguide, the two waves add or subtract depending on their relative phase. The result is a standing wave pattern from which the VSWR and equivalently the reflection coefficient can be obtained.

The moment method solution is used to calculate the magnitude of the field at a number of points along the waveguide section. The minima and maxima of the standing wave pattern are determined from these values. The VSWR is given by

$$VSWR = \frac{|E_{MAX}|}{|E_{MIN}|} = \frac{|H_{MAX}|}{|H_{MIN}|} \tag{2.15}$$

where (E_{MAX}, H_{MAX}) and (E_{MIN}, H_{MIN}) are the maximum and minimum field magnitudes, respectively. The reflection coefficient ρ can then be calculated from elementary considerations:

$$\rho = |\rho| \, e^{j\delta} \tag{2.16}$$

$$|\rho| = \frac{VSWR-1}{VSWR+1} \tag{2.17}$$

and

$$\delta = 2kx_n - (2n-1)\pi \tag{2.18}$$

where k is the wave number and x_n is the distance from the n^{th} minima in the waveguide to the aperture.

CHAPTER III

BACKGROUND FOR UNIFORM GEOMETRICAL THEORY OF DIFFRACTION

Complete uniform geometrical theory of diffraction solutions for the standard pyramidal horn have been obtained for both the E-plane and H-plane patterns by Peters, Rudduck, and Yu [5,6]. The UTD wedge diffraction solutions were utilized in these papers. The corresponding two-dimensional geometry for the moment method solution is illustrated in Figure 13.

Burnside and Chuang [10,11] used a hybrid approach to obtain a solution for an aperture-matched horn design consisting of a dihedral horn with a rolled edge flare section as shown in Figure 15. This hybrid approach combined moment method and UTD techniques to obtain a numerically derived solution for the diffraction coefficient of a source mounted on a perfectly conducting planar surface smoothly terminated by a circular cylinder as shown in Figure 17.

Two such surfaces may be attached as shown in Figure 18 to model a horn geometry. A magnetic line source at the vertex generates the field from the throat of the horn. Note that the throat region appears

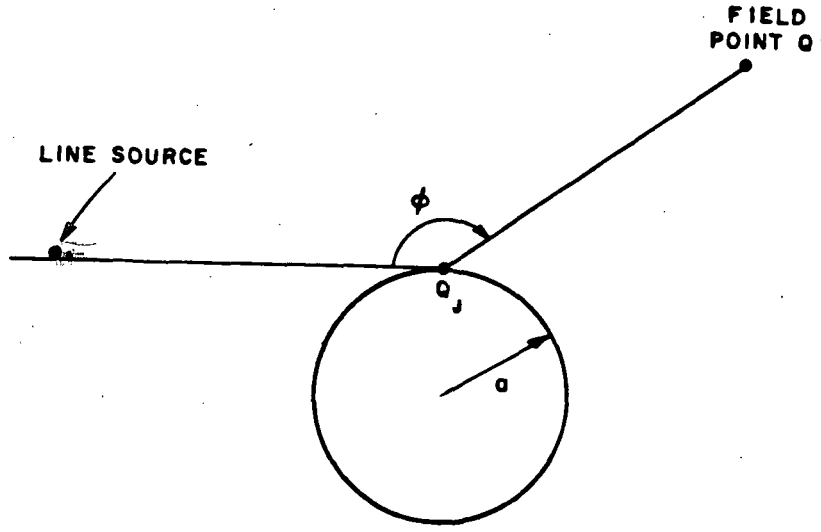

Figure 17. Two-dimensional geometry for a source mounted on a perfectly conducting planar surface smoothly terminated by a circular cylinder.

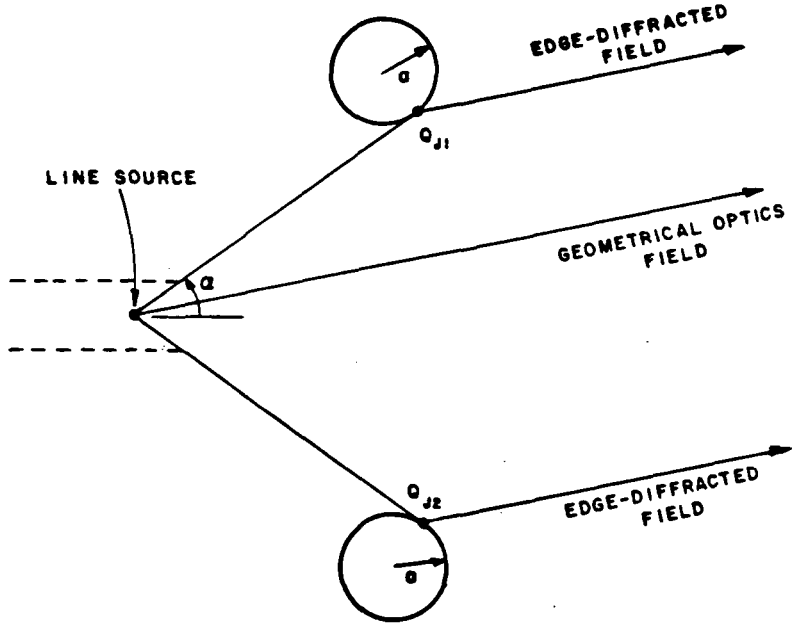

Figure 18. Two-dimensional geometry for pyramidal horn with rolled edge for UTD solution.

as an electrically small radiator; as expected, its pattern is smooth across the horn flare angle and zero otherwise. Thus, the pattern is dominated by three terms: direct throat radiation and two diffraction terms from the edge junctions. The resulting solution agrees quite well with measurements and complete moment method solutions.

The aperture-matched horn design shown in Figure 16 has, in addition to the rolled edge flare section, a circularly curved throat section. Thus, a more accurate model is needed to include the effects of the curved section on the source field from the throat. Secondly, to decrease computation time a "pure" UTD solution is preferable to the hybrid approach. In other words, one needs a UTD solution of the diffraction coefficient for a source mounted on a perfectly conducting planar surface smoothly terminated by a circular cylinder.

Such a diffraction coefficient is obtained by empirically modifying a previous solution of a diffraction coefficient for a perfectly conducting two-dimensional surface with a discontinuity in surface curvature [12] as shown in Figure 19. The diffraction coefficient and the necessary parameters are given by

$$D_h = \frac{e^{-j\pi/4}\left[C_h(\xi_1)F(X_1) - C_h(\xi_2)F(X_2)\right]}{\sqrt{2\pi k}\,(\cos\phi + \cos\phi')} \tag{3.1}$$

where

$$C_h(\xi_{1,2}) = \sqrt{\frac{2\cos\left(\frac{\phi-\phi'}{2}\right)}{a_{1,2}}}\left[\frac{1}{2}\sqrt{\frac{L}{\pi X}}\,F(X) + m_{1,2}\sqrt{\frac{2}{k}}\,q^*(\xi_{1,2})\right] e^{-j\pi/4}\, e^{-j(\xi_{1,2})^3/12} \tag{3.2}$$

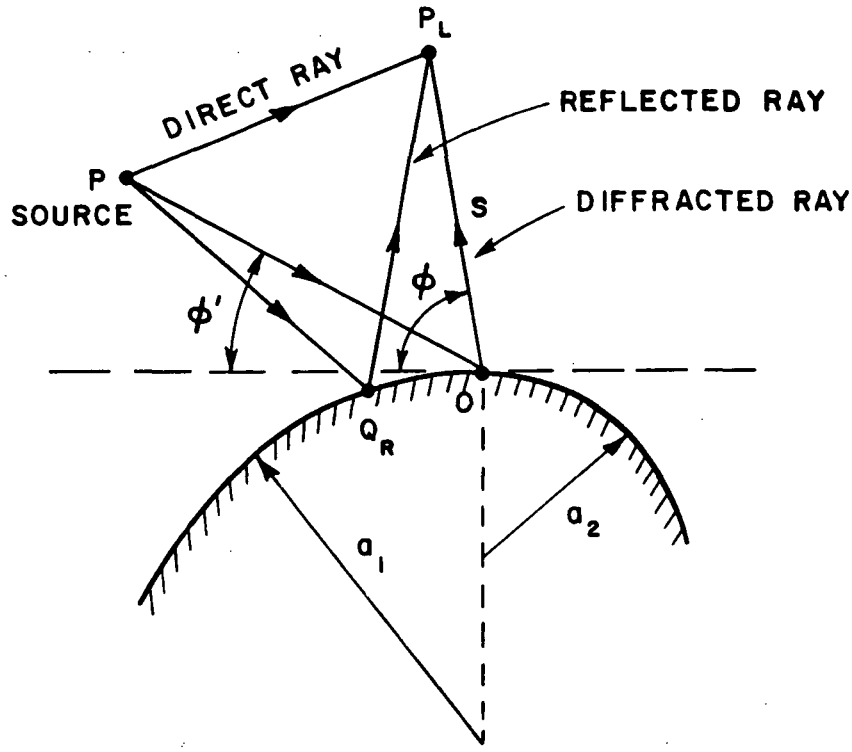

Figure 19. Geometry for a perfectly conducting two-dimensional surface with a discontinuity in surface curvature.

$$\xi_{1,2} = -2m_{1,2} \cos\left(\frac{\phi-\phi'}{2}\right) \tag{3.3}$$

$$m_{1,2} = (1/2ka_{1,2})^{1/3} \tag{3.4}$$

$$L = \frac{ss'}{s+s'} \tag{3.5}$$

$$X = 2kL \cos^2\left(\frac{\phi-\phi'}{2}\right) \tag{3.6}$$

$$X_{1,2} = \frac{ka_{1,2}(\cos\phi + \cos\phi')^2}{4\cos\left(\frac{\phi-\phi'}{2}\right)\left[1+\left(\frac{1}{s}+\frac{1}{s'}\right)\frac{a_{1,2}}{2}\cos\left(\frac{\phi-\phi'}{2}\right)\right]} \tag{3.7}$$

$$F(x) = 2j\sqrt{x}\, e^{jx} \int_{\sqrt{x}}^{\infty} e^{-jt^2} dt \tag{3.8}$$

and

$$q^*(\xi_{1,2}) = \frac{1}{\sqrt{\pi}} \int_{-\infty}^{\infty} \frac{V'(\tau)}{W_2'(\tau)} e^{-j\xi_{1,2}\tau} d\tau \quad . \tag{3.9}$$

Note that $V(\tau)$ and $W_2(\tau)$ are Fock type Airy functions given by

$$2jV(\tau) = W_1(\tau) - W_2(\tau) \tag{3.10}$$

where

$$W_{1,2}(\tau) = \frac{1}{\sqrt{\pi}} \int_{\infty e^{\mp 2\pi/3}}^{\infty - j\varepsilon} e^{\tau t - t^3/3}\, dt \tag{3.11}$$

with ε being a positive number however small; further,

$$V'(\tau) = \frac{\partial V_2(\tau)}{\partial \tau} \tag{3.12}$$

and

$$W_2'(\tau) = \frac{\partial W_2(\tau)}{\partial \tau} \quad . \tag{3.13}$$

This diffraction coefficient is derived for the case where the source is off the conducting cylinder ($\phi' \neq 0$).

Let us assume that a_1 becomes infinite and $\phi'=0$ so that grazing incidence occurs as shown in Figures 20 and 21. Notice that there now exists a lit region ($0<\phi<\pi$) and a dark region ($\pi<\phi<2\pi$) where the incident field is blocked by the conducting cylinder. The necessary modifications are described in Appendix A. The resulting diffracted field for TE polarization is given in the lit region ($0<\phi<\pi$) by

$$\vec{H}(Q) = \hat{z} H^i(Q_J) D_h \frac{e^{-jks}}{\sqrt{s}} \tag{3.14}$$

where $H^i(Q_J)$ is the field incident on the junction at the point Q_J, s is the distance from Q_J to the field point, and

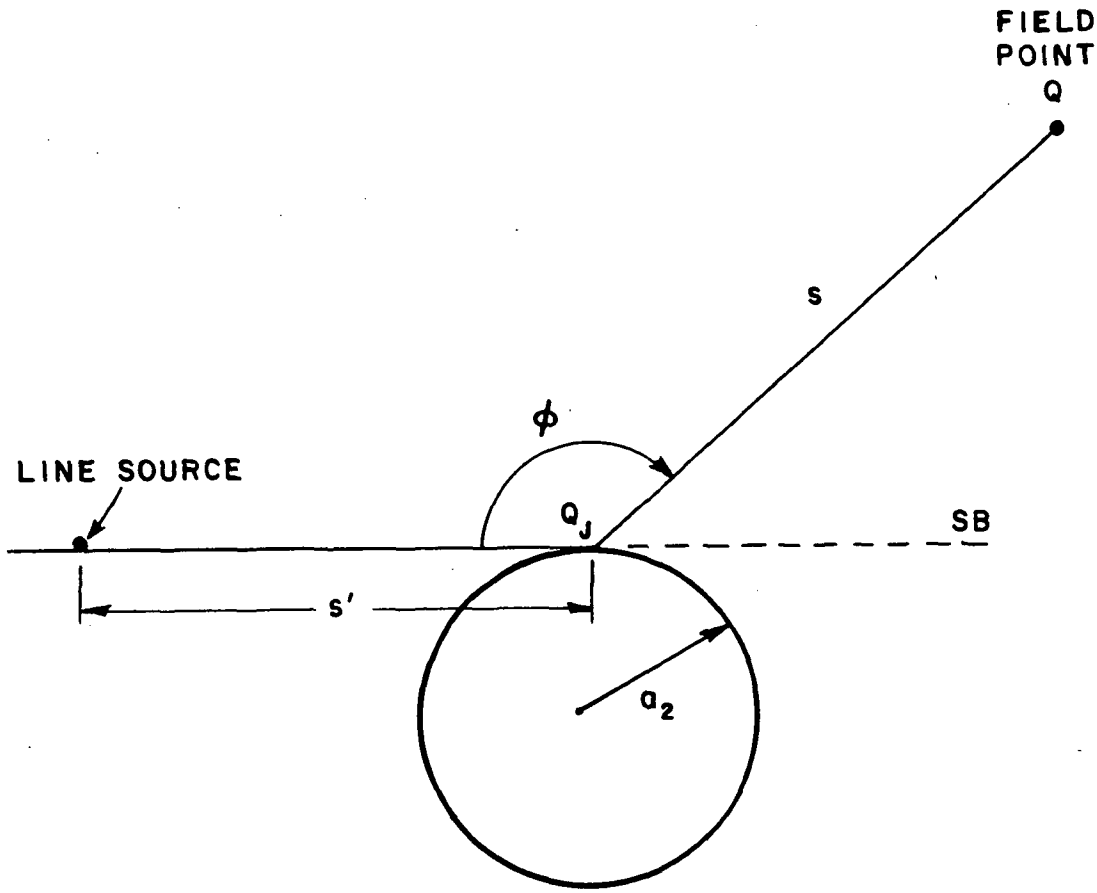

Figure 20. Two-dimensional geometry for the lit region ($0<\phi<\pi$) field for a line source mounted on a perfectly conducting planar surface smoothly terminated by a circular cylinder.

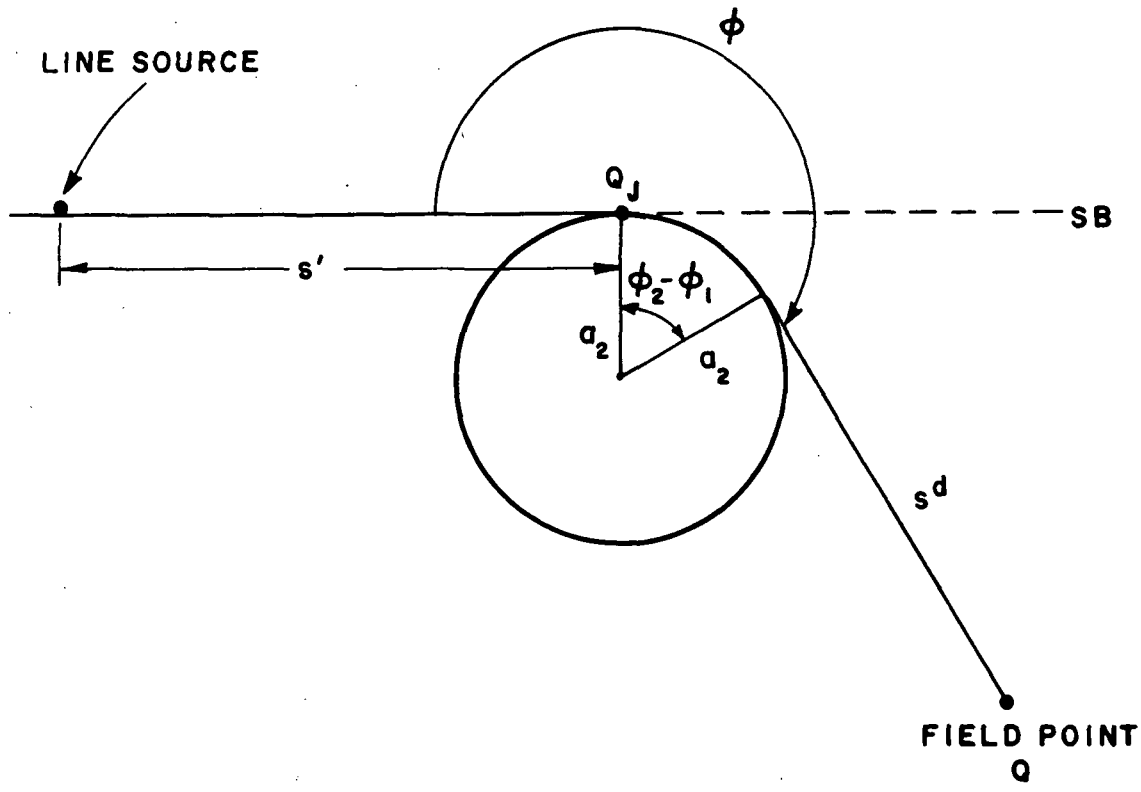

Figure 21. Two-dimensional geometry for the shadow region ($\pi<\phi<2\pi$) field for a line source mounted on a perfectly conducting planar surface smoothly terminated by a circular cylinder.

$$D_h = \frac{-e^{-j\pi/4}}{\sqrt{2\pi k}} \quad \frac{\cos\left(\frac{\phi-\phi'}{2}\right) F(X_1) + C_h(\xi_2)\, F(X_2)}{\cos\phi + \cos\phi'} \tag{3.15}$$

$$C_h(\xi_2) = \sqrt{\frac{2\cos\left(\frac{\phi-\phi'}{2}\right)}{a_2}} \left[\frac{1}{2} \sqrt{\frac{L}{\pi X}}\, F(X) + m_2 \sqrt{\frac{2}{k}}\, q^*(\xi_2) \right] e^{-j\pi/4}\, e^{-j(\xi_2)^3/12} \,. \tag{3.16}$$

$$\xi_2 = -\, 2m_2 \cos\left(\frac{\phi-\phi'}{2}\right) \tag{3.17}$$

$$m_2 = (1/2\ ka_2)^{1/3} \tag{3.18}$$

$$L = \frac{ss'}{s + s'} \tag{3.19}$$

$$X = 2kL \cos^2\left(\frac{\phi-\phi'}{2}\right) \tag{3.20}$$

$$X_1 = \frac{kL(\cos\phi + \cos\phi')^2}{8\cos^2\left(\frac{\phi-\phi'}{2}\right)} \tag{3.21}$$

and,

$$X_2 = \frac{ka_2\,(\cos\phi + \cos\phi')^2}{4\cos\left(\frac{\phi-\phi'}{2}\right)\left[1 + \left(\frac{1}{s} + \frac{1}{s'}\right) a_2/2 \cos\left(\frac{\phi-\phi'}{2}\right)\right]} \,. \tag{3.22}$$

In the shadow region ($\pi<\phi<2\pi$), the diffracted field is given by

$$\vec{H}(Q) = \hat{z}H^i(Q_J)C\tau_h \frac{e^{-jks^d}}{\sqrt{s^d}} \tag{3.23}$$

where

$$\tau_h = m_2\, e^{-jkt}\, \sqrt{2/k} \left[\frac{F(X^d)}{2\xi\sqrt{\pi}} - q^*(\xi) \right] e^{-j\pi/4} \tag{3.24}$$

$$m_2 = (1/2ka_2)^{1/3} \tag{3.25}$$

$$t = a_2\, |\phi_2 - \phi_1| \tag{3.26}$$

$$\xi = \frac{m_2 t}{a_2} = m_2\, |\phi_2 - \phi_1| \tag{3.27}$$

$$X^d = \frac{k\, s' s^d}{s' + s^d} \frac{\xi^2}{2m_2^2} \tag{3.28}$$

$$C = \frac{H_L(Q)}{H_S(Q)}\bigg|_{SB} = \left[\frac{H^i(Q) + H^i(Q_J)\, D_h \frac{e^{-jks}}{\sqrt{s}}}{H^i(Q_J)\tau_h \frac{e^{-jks^d}}{\sqrt{s^d}}} \right]\bigg|_{SB} \tag{3.29}$$

and s^d is the distance from the creeping wave launch point Q_T to the field point. The functions $F(x)$ and $q^*(x)$ are defined in Equations (3.8) to (3.13). This coefficient is found to give good results for $s' > 1.5\lambda$ and $a_2 > 0.5\lambda$ (see Appendix A for details).

The aperture-matched horn is modelled by the two-dimensional geometry shown in Figure 22 with the x-axis being the axis of symmetry of the horn. A plane wave with the $\vec{E}$ field polarized in the y-direction is incident in the waveguide. The field strikes the junctions at Q_{J11} and Q_{J12} resulting in the diffracted fields $\vec{H}_{J1}$ and $\vec{H}_{J2}$.

Consider a circular aperture of radius (R_A) centered at the apex (P) of the horn. The radius (R_A) is such that the aperture is at the junctions (Q_{JS1} and Q_{JS2}) between the curved throat sections and the walls of the horn. The creeping wave fields which travel around the curved section and strike the junctions (Q_{JS1} and Q_{JS2}) will also produce diffracted fields. However, it is assumed that the creeping waves have attenuated substantially by the time they reach the second junction. Thus, to a first-order approximation, this term may be neglected. Considering only first-order terms, the field distribution across the aperture has three contributions: the incident waveguide field $\vec{H}^i(Q)$ and the two diffracted fields $\vec{H}^d_{J1}(Q)$ and $\vec{H}^d_{J2}(Q)$ from junctions Q_{J11} and Q_{J12}, respectively.

The horn aperture with the various regions are illustrated in Figure 23. The aperture fields are given by

$$\vec{H}(Q) = \vec{H}^i(Q) + \vec{H}^d_{J1}(Q) + \vec{H}^d_{J2}(Q) \qquad (3.30)$$

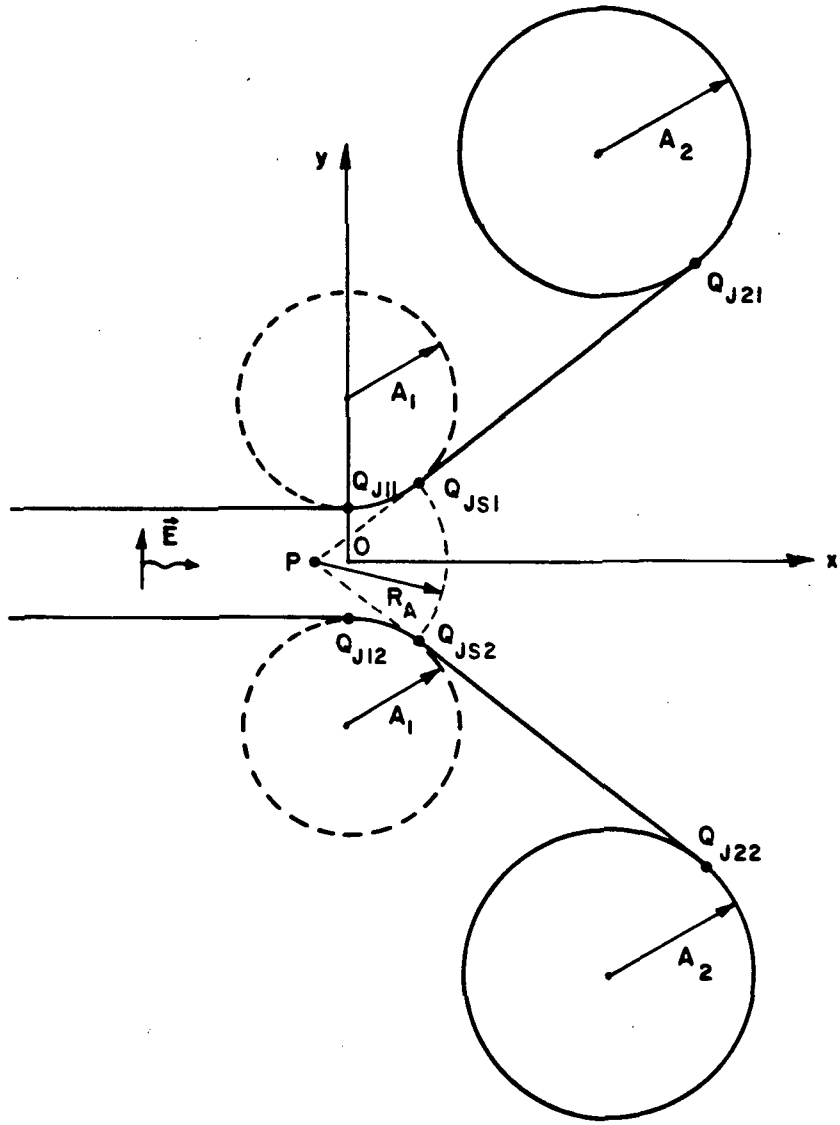

Figure 22. Two-dimensional aperture-matched horn geometry for UTD solution.

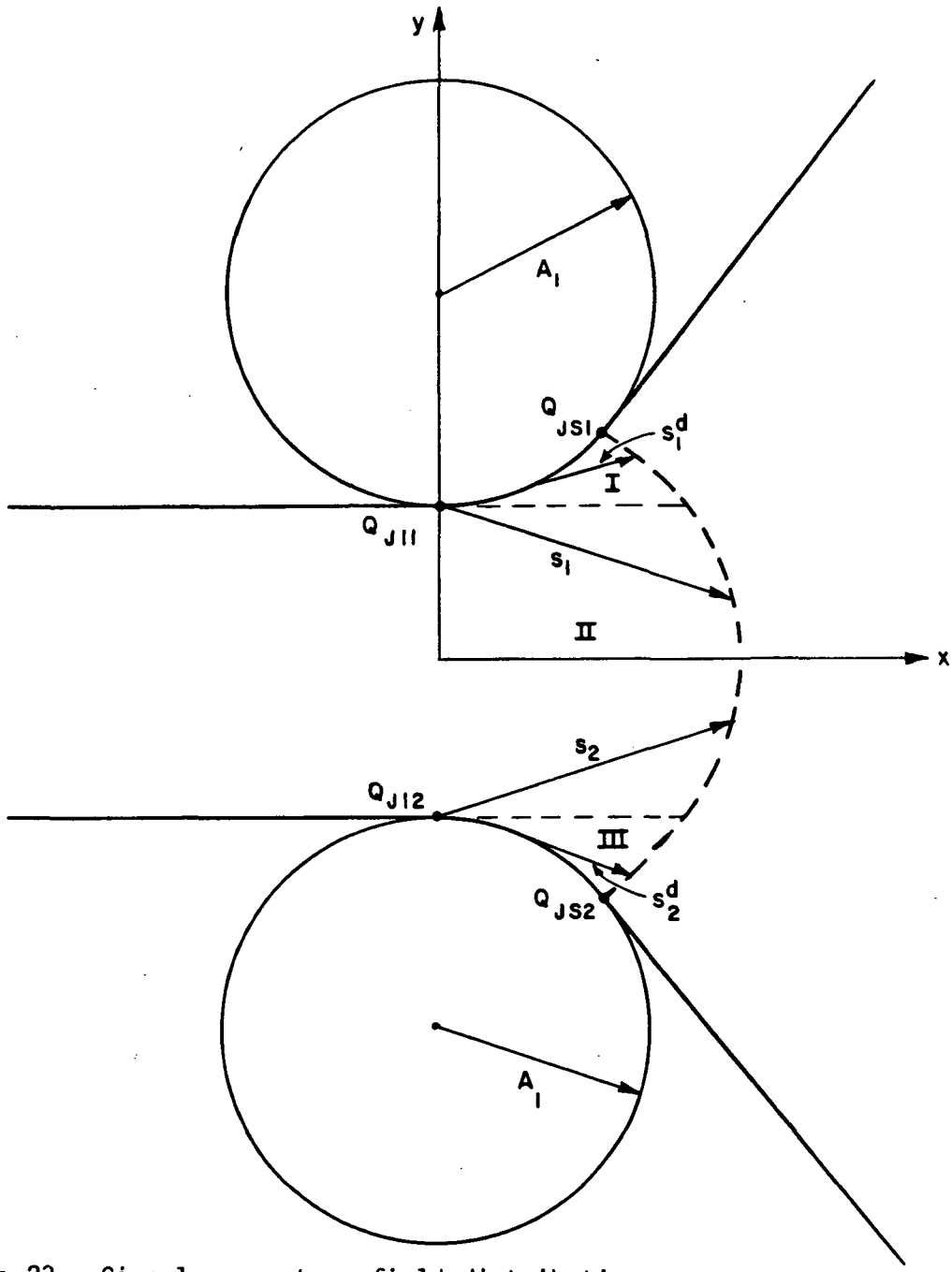

Figure 23. Circular aperture field distribution.

in region II, and

$$\vec{H}(Q) = \vec{H}^{d}_{J1}(Q) + \vec{H}^{d}_{J2}(Q) \tag{3.31}$$

in regions I and III. The component fields at the point $Q = (X_A, Y_A)$ in the aperture are

$$\vec{H}^{i}(Q) = \hat{z}\, e^{-jkX_A} \tag{3.32}$$

$$\vec{H}^{d}_{J1}(Q) = \begin{cases} \hat{z}\, H^{i}(Q_{J11})\, D_{h1}\, \dfrac{e^{-jks_1}}{\sqrt{s_1}} & \text{in regions II and III} \\ \hat{z}\, H^{i}(Q_{J11})\, C_1\, \tau_{h1}\, \dfrac{e^{-jks^{d}_1}}{\sqrt{s^{d}_1}} & \text{in region I} \end{cases} \tag{3.33}$$

and

$$\vec{H}^{d}_{J2}(Q) = \begin{cases} \hat{z}\, H^{i}(Q_{J12})\, D_{h2}\, \dfrac{e^{-jks_2}}{\sqrt{s_2}} & \text{in regions I and II} \\ \hat{z}\, H^{i}(Q_{J12})\, C_2\, \tau_{h2}\, \dfrac{e^{-jks^{d}_2}}{\sqrt{s^{d}_2}} & \text{in region III} \end{cases} \tag{3.34}$$

where $s_{1,2}$, $s^{d}_{1,2}$, $D_{h1,2}$, $C_{1,2}$, and $\tau_{h1,2}$ are as defined in Equations (3.14) to (3.29) applied to junction $Q_{J11,2}$. For plane wave incidence in the near field, the constant $C_{1,2}$ is given by

$$C_{1,2} = \frac{m\sqrt{2}\, q^*(0)\, e^{-j\pi/4} + \sqrt{ks_{1,2}}\, (1-2H^i(Q_{J11,2}))}{2m\sqrt{2}\, q^*(0)\, e^{-j\pi/4} - \sqrt{ks_{1,2}}} \tag{3.35}$$

where

$$m = (1/2kA_1)^{1/3} \tag{3.36}$$

and $q^*(0)$ is the appropriate Fock integral evaluated at zero.

Once the aperture field distribution is known, one may replace the original geometry with the wedge geometry shown in Figure 24. Neglecting, for the moment, the finite termination of the perfectly conducting wedge at the rolled edges of the horn, the resulting geometry is an infinite two-dimensional wedge of angle equal to 2α.

The magnetic field (H_Z^i) must satisfy the scalar Helmholtz equation in this source-free wedge-shaped region which is given by

$$\nabla^2 H_Z^i + k^2 H_Z^i = 0 \tag{3.37}$$

where k is the free space wave number. The accompanying boundary conditions are obtained from the condition on the tangential electric field at the perfectly conducting boundaries such that

$$E_\rho^i(\rho,\phi) = \frac{1}{j\omega\varepsilon} \frac{\partial H_Z^i(\rho,\phi)}{\partial\phi} = 0 \tag{3.38}$$

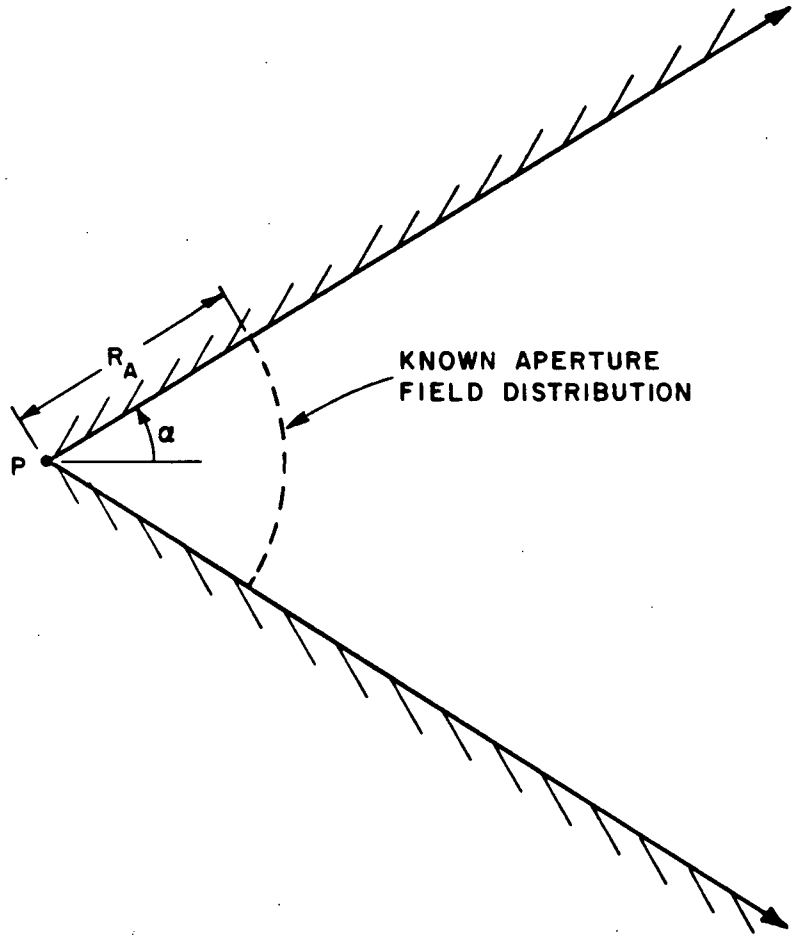

Figure 24. Two-dimensional wedge geometry for calculating the incident field from the throat.

at $\phi = \pm \alpha$. Also, $H_z^i(\rho,\phi)$ must satisfy the radiation conditions as $\rho \to \infty$ for $e^{j\omega t}$ time dependence. Thus, an appropriate solution for $H_z^i(\rho,\phi)$ is

$$H_z^i(\rho,\phi) = \sum_{n=0}^{\infty} A_n \cos\left(\frac{n\pi}{\alpha}\phi\right) H_n^{(2)}(k\rho) \tag{3.39}$$

where A_n are constants to be determined. For $k\rho$ large, as in the far field, one finds that

$$H_n^{(2)}(k\rho) \doteq \sqrt{\frac{2j}{\pi k\rho}}\; j^n\, e^{-jk\rho} \; . \tag{3.40}$$

For n=0, this approximation is good to within about 10% error for $\rho > 0.2\lambda$. Then, Equation (3.37) becomes

$$H_z^i(\rho,\phi) = \frac{e^{-jk\rho}}{\sqrt{\rho}} \sum_{n=0}^{\infty} \tilde{A}_n \cos\left(\frac{n\pi}{\alpha}\phi\right) \tag{3.41}$$

where

$$\tilde{A}_n = j^n A_n \sqrt{\frac{2j}{\pi k}} \; . \tag{3.42}$$

On the circular arc aperture, $\rho = R_A$ so that

$$H_z^i(R_A,\phi) = \frac{e^{-jkR_A}}{\sqrt{R_A}} \sum_{n=0}^{\infty} \tilde{A}_n \cos\left(\frac{n\pi}{\alpha}\phi\right) = H_{zA}(\phi) \tag{3.43}$$

where $H_{zA}(\phi)$ is the known aperture distribution. Equation (3.43) is simply a Fourier cosine series representation of $H_{zA}(\phi)$. The coefficients $\tilde{A}_n$ are found by multiplying both sides of Equation (3.43) by $\cos\left(\frac{n\pi}{\alpha}\phi\right)$ and integrating over the interval $-\alpha \leq \phi \leq \alpha$. The result is

$$\tilde{A}_n = \frac{\varepsilon_n\sqrt{R_A}}{2\alpha}\, e^{-jkR_A} \int_{-\alpha}^{\alpha} H_{zA}(\phi) \cos\left(\frac{n\pi}{\alpha}\phi\right) d\phi \tag{3.44}$$

where

$$\varepsilon_n = \begin{cases} 1, & n = 0 \\ 2, & n \neq 0 \end{cases} \tag{3.45}$$

which is Neumann's number.

Once the coefficients $(\tilde{A}_n)$ have been calculated, Equation (3.41) gives the field (H_z^i) for large ρ. Provided $H_{zA}(\phi)$ is a relatively smooth function across the circular aperture, the series will converge rapidly and only the first few terms or modes will be significant. The infinite series of Equation (3.41) becomes a finite series for the incident throat field of the horn such that

$$H_z^i(\rho,\phi) = \frac{e^{-jk\rho}}{\sqrt{\rho}} \sum_{n=0}^{N} \tilde{A}_n \cos\left(\frac{n\pi}{\alpha}\phi\right) \tag{3.46}$$

where N is a finite number such that $\tilde{A}_n$ for $n > N$ are relatively small. Note that each mode in the series has the same ρ dependence as a line

source field coming from the apex, and each can be treated as such in the subsequent UTD analysis.

The geometry of the problem now reduces to that of Figure 25. Note that it is identical to the model used by Burnside and Chuang [11] except that the incident field from the throat of the horn is modified to account for the curved throat sections. In a first-order solution there are three contributions: the incident throat field and the two diffracted fields from the junctions Q_{J21} and Q_{J22}. The incident throat field is given by

$$\vec{H}^i(Q) = \begin{cases} \hat{z}\,\dfrac{e^{-jk\rho}}{\sqrt{\rho}} \displaystyle\sum_{n=0}^{N} \tilde{A}_n \cos\left(\frac{n\pi}{\alpha}\phi\right) & \text{in region I} \\ 0 & \text{in regions II, III, IV, and V} \end{cases} \tag{3.47}$$

where the $\tilde{A}_n$ are defined in Equation (3.44). The diffracted fields $\vec{H}^{d1}$ and $\vec{H}^{d2}$ from the junctions at Q_{J21} and Q_{J22} are, respectively, given by

$$\vec{H}^{d1}(Q) = \begin{cases} \hat{z}\, H^i(Q_{J21}) D_{h1} \dfrac{e^{-jk\rho_1}}{\sqrt{\rho_1}} & \text{in regions I and V} \\ \hat{z}\, H^i(Q_{J21}) C_1 \tau_{h1} \dfrac{e^{-jk\rho_1^d}}{\sqrt{\rho_1^d}} & \text{in regions II and III} \\ 0 & \text{in region IV} \end{cases} \tag{3.48}$$

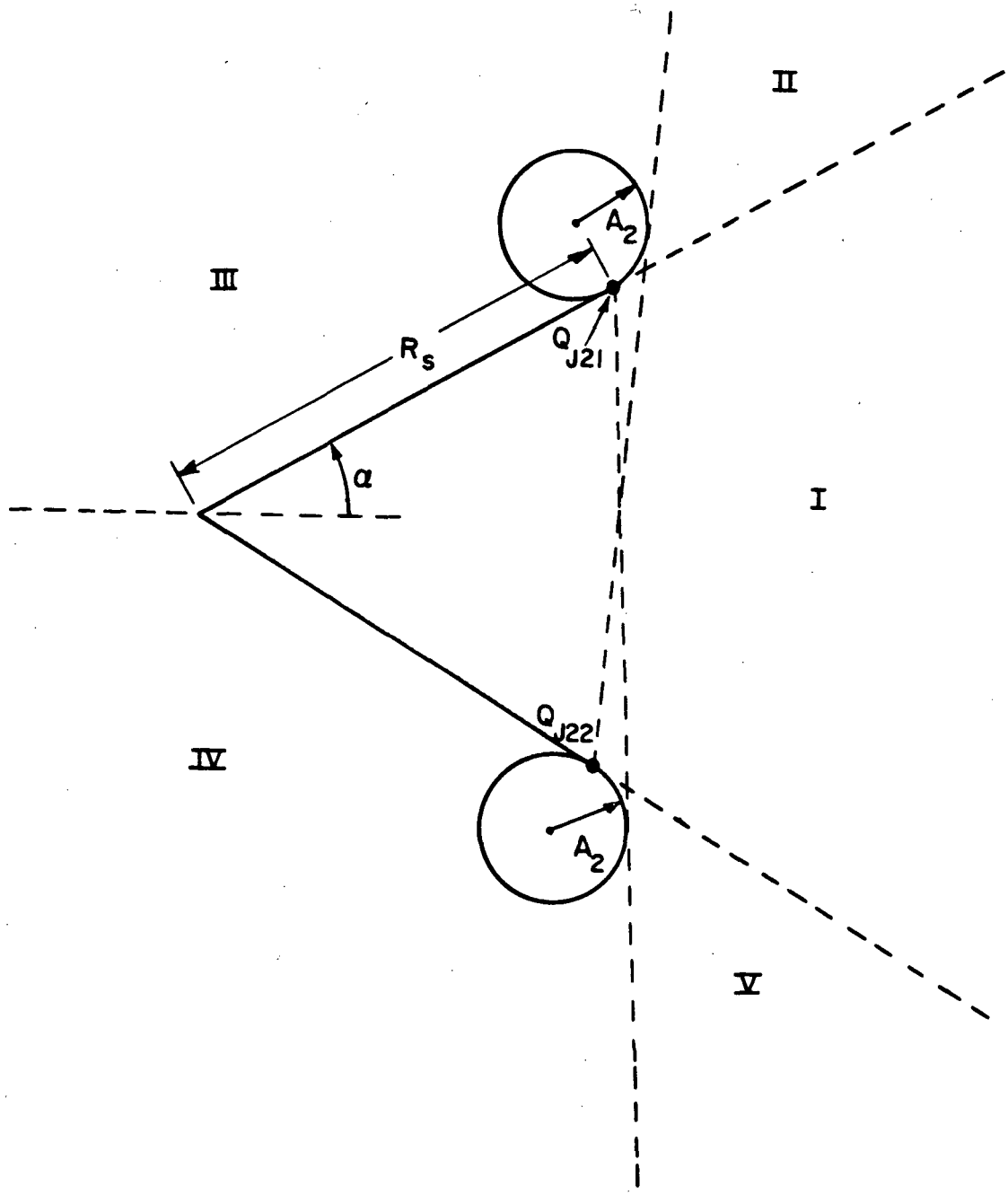

Figure 25. Two-dimensional aperture-matched horn geometry for UTD solution with a modal expansion of the throat field.

and

$$\vec{H}^{d2}(Q) = \begin{cases} \hat{z}\, H^{i}(Q_{J22}) D_{h2} \dfrac{e^{-jk\rho_2}}{\sqrt{\rho_2}} & \text{in regions I and II} \\ \hat{z}\, H^{i}(Q_{J22}) C_2 \tau_{h2} \dfrac{e^{-jk\rho_2^d}}{\sqrt{\rho_2^d}} & \text{in regions IV and V} \\ 0 & \text{in region III} \end{cases} \tag{3.49}$$

where $\rho_{1,2}$, $\rho^d_{1,2}$, $D_{h1,2}$, $C_{1,2}$, and $\tau_{h1,2}$ are as defined in Equations (3.12) to (3.27) applied to the $Q_{J21,2}$ junction. For the far field for a line source incident on the junction one finds that

$$C_{1,2} = \frac{m\sqrt{2}\; q^*(0)\; e^{-j\pi/4} - \sqrt{kR_s}}{2m\sqrt{2}\; q^*(0)\; e^{-j\pi/4} - \sqrt{kR_s}} \tag{3.50}$$

where

$$m = (1/2\; k\; A_2)^{1/3} \tag{3.51}$$

and $q^*(0)$ is the appropriate Fock integral evaluated at zero.

CHAPTER IV

RESULTS AND ANALYSIS

The purpose of this chapter is twofold. Results obtained from the theory discussed in the previous two chapters are presented and analyzed to determine the validity of the theory. Secondly, the value of the particular aperture-matched horn design considered in this report as well as the effect of changing various design parameters are discussed.

Consider first the two-dimensional geometry for the standard pyramidal horn shown in Figure 26(a). The frequency is 10 Ghz, and the remaining parameters are given in the figure. The pattern obtained by the moment method solution is shown in Figure 26(b), and the calculated VSWR is 1.35.

Next, a rolled edge of radius A_2 = 7.62 cm is added to this pyramidal horn as illustrated in Figure 27(a). Note that this is the two-dimensional geometry treated by Burnside and Chuang in Reference [11]. The resulting moment method pattern is shown in Figure 27(b). As expected, the main beam of the pattern is broader than that of the pyramidal horn, and the side lobes are much lower. The sharp edges of the pyramidal horn diffract the energy into the main beam region where it interferes with the incident field from the throat. The rolled

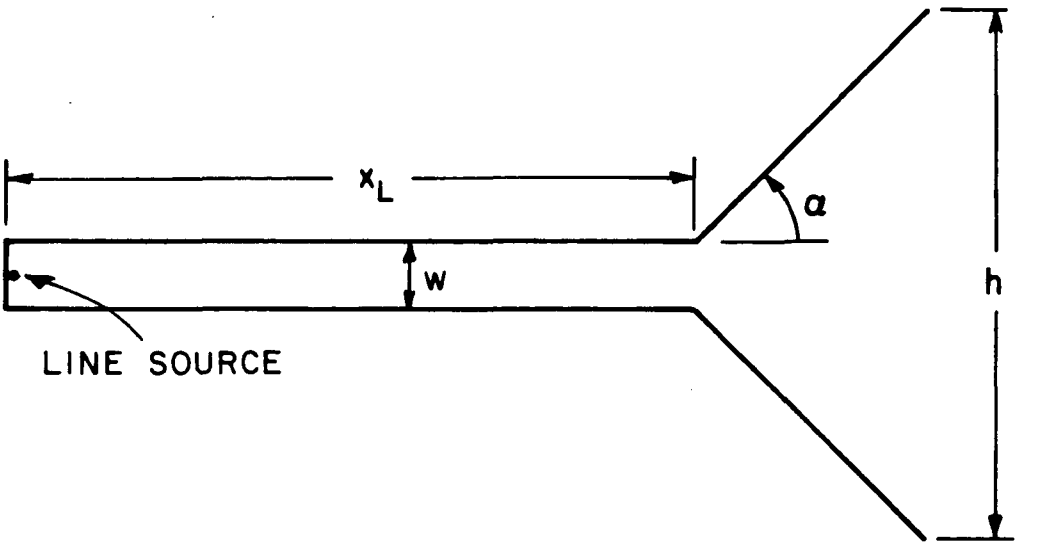

(a). Two-dimensional geometry for pyramidal horn (E-plane). f = 10 GHz, w = 1.016 cm, x_L = 10.16 cm, α = 45°, h = 7.85 cm.

Figure 26. Moment method solution for standard pyramidal horn.

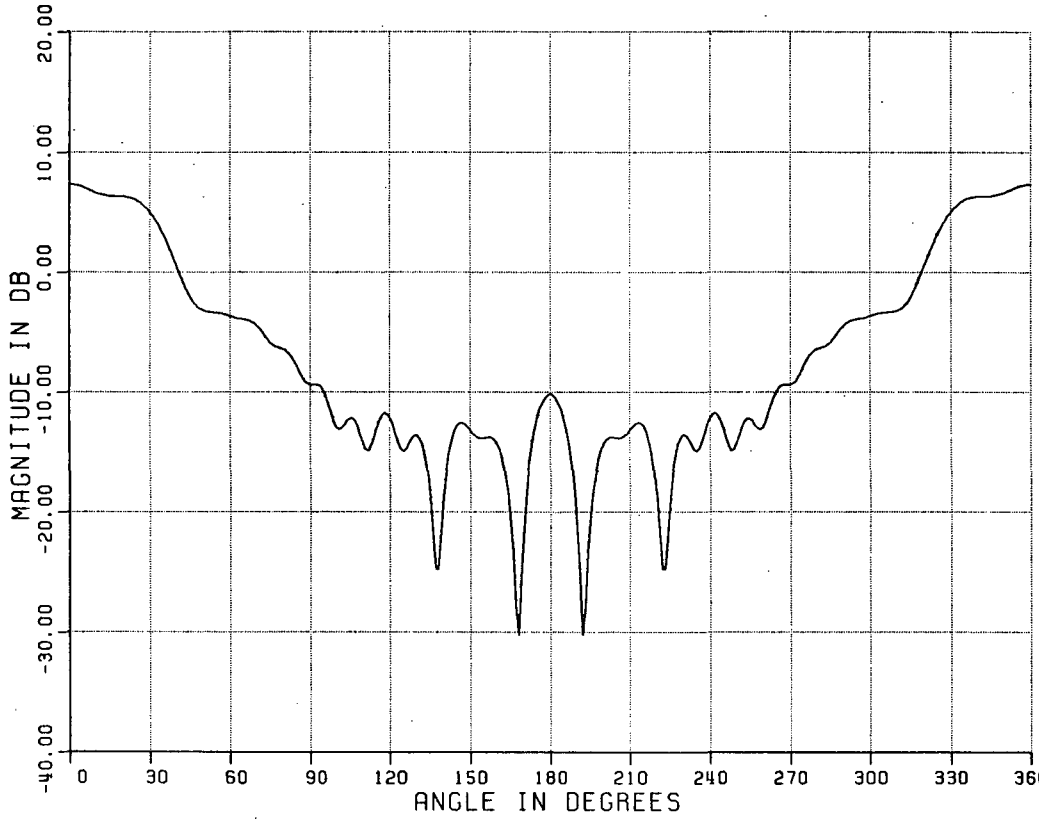

(b). E-plane field pattern for pyramidal horn obtained by moment method solution. VSWR = 1.35.

Figure 26. (Continued).

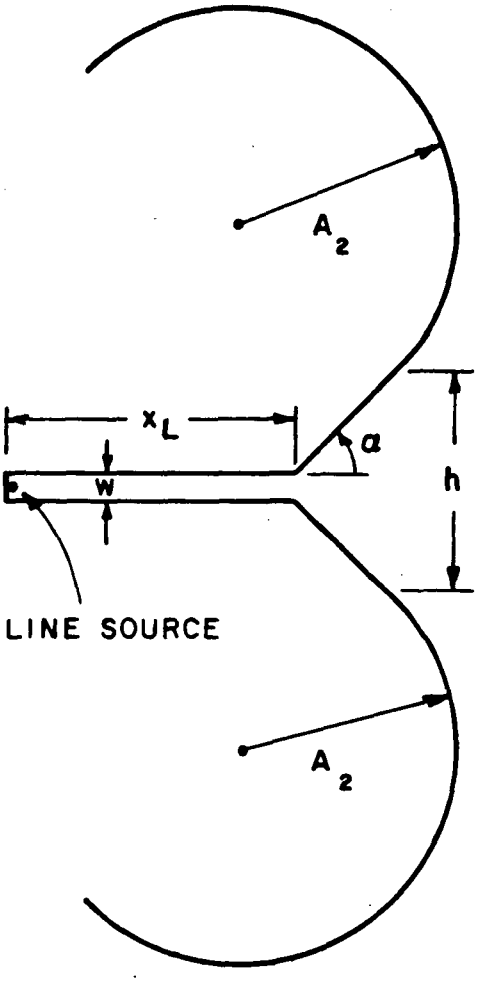

(a). Two dimensional geometry for pyramidal horn with rolled edge section (E-plane).
f = 10 GHz, w = 1.016 cm, x_L = 10.16 cm, α = 45°,
h = 7.85 cm, A_2 = 7.62 cm.

Figure 27. Moment method solution for pyramidal horn with rolled edge.

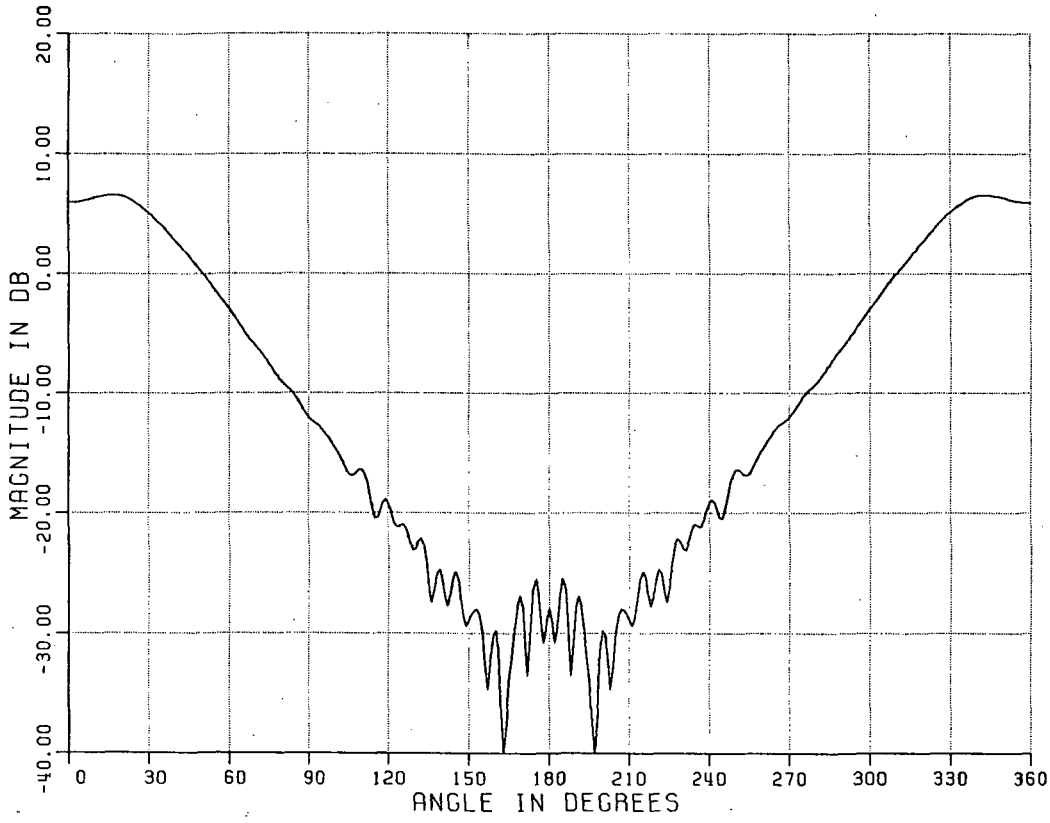

(b) E-plane field pattern for pyramidal horn with rolled edge section obtained by moment method solution. VSWR = 1.35.

Figure 27. (Continued).

edges, on the other hand, allow the energy to creep around the curved section and gradually shed off into the side lobe region. The calculated VSWR is 1.35.

Figure 28(a) illustrates the aperture-matched horn with a curved throat section with a radius of 3.05 cm. The corresponding pattern shown in Figure 28(b) is almost identical to that of Figure 27(b). However, the calculated VSWR is 1.04. This is almost an 87% reduction in the reflection coefficient at the throat of the horn. Thus, the rolled edges improve the pattern by making it broader and reducing the side lobes; in addition, the curved throat section serves mainly to reduce the VSWR.

The frequency dependence of the field pattern and VSWR of the aperture-matched horn is examined in Figure 29 using the moment method approach. At the low frequencies, the antenna is small with respect to a wavelength. As is typical for electrically small antennas, the pattern has a broad main beam with relatively high side lobes. As the frequency increases, the main beam becomes narrower, and the side lobes become lower. The VSWR decreases as the horn, particularly the radius of curvature of the throat, becomes larger with respect to the wavelength.

The results of the UTD approach are also shown in Figure 29. UTD is a high frequency technique, and the field plots clearly show this property. The solution, however, agrees quite well with the more exact moment method results at frequencies as low as 6 GHz (λ = 5 cm). At this frequency, the radius A_1 of the throat section is about 0.6λ. This is quite close to the low frequency limit of the diffraction coefficient

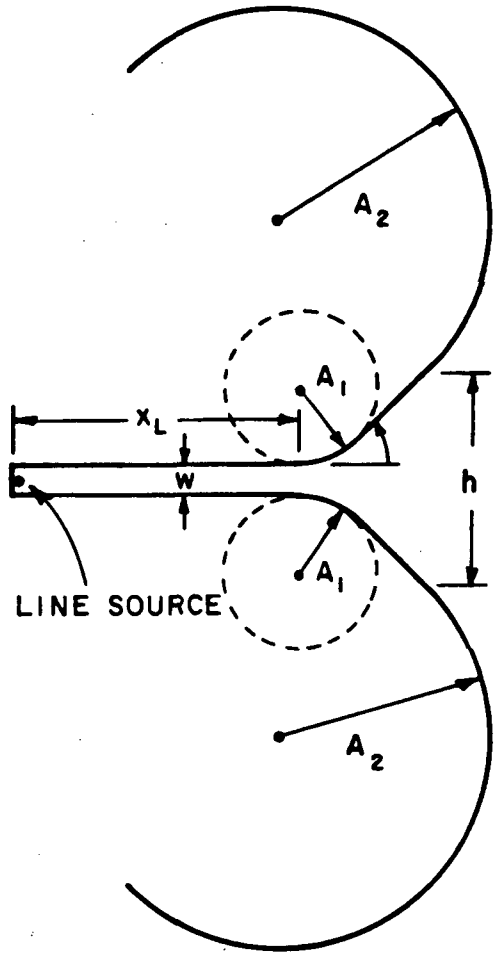

(a). Two-dimensional geometry for aperture-matched horn (E-plane).
f = 10 GHz, w = 1.016 cm, X_2 = 10.16 cm, α = 45°, h = 7.85 cm, A_1 = 3.05 cm, A_2 = 7.62 cm.

Figure 28. Moment method solution for aperture-matched horn.

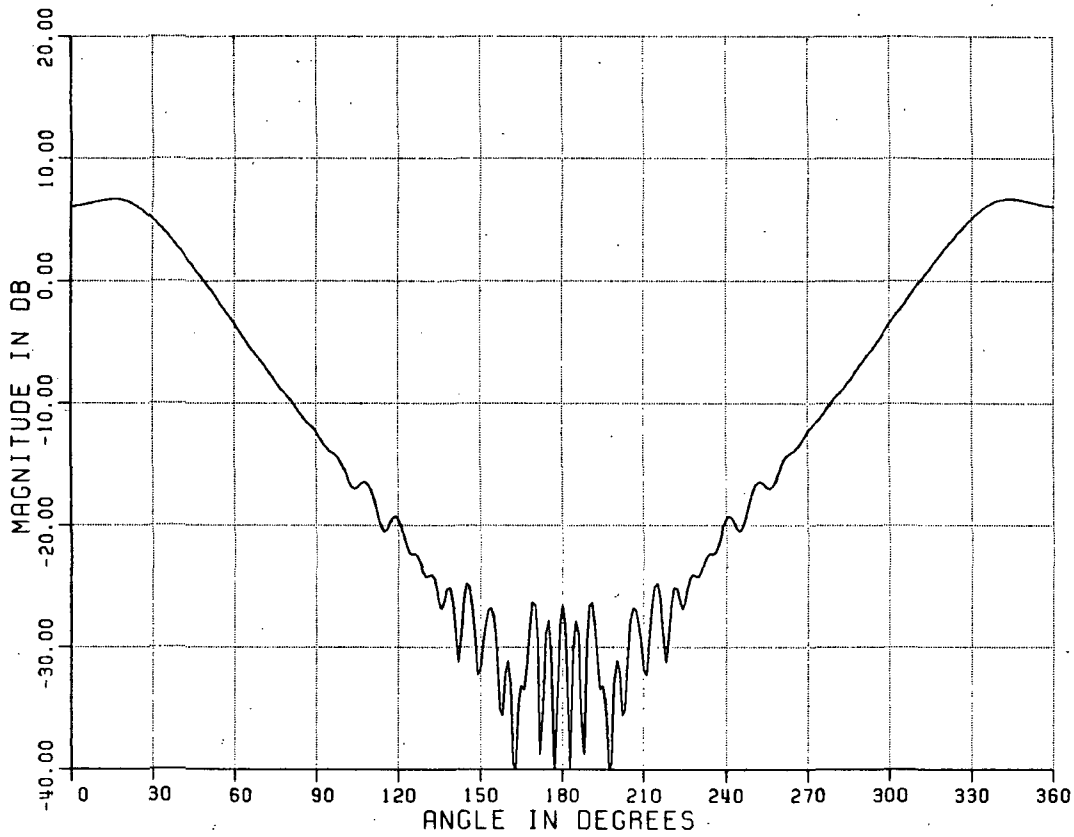

(b). E-plane field pattern for aperture-matched horn obtained by moment method solution. VSWR = 1.04.

Figure 28. (Continued).

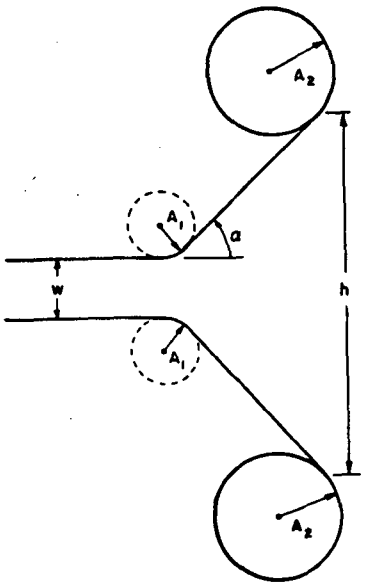

(a). Two-dimensional geometry for aperture-matched horn (E-plane). $w = 1.016$ cm, $\alpha = 45°$, $h = 7.85$ cm, $A_1 = 3.05$ cm, $A_2 = 7.62$ cm, f varies.

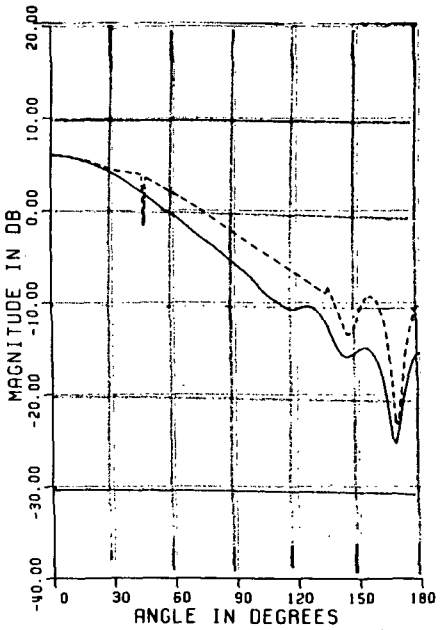

(b). E-plane field patterns for f = 2 Ghz. VSWR = 2.52.

Figure 29. Moment method and UTD solutions for aperture-matched horn as the frequency (f) is varied.

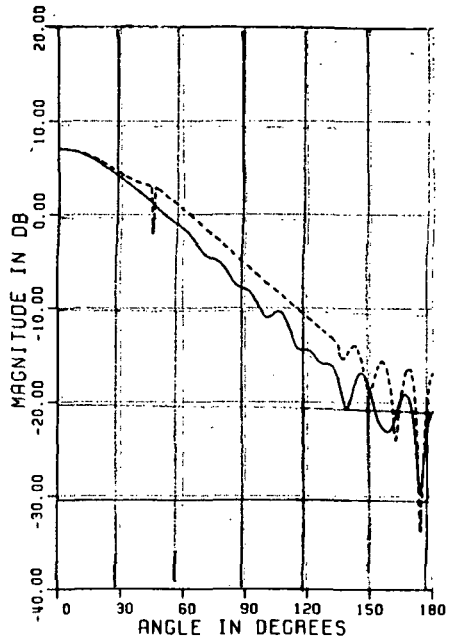

(c). E-plane field patterns for f = 4 Ghz. VSWR = 1.37

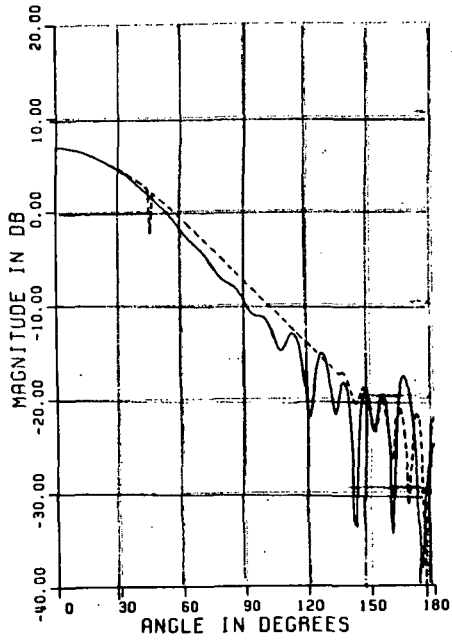

(d). E-plane field patterns for f = 6 Ghz. VSWR = 1.10.

Figure 29. (Continued).

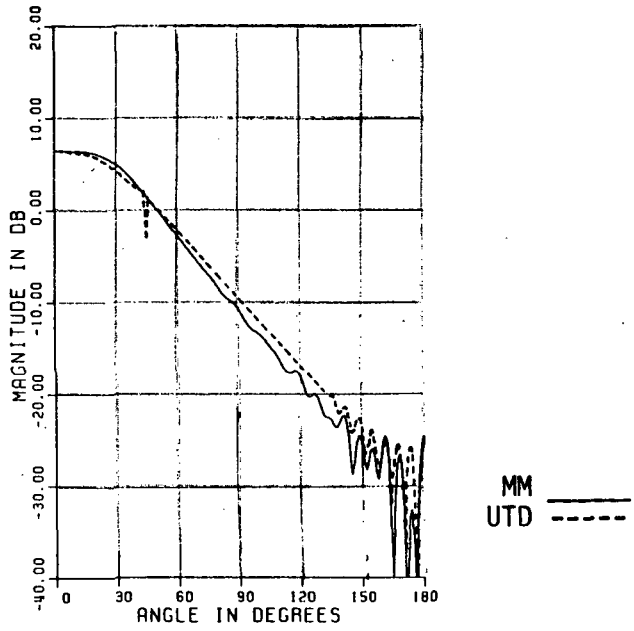

(e). E-plane field patterns for f = 8 Ghz. VSWR = 1.06.

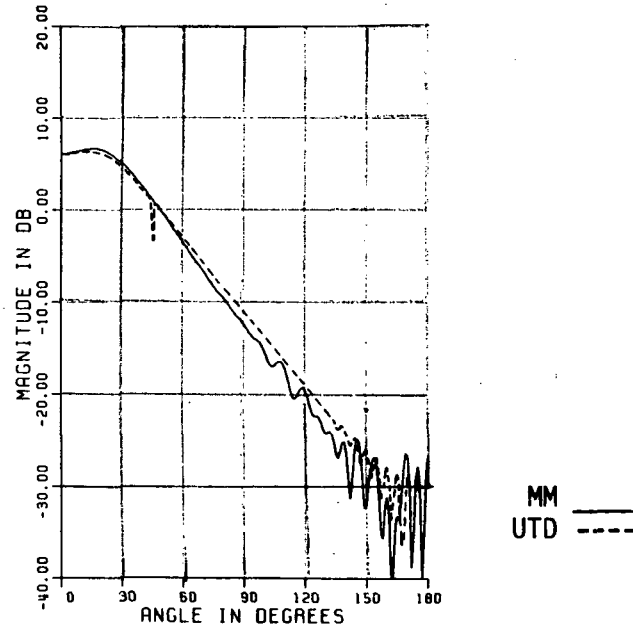

(f). E-plane field patterns for f = 10 Ghz. VSWR = 1.04.

Figure 29. (Continued).

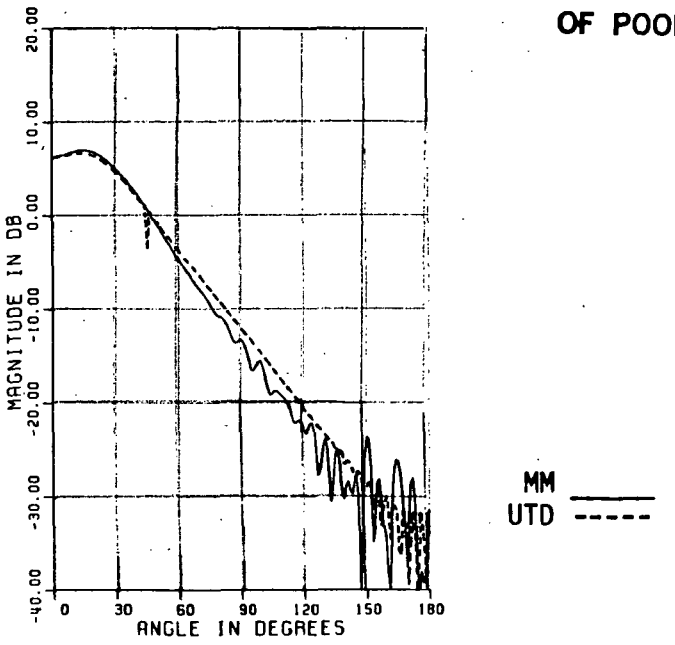

(g). E-plane field patterns for f = 12 Ghz. VSWR = 1.02.

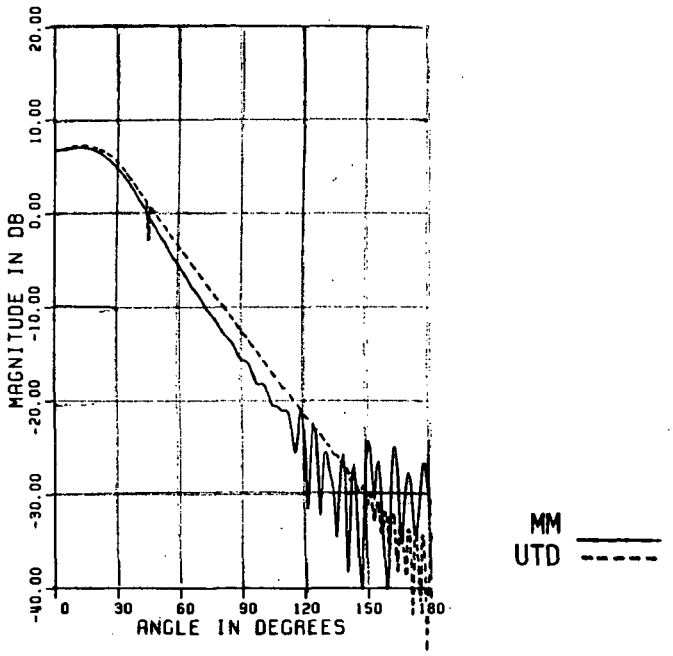

(h). E-plane field patterns for f = 14 Ghz. VSWR = 1.02.

Figure 29. (Continued).

D_{PC} which is valid for $A_1 > 0.5\lambda$. In addition, the apparent source distance s' (denoted by R_s in Figure 25) for the rolled edge is only 1.1λ. This is outside the range of validity of D_{PC}, and it probably accounts for the disagreement with the moment method solution in the region outside the flare angle. Above 6 GHz, the UTD patterns are within 1 dB of the moment method patterns in the main beam region.

There are several geometrical parameters of the aperture-matched horn which may affect the performance of a particular design. For instance, Figure 30 illustrates the pattern behavior as the radius of curvature A_1 of the throat section is varied. The results are obtained from the moment method. As A_1 decreases, the geometry approaches that of Figure 27(a). In fact, the pattern in Figure 30 (A_1 = 0.75 cm = 0.25λ) is almost identical to the pattern in Figure 27(b). As A_1 increases, the VSWR decreases. This is expected since a larger radius of curvature provides a more gradual transition from the waveguide to horn modes. Thus, there is a smaller reflection coefficient associated with the junction.

The corresponding patterns obtained from the UTD approach are also shown in Figure 30. For A_1 = 0.75 cm = 0.25λ, there is a slight disagreement with the moment method pattern which dips at 0°. This is probably due to the fact that A_1 is only a quarter of a wavelength, i.e., the low frequency case. However, another discrepancy occurs for larger values of A_1. Specifically, for A_1 = 6 cm = 2λ, the main beam begins to become too broad in the UTD solution.

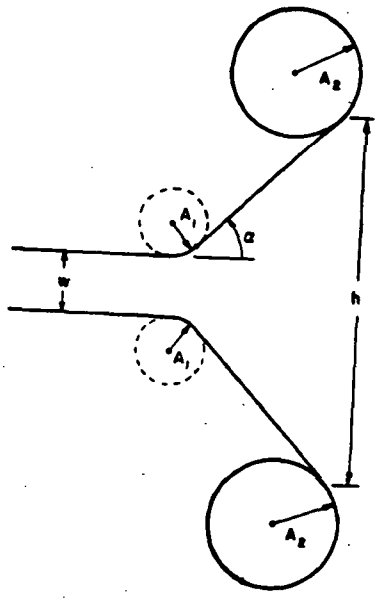

(a). Two-dimensional geometry for aperture-matched horn (E-plane). f = 10 GHz, w = 1.016 cm, α = 45°, h = 7.85 cm, A_2 = 7.62 cm, A_1 varies.

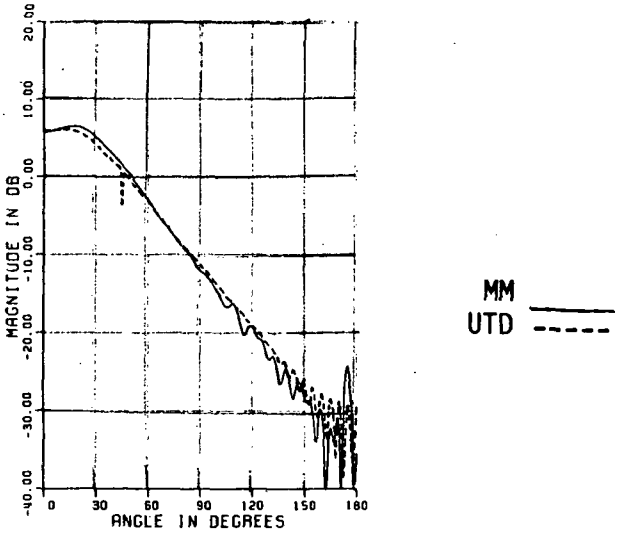

(b). E-plane field patterns for A_1 = 0.75 cm. VSWR = 1.23.

Figure 30. Moment method and UTD solutions for aperture-matched horn as the radius of curvature (A_1) of the throat section is varied.

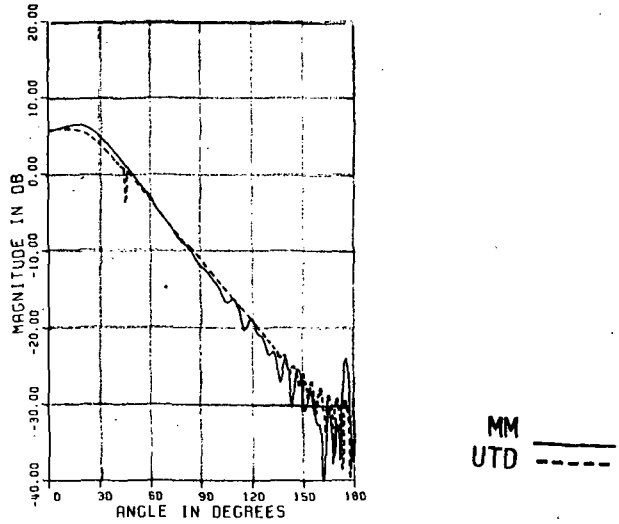

(c). E-plane field patterns for A_1 = 1.50 cm. VSWR = 1.08.

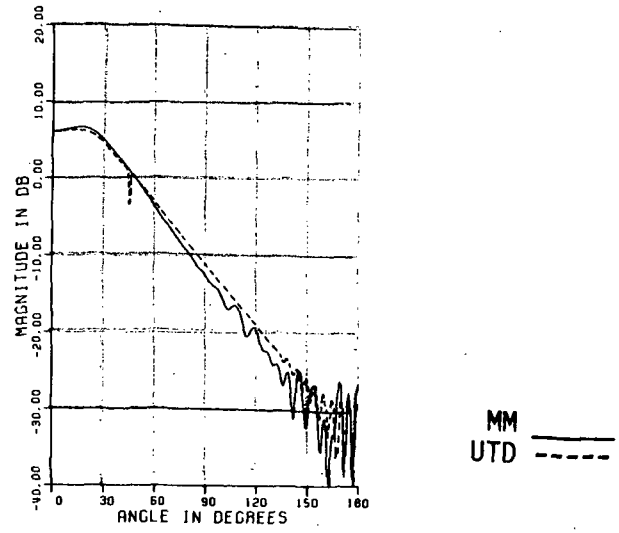

(d). E-plane field patterns for A_1 = 3.05 cm. VSWR = 1.04.

Figure 30. (Continued).

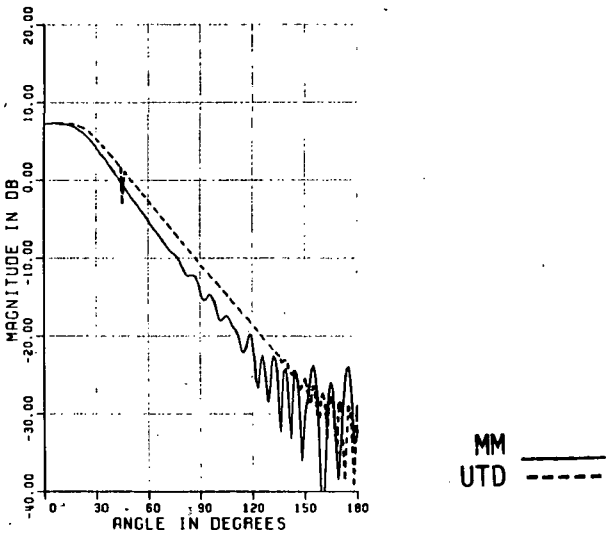

(e). E-plane field patterns for A_1 = 6.00 cm. VSWR = 1.03.

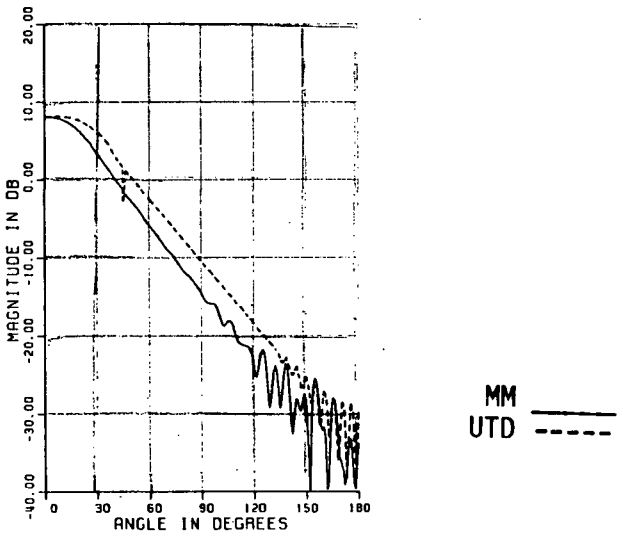

(f). E-plane field patterns for A_1 = 9.00 cm. VSWR = 1.02.

Figure 30. (Continued).

One possible explanation is suggested by the geometry shown in Figure 31. As A_1 increases with the other parameters remaining fixed, the length R_L of the straight sides of the horn decreases. The form of the modal expansion of the field across the circularly curved throat aperture assumes the region is bounded by an infinite two-dimensional wedge of angle 2α. However, as R_L becomes smaller, this approximation becomes less valid as the wedge structure vanishes. Also, note that as A_1 increases, the radius of curvature R_A of the throat aperture increases. Thus, the throat aperture is closer to the horn aperture. The diffracted fields from the rolled edge junctions may then need to be included in the field distribution across the throat aperture.

The effect of varying the radius of curvature A_2 of the rolled edge section is examined in Figure 32 using the moment method solution. The most noticeable change in the pattern as A_2 increases is a decrease in the level of the side lobes. In addition, the VSWR drops slightly. The UTD solution results are also shown in Figure 32 and agree well with the moment method solution for A_2 greater than one wavelength. However for smaller values of A_2, the UTD patterns exhibit a slight slope discontinuity at the shadow boundaries at 45° and 315°. The main beam of the UTD pattern disagrees with the moment method results, too. This behavior may be attributed to the low frequency limitations of the UTD diffraction coefficients.

Figure 33 illustrates the dependence of the pattern on the half-flare angle using the moment method approach. Clearly, as α increases, the width of the main beam increases. The calculated VSWR

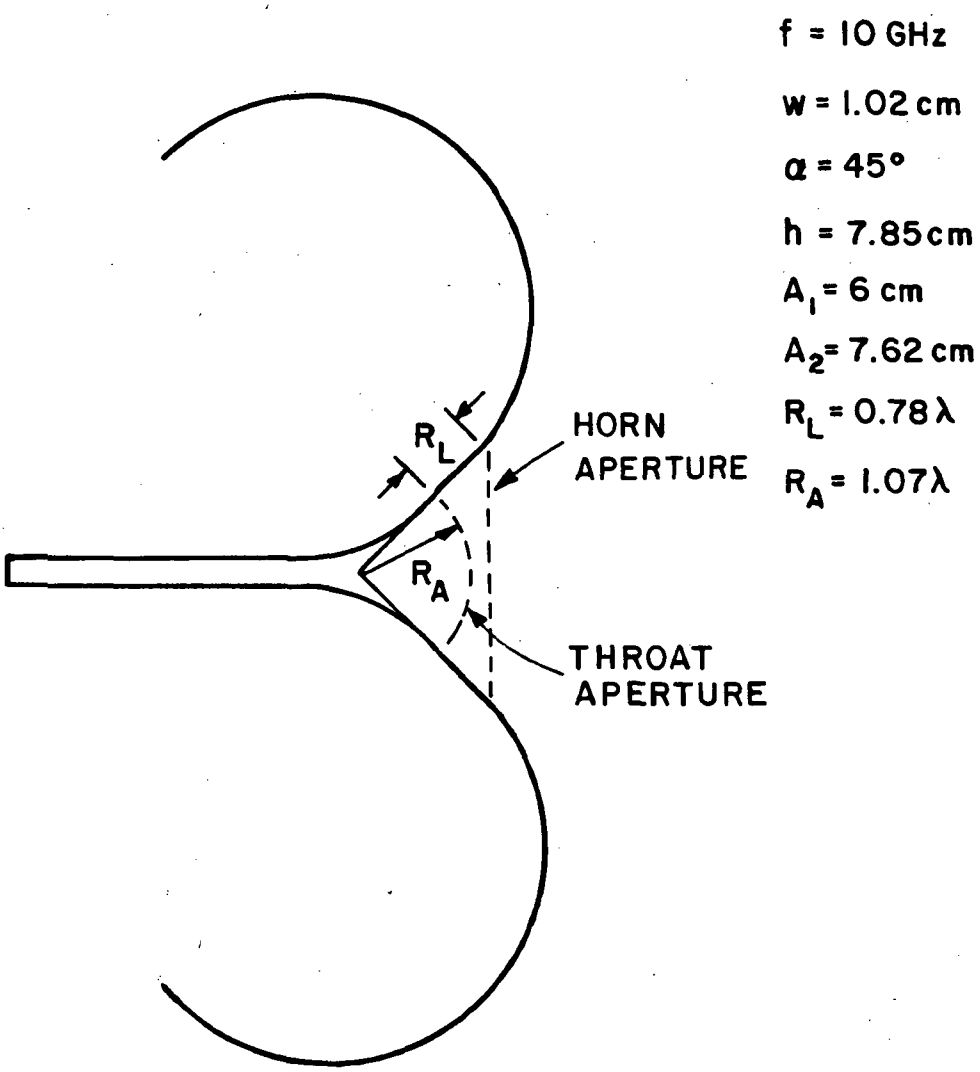

Figure 31. Aperture-matched horn geometry for a large value of the radius of curvature (A_1) of the throat section.

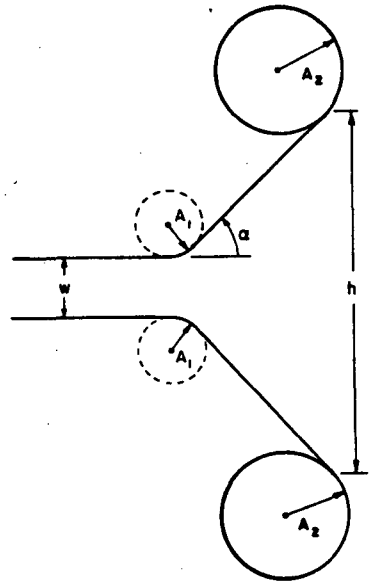

(a). Two-dimensional geometry for aperture-matched horn (E-plane). f = 10 GHz, w = 1.016 cm, α = 45°, h = 7.85 cm, A_1 = 3.05 cm, A_2 varies.

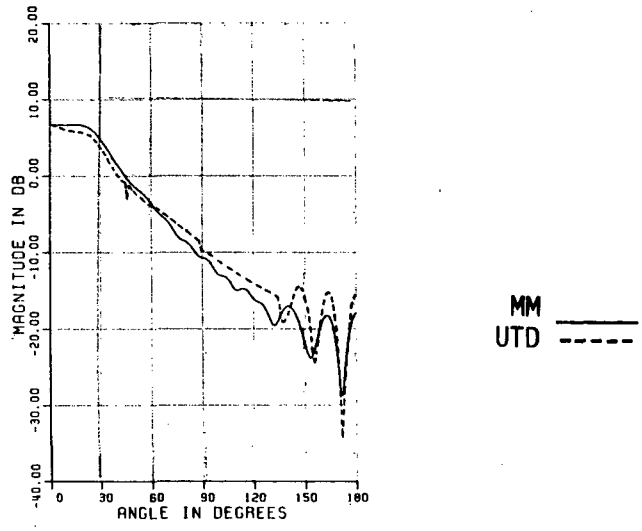

(b). E-plane field patterns for A_2 = 0.75 cm. VSWR = 1.05.

Figure 32. Moment method and UTD solutions for aperture-matched horn as the radius of curvature (A_2) of the rolled edge section is varied.

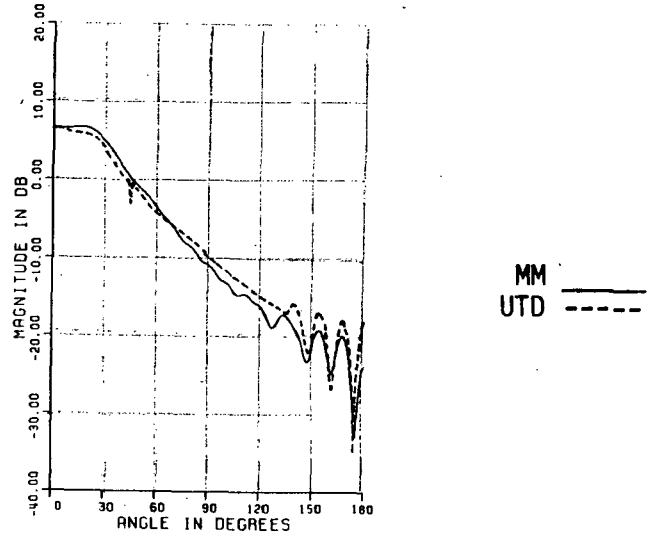

(c). E-plane field patterns for A_2 = 1.50 cm. VSWR = 1.04.

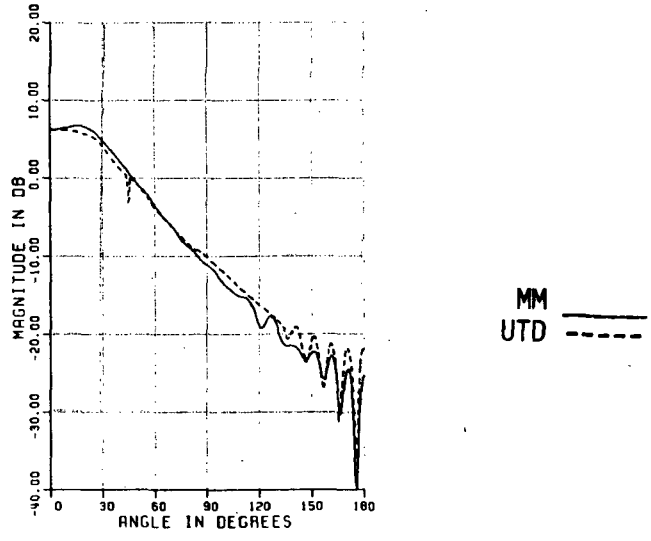

(d). E-plane field patterns for A_2 = 3.00 cm. VSWR = 1.04.

Figure 32. (Continued).

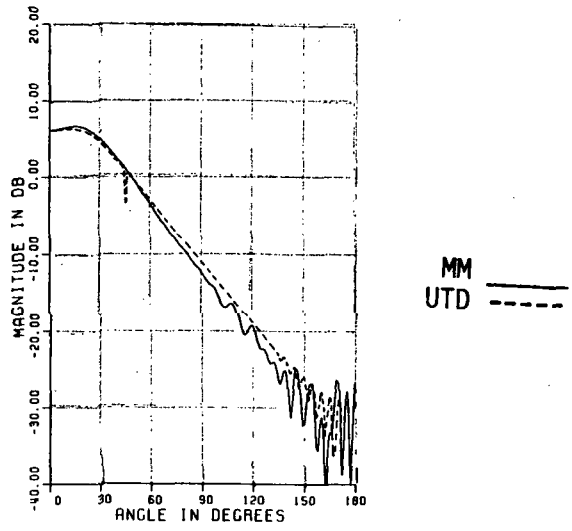

(e). E-plane field patterns for A_2 = 7.62 cm. VSWR = 1.04.

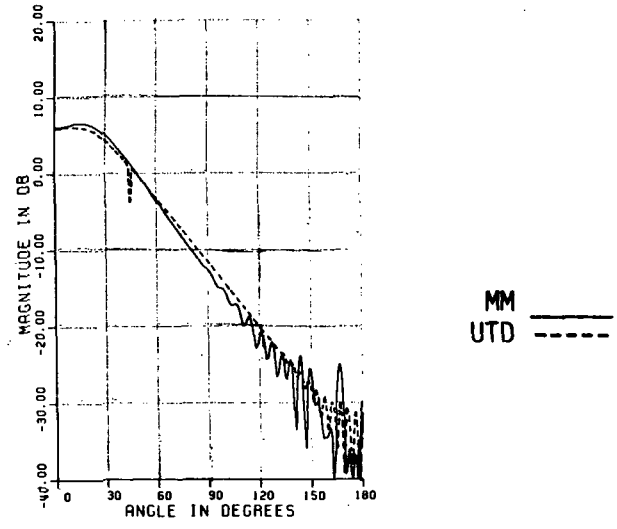

(f). E-plane field patterns for A_2 = 9.00 cm., VSWR = 1.04.

Figure 32. (Continued).

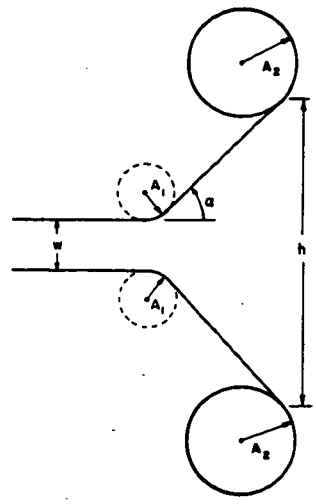

(a). Two-dimensional geometry for aperture-matched horn (E-plane). f = 10 GHz, w = 1.016 cm, h = 7.85 cm, A_1 = 3.05 cm, A_2 = 7.62 cm, α varies.

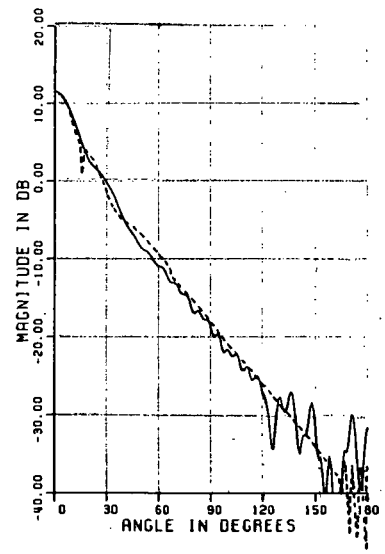

(b). E-plane field patterns for α = 15. VSWR = 1.07.

Figure 33. Moment method and UTD solutions for aperture-matched horn as the half-flare angle (α) is varied.

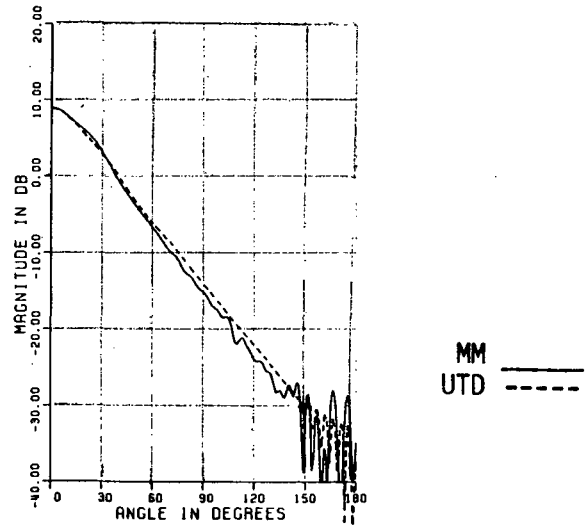

(c). E-plane field patterns for α = 30. VSWR = 1.03.

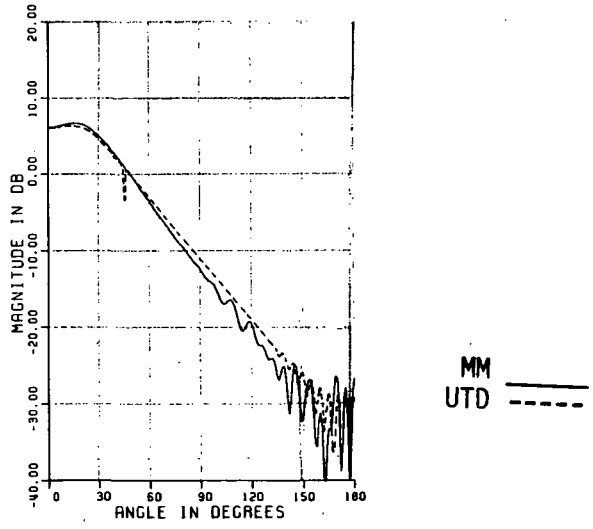

(d). E-plane field patterns for α = 45. VSWR = 1.04.

Figure 33. (Continued).

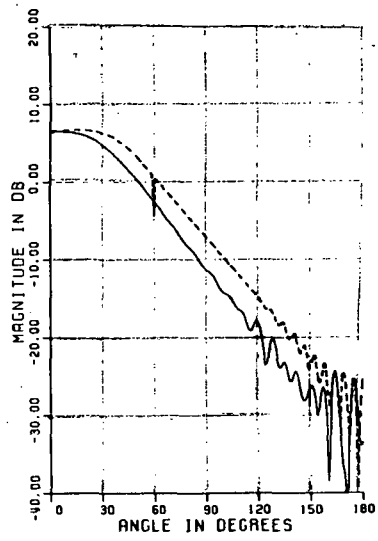

(e). E-plane field patterns for α = 60. VSWR = 1.03.

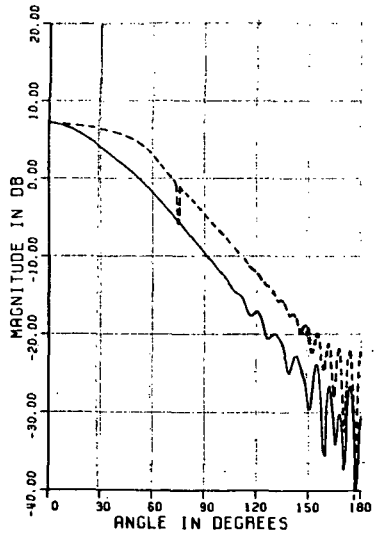

(f). E-plane field patterns for α = 75. VSWR = 1.03.

Figure 33. (Continued).

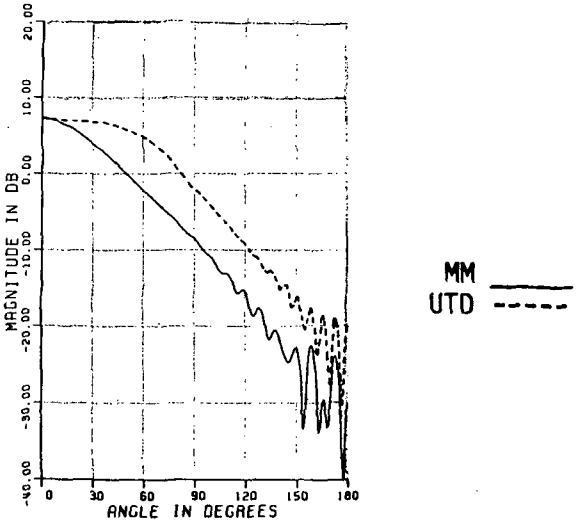

(g). E-plane field patterns for $\alpha = 90$. VSWR = 1.03.

Figure 33. (Continued).

remains relatively constant. The corresponding UTD results are also shown in Figure 33. The UTD solutions agree well with the moment method patterns for α less that 60°. However, for α = 60°, the UTD results begin to disagree with the moment method results. Since the aperture width is held constant, the length R_L of the straight sides of the horn decreases as α increases. Also, the curved throat aperture becomes closer to the horn aperture. Thus, the infinite wedge approximation breaks down again. Note that if both α and h were increased so that R_L did not decrease, the UTD solution would remain valid.

The moment method patterns shown in Figure 34 indicate that as h increases, the main beam exhibits a ripple. This is expected since a large aperture is likely to have a greater phase variation across it. The VSWR is relatively constant as h varies. The UTD patterns as h is varied are also shown in Figure 34. There is excellent agreement with the corresponding moment method results, except for h = 3 cm. For such small values of h, the length R_L of the straight sides of the horn is small so that the infinite wedge approximation is no longer valid.

As an example, consider the aperture-matched horn geometry shown in Figure 35. It represents the E-plane cross-sectional view of a horn which was actually designed for use in a compact range. The design requirements include a main beam which is relatively flat with less than 1 dB of variation within a 50° beamwidth. The backlobes must fall to approximately 40 dB below the maximum. The frequency range of operation is from 8 GHz to 12 GHz. In addition, a low VSWR is necessary since the same horn is used to transmit an incident field and receive the resulting scattered field.

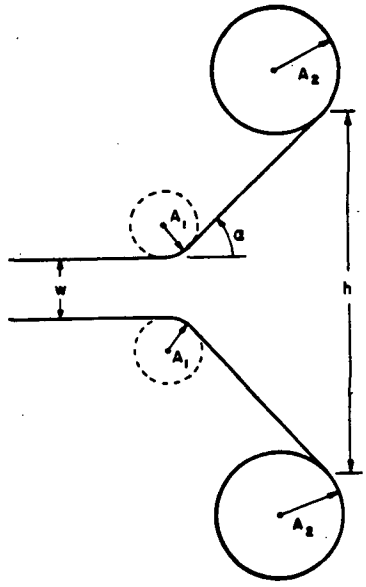

(a). Two-dimensional geometry for aperture-matched horn (E-plane). f = 10 GHz, w = 1.016 cm, α = 45°, A_1 = 3.05 cm, A_2 = 7.62 cm, h varies.

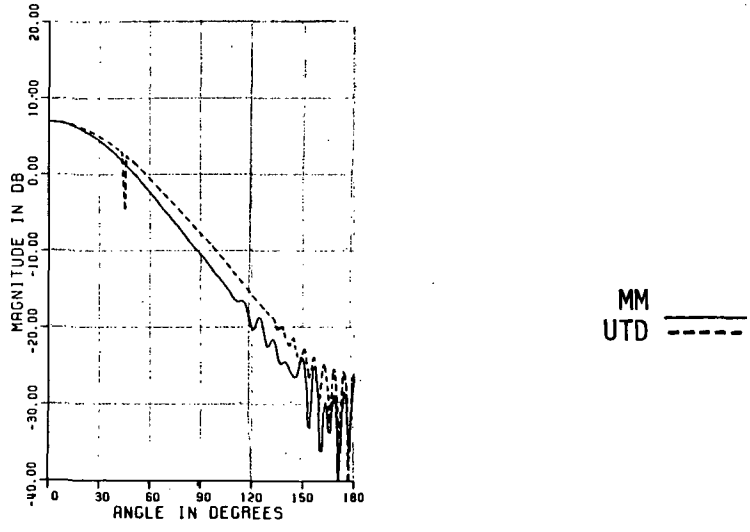

(b). E-plane field patterns for h = 3.00 cm. VSWR = 1.04.

Figure 34. Moment method and UTD solutions for aperture-matched horn as the aperture width (h) is varied.

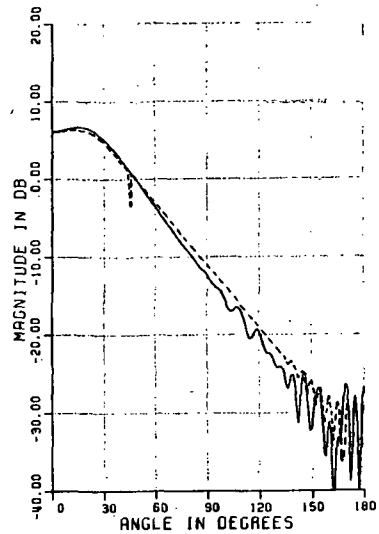

(c). E-plane field patterns for h = 7.85 cm. VSWR = 1.04.

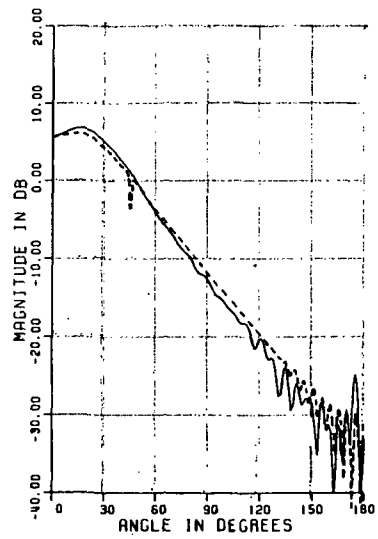

(d). E-plane field patterns for h = 9.00 cm. VSWR = 1.04.

Figure 34. (Continued).

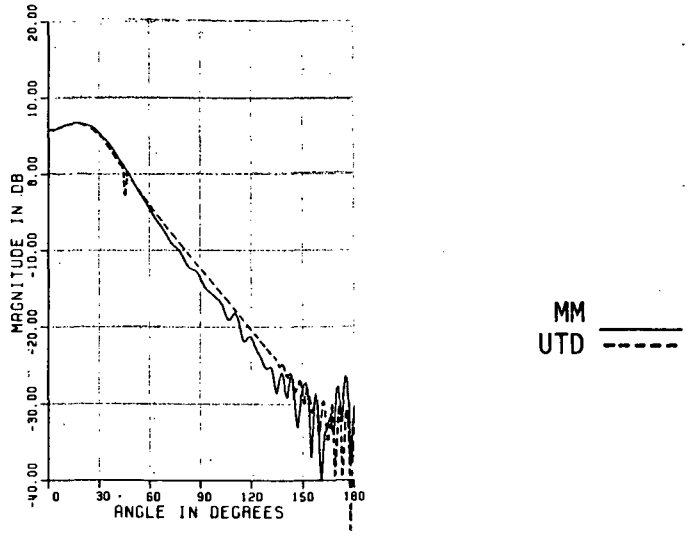

(e). E-plane field patterns for h = 12.00 cm. VSWR = 1.04.

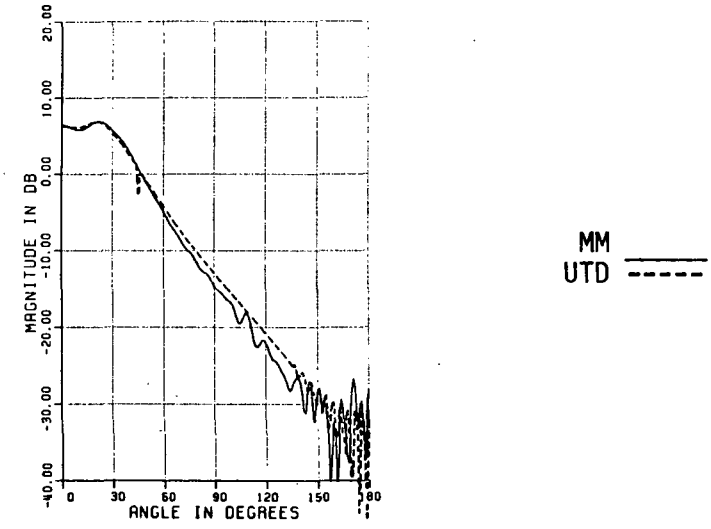

(f). E-plane field patterns for h = 15.00 cm. VSWR = 1.04.

Figure 34. (Continued).

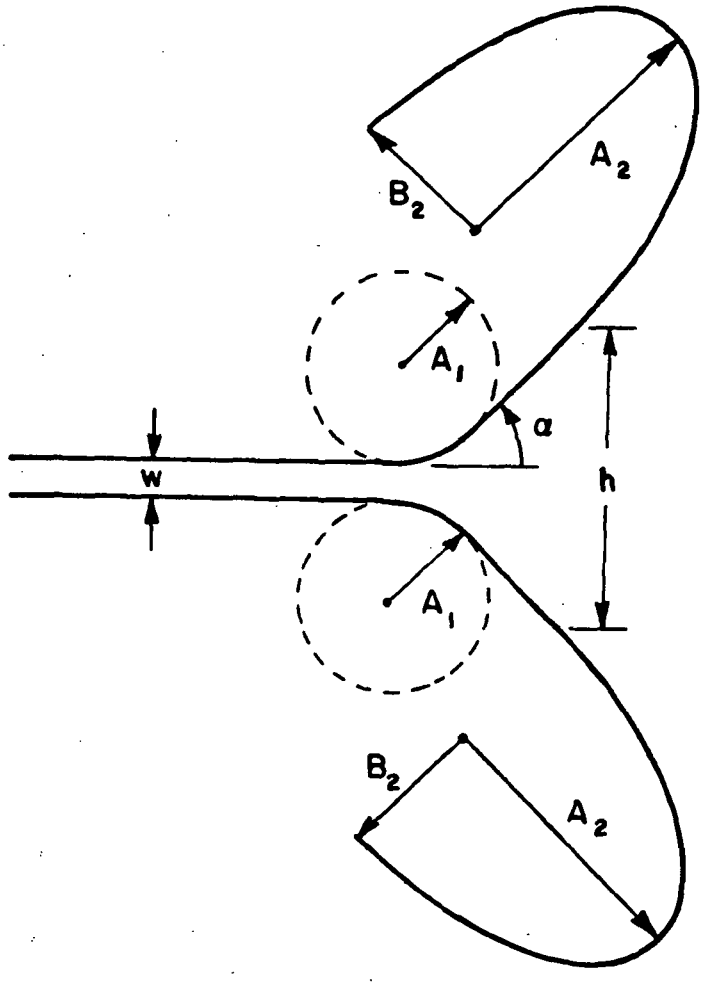

Figure 35. Compact range aperture-matched horn geometry (E-plane side view). w = 1.1016 cm, α = 45°, h = 7.8486 cm, A_1 = 3.048 cm, A_2 = 7.62 cm, B_2 = 3.81 cm.

The calculated and measured patterns are shown in Figure 36. The moment method results show excellent agreement with the measured patterns. The UTD solutions are within 1 dB of the measurements inside the flare angle of the horn, and they are well within 3 dB of the measurements out to the broadside direction. The discrepancies in the backlobes may be attributed to the inability to accurately model the structures feeding the horn. Also, higher order terms may be needed in the diffraction coefficient. In any case, both the UTD and the moment method solutions agree well with the measured patterns in the major regions of interest.

The measured VSWR of the horn is shown in Table 1. As indicated by the moment method solution, the VSWR is higher at the lower frequencies but excellent after about 9.5 GHz. The VSWR had to be traded off against the pattern requirements in that the rolled throat section was directly affecting the VSWR and main beam pattern. As the throat radius increased, the VSWR improved but the main beam pattern had too much taper. As a compromise, the throat radius was chosen to provide the pattern requirement which was much more critical in the design. One should note that a VSWR of 1.2 is typical of most traditional horn antennas, so these results still exceed the VSWR performance of most horn antennas.

Clearly, this design does satisfy the necessary specifications. At this point, however, an absorbing material was added to the rolled edges of the horn to further improve its performance.

Another property of interest for such a feed antenna is the phase of the field. It is very necessary to have a relatively constant phase across the main beam of the feed antenna. Figure 37 shows the measured phase for the compact range horn with the absorbing material on the rolled edges. Note that the phase remains relatively constant as a function of angle as well as frequency. This is characteristic of aperture-matched antennas since the main beam is dominated by the throat term.

In conclusion, the aperture-matched horn can be designed using these analytic techniques to provide uniform patterns across a wide beam width with low backlobes, low VSWR, a wide frequency response, and constant phase center.

TABLE 1

MEASURED VSWR VERSUS FREQUENCY FOR COMPACT RANGE APERTURE-MATCHED HORN ANTENNA WITH ABSORBING MATERIAL ON ROLLED EDGES

Frequency (GHz)	VSWR
8.0	1.16
8.5	1.12
9.0	1.08
9.5	1.04
10.0	1.02
10.5	1.03
11.0	1.04
11.5	1.03
12.0	1.04

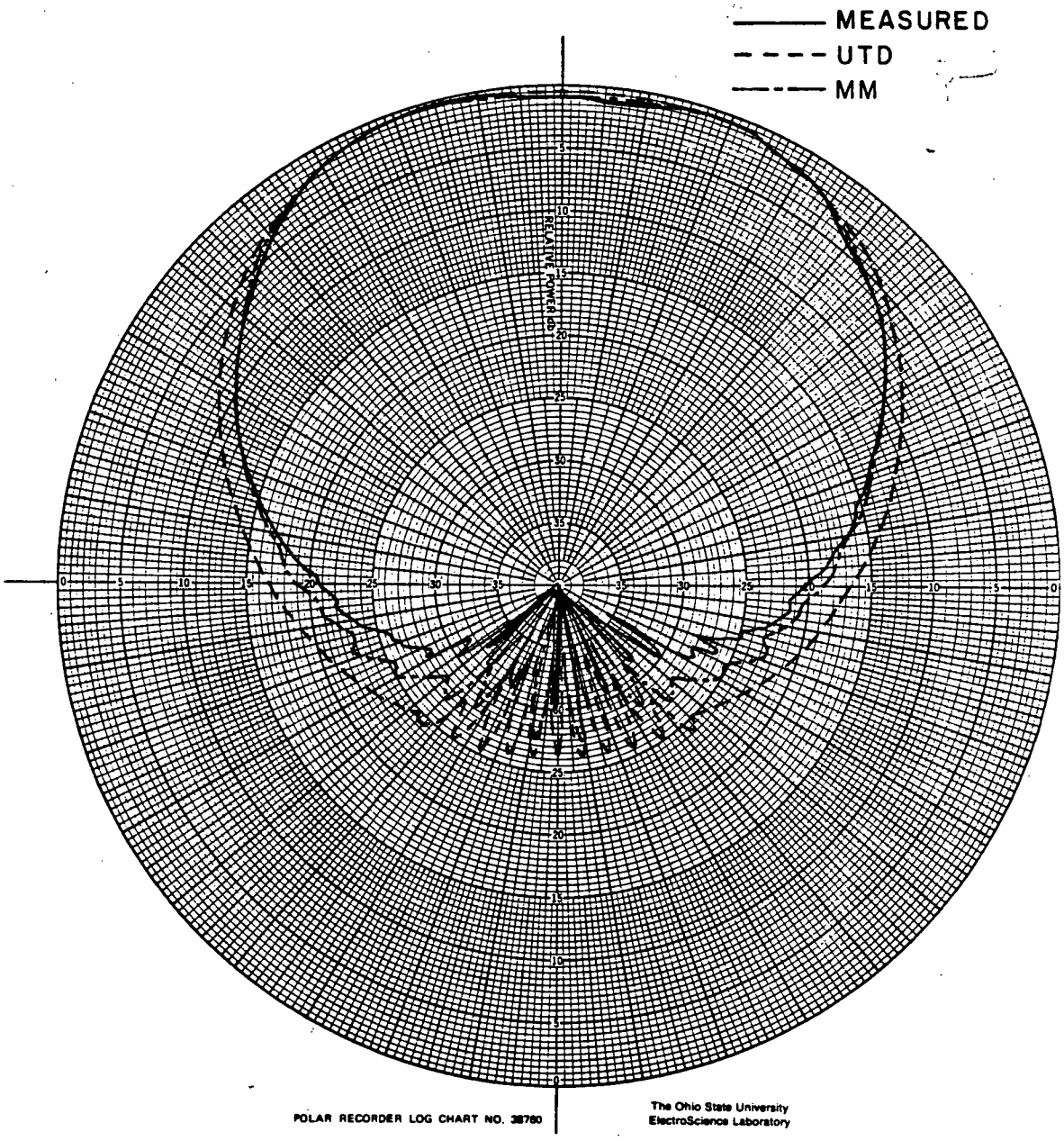

a. E-plane field patterns for f = 8 GHz.

Figure 36. Comparison of calculated and measured E-plane field patterns for compact range aperture-matched horn.

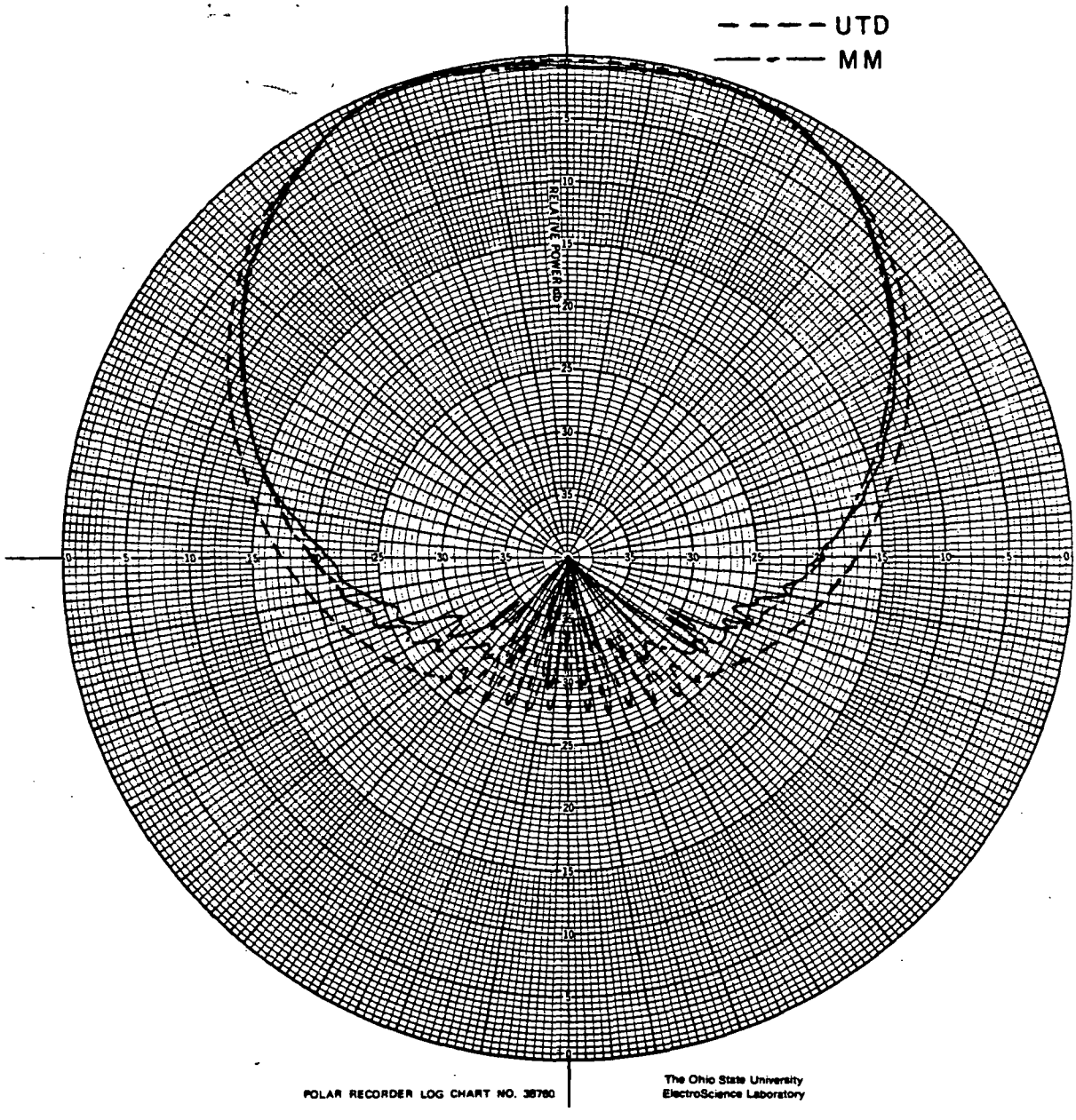

b. E-plane field patterns for f = 9 GHz.

Figure 36. (Continued).

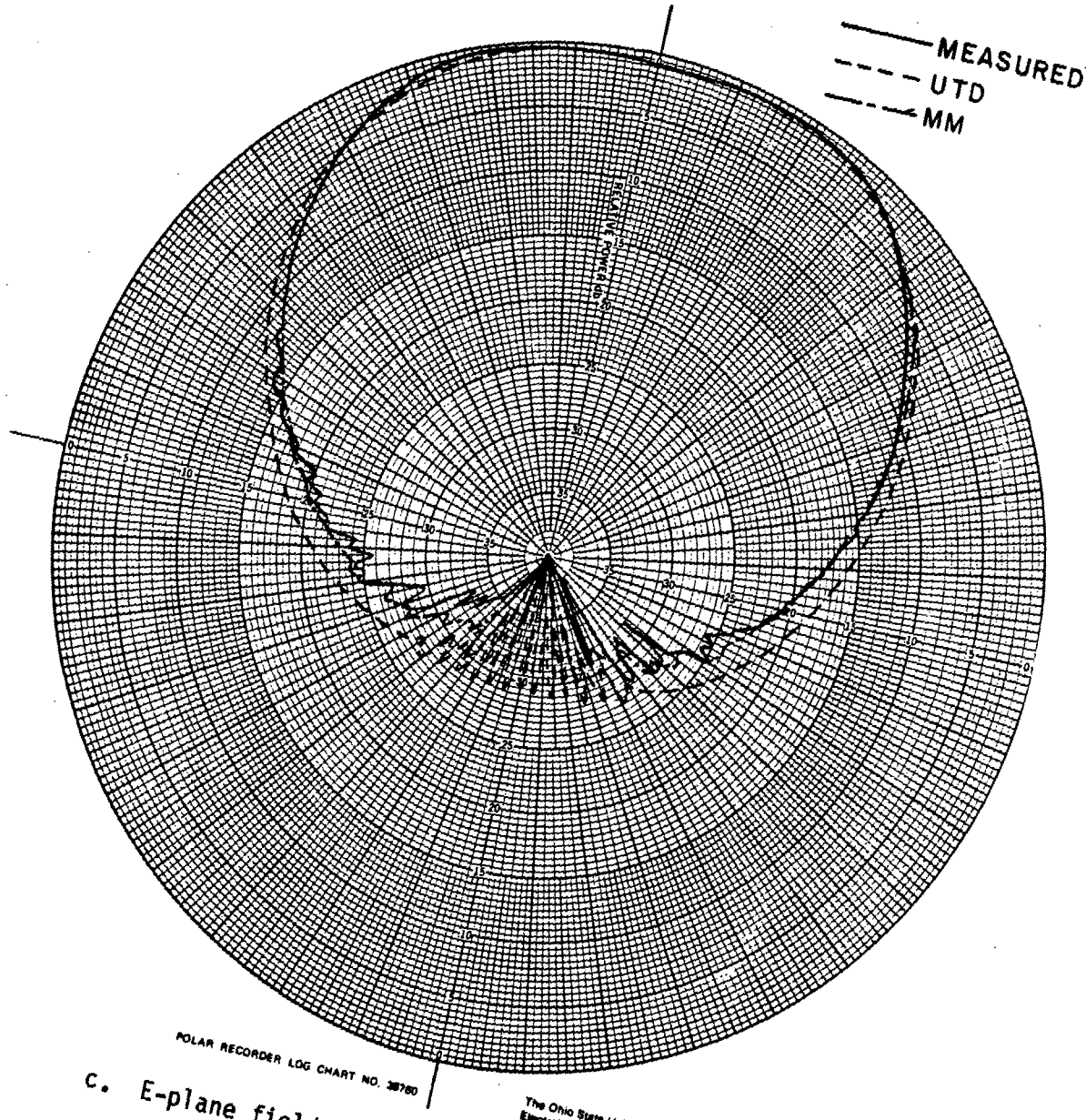

c. E-plane field patterns for f = 10 GHz.

Figure 36. (Continued).

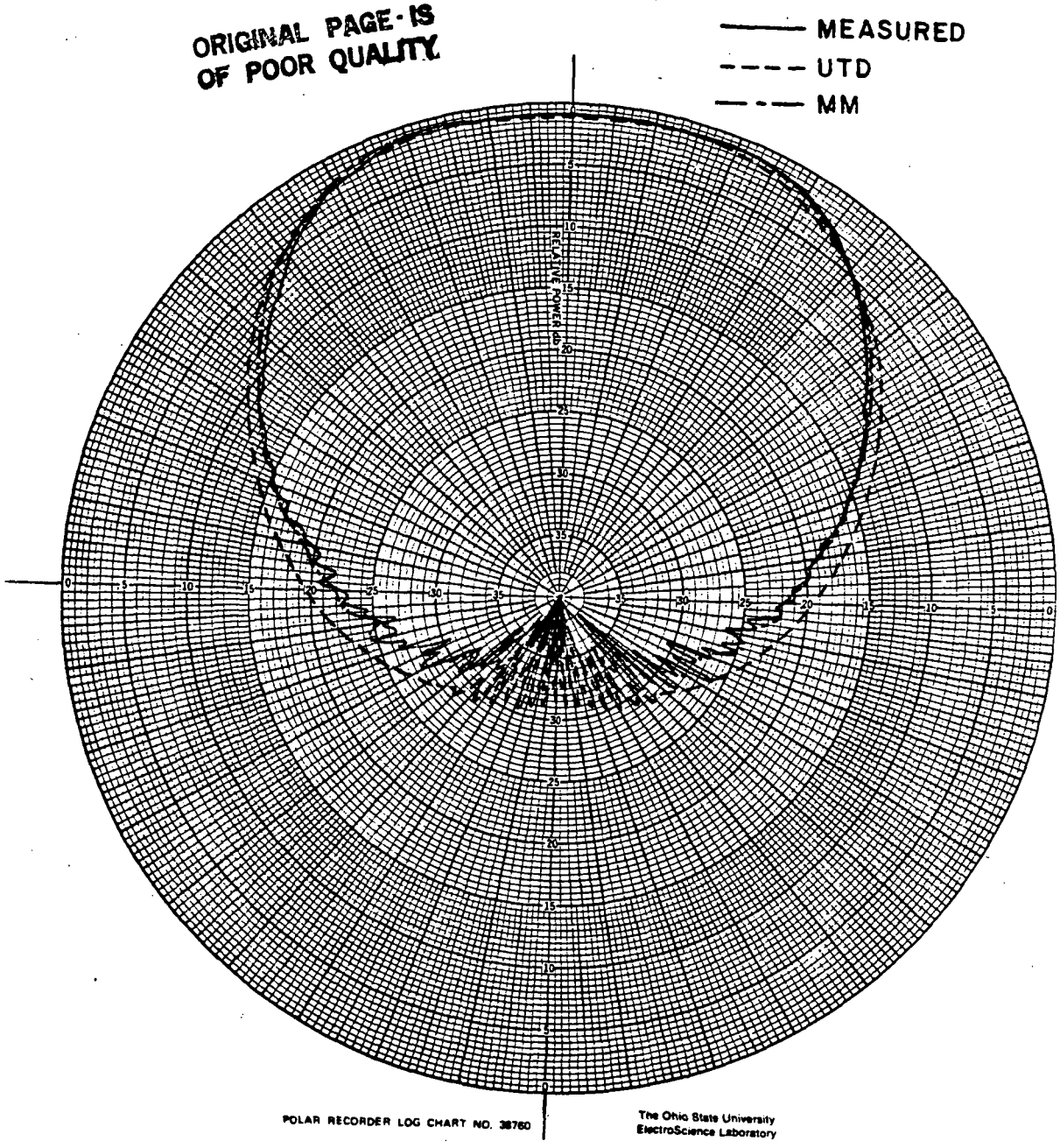

d. E-plane field patterns for f = 11 GHz.

Figure 36. (Continued).

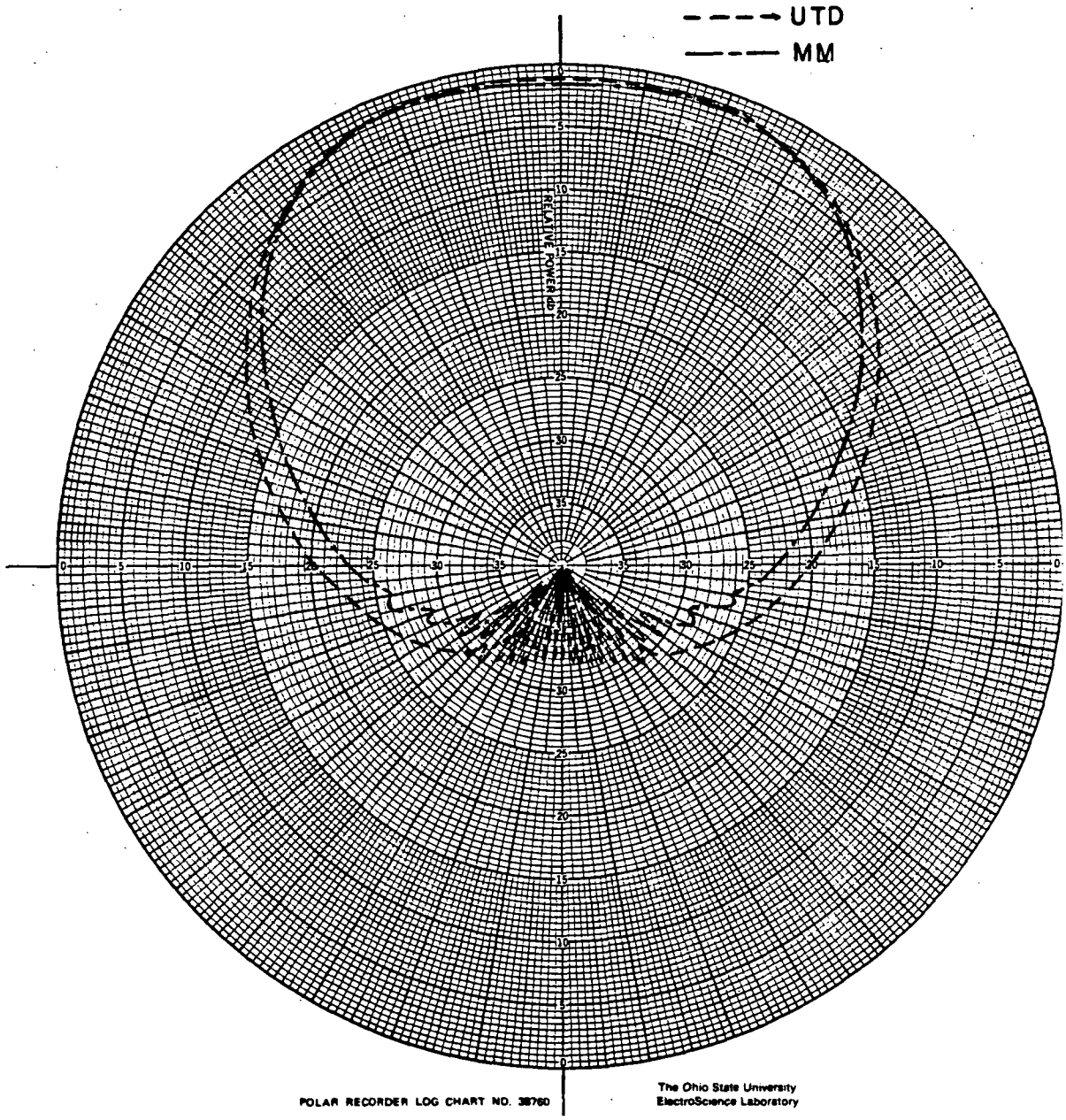

e. E-plane field patterns for f = 12 GHz.

Figure 36. (Continued).

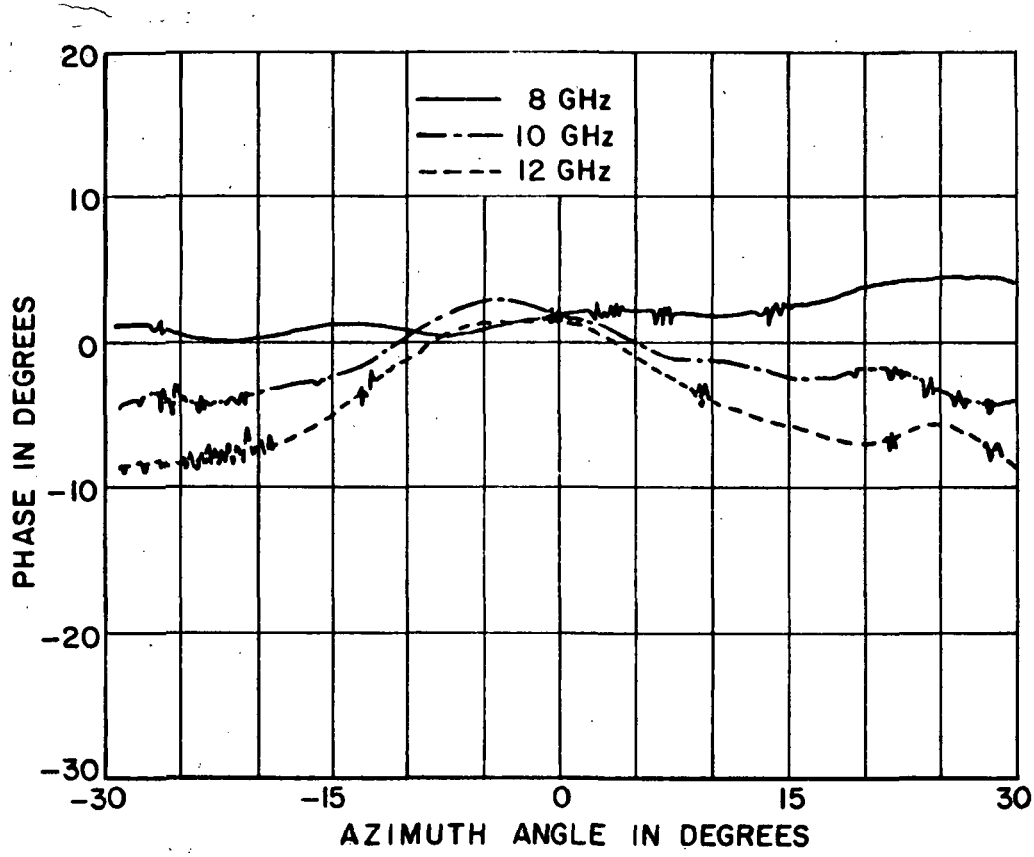

Figure 37. Measured phase versus azimuth angle for compact range aperture-matched horn with absorbing material on rolled edges.

CHAPTER V

SUMMARY AND CONCLUSIONS

In summary, an aperture-matched horn can be designed to have a broader main beam and lower side lobes than standard pyramidal horns. In addition, it has a lower VSWR. For certain applications, particularly for compact range feed antennas, these characteristics are essential.

Two methods for calculating the E-plane field pattern for such an aperture-matched horn were considered. In both approaches, the actual three-dimensional horn geometry was approximated by a two-dimensional geometry such that any coupling effects between the E- and H-planes are neglected.

Moment method techniques were used to calculate the field by solving an integral equation obtained from the reaction concept. The VSWR was determined from an internal field. In fact, this method gives accurate results provided one uses at least four current samples per wavelength. However, at high frequencies, the number of unknowns becomes large resulting in intolerably large amounts of computation time.

The UTD approach presented in this report helped overcome this problem. A diffraction coefficient for a source mounted on a pefectly conducting planar surface smoothly terminated by a circular cylinder was obtained. Using this coefficient, the field distribution across a curved aperture in the throat of the horn was calculated. Next, this distribution was expanded in a series of cylindrical modes. The resulting series provided the field incident from the throat of the horn such that UTD techniques could then be used to calculate the far field pattern. This method requires much less computation time than the moment method. However, the UTD is a high frequency technique; it fails at low frequencies where the horn dimensions are electrically small. At high frequencies, the UTD solution converges asymptotically to the exact solution. Specifically, a discrepancy occurs when the radius of curvature of the circular cylinder is less than one half of a wavelength. Also, there is a discrepancy when the distance from the source to the junction is less than 1.5 wavelengths.

Ordinarily, one would expect the UTD solution to be valid at even lower frequencies. The disagreement described above suggests that this UTD diffraction coefficient may be improved. Perhaps the addition of higher order terms may help the low frequency behavior. In any case, the diffraction coefficient obtained here works very well for electrically large horns.

The UTD solution also becomes inaccurate when the horn geometry loses its wedge-shaped appearance. Then the infinite wedge approximation used to obtain the modal expansion of the throat field breaks down. This occurs whenever the length R_L of the straight sides

of the horn becomes too small. When this happens, the curved throat aperture becomes very close to the planar horn aperture; in fact, it may even extend beyond the horn aperture.

Fortunately, the UTD approach works well for the type of geometry typically encountered in practice. For low frequencies where the UTD fails, the moment method approach is suitable. Together, the two methods may be used to efficiently design an aperture-matched horn to operate over a broad range of frequencies. It is suggested that the UTD be used to initially design the horn; then, the moment method should be used to "fine tune" the result in that it represents a more complete solution. On the other hand, one should beware when the moment method and UTD do not agree, particularly at high frequencies. It is entirely possible that the moment method is being applied in an incomplete sense such as a lack of current segments needed to realistically represent the horn geometry under test. At low frequencies, the UTD solution may be suspect, but then an accurate moment method solution would involve a relatively small number of unknowns and therefore little computation time. Together, the two methods allow one to quickly and efficiently design an aperture-matched horn.

This analytic approach was used to design an aperture-matched horn to feed a compact range measurement system. The requirements for this feed antenna were very stringent and necessitated many iterations on the computer. However, the desired performance has achieved based on experimental verification. In fact, the calculated results agreed very well with the prototype measurements. Thus, this design procedure has been sucessfully applied in this application.

APPENDIX A

EVALUATION OF THE DIFFRACTION COEFFICIENT FOR A SOURCE MOUNTED ON A PERFECTLY CONDUCTING PLANAR SURFACE SMOOTHLY TERMINATED BY A CIRCULAR CYLINDER

Consider only the hard case, i.e., the electric field transverse to the z-direction. The diffraction coefficient for a perfectly conducting two-dimensional surface with a discontinuity in surface curvature [12] is given by

$$D_h = \frac{e^{-j\pi/4}}{\sqrt{2\pi k}} \frac{C_h(\xi_1)F(X_1) - C_h(\xi_2)F(X_2)}{\cos\phi + \cos\phi'} \tag{A.1}$$

where

$$C_h(\xi_{1,2}) = \sqrt{\frac{2\cos(\frac{\phi-\phi'}{2})}{a_{1,2}}} \left[1/2\sqrt{\frac{L}{\pi X}}\, F(X) + m_{1,2}\sqrt{\frac{2}{k}}\, q^*(\xi_{1,2})\right] \cdot e^{-j\pi/4 - j(\xi_{1,2})^3/12} \tag{A.2}$$

$$\xi_{1,2} = -2m_{1,2}\cos(\frac{\phi-\phi'}{2}) \tag{A.3}$$

$$m_{1,2} = (1/2ka_{1,2})^{1/3} \tag{A.4}$$

$$L = \frac{ss'}{s + s'} \tag{A.5}$$

$$X = 2kL \cos^2 \left(\frac{\phi-\phi'}{2}\right) \tag{A.6}$$

$$X_{1,2} = \frac{ka_{1,2}(\cos\phi + \cos\phi')^2}{4\cos\left(\frac{\phi-\phi'}{2}\right)\left[1+\left(\frac{1}{s} + \frac{1}{s'}\right)\frac{a_{1,2}}{2}\cos\left(\frac{\phi-\phi'}{2}\right)\right]} \tag{A.7}$$

$$F(x) = 2j\sqrt{x}\, e^{jx} \int_{\sqrt{x}}^{\infty} e^{-jt^2} dt \tag{A.8}$$

$$q^*(\xi_{1,2}) = \frac{1}{\sqrt{\pi}} \int_{-\infty}^{\infty} \frac{V'(\tau)}{W_2'(\tau)} e^{-j\xi_{1,2}\tau} d\tau \tag{A.9}$$

in which $V(\tau)$ and $W_2(\tau)$ are the Fock type Airy functions given by

$$2jV(\tau) = W_1(\tau) - W_2(\tau) \quad ; \quad W_{\frac{1}{2}}(\tau) = \frac{1}{\sqrt{\pi}} \int_{\infty e^{\mp j2\pi/3}}^{\infty - j\varepsilon} e^{\tau t - t^3/3} dt \tag{A.10}$$

with ε being a positive number however small, and

$$V'(\tau) = \frac{\delta V(\tau)}{\delta \tau} \quad ; \quad W_2'(\tau) = \frac{\delta W_2(\tau)}{\delta \tau} \quad . \tag{A.11}$$

Consider the quantity $C_h(\xi_1)F(X_1)$ for the far field ($s \to \infty$) with plane wave incidence ($s' \to \infty$) as a_1 approaches infinity. Then

$$L \to \infty \tag{A.12}$$

$$X \to \infty \tag{A.13}$$

and

$$X_1 \to \infty \quad . \tag{A.14}$$

For large arguments, the transition function $F(X)$ approaches unity so that

$$F(X) \to 1 \tag{A.15}$$

and

$$F(X_1) \to 1 \quad . \tag{A.16}$$

For large negative arguments, the Pekeris function has the asymptotic form given by

$$q^*(x) \approx \frac{1}{2x\sqrt{\pi}} - 1/2 \quad \sqrt{|x|}\left(1 - \frac{j2}{x^3}\right) e^{-jx^3/12} \, e^{j\pi/4} \quad . \tag{A.17}$$

Thus for the far field with plane wave incidence, one obtains

$$\lim_{a_1\to\infty} C_h(\xi_1)F(X_1) = \lim_{a_1\to\infty} \left[\sqrt{\frac{2\cos\left(\frac{\phi-\phi'}{2}\right)}{a_1}} \left[\frac{1}{2\sqrt{2\pi k}\cos\left(\frac{\phi-\phi'}{2}\right)} \right. \right.$$

$$\left. - \frac{1}{2\sqrt{2\pi k}\cos\left(\frac{\phi-\phi'}{2}\right)} \sqrt{\frac{m_1^3\left|\cos\left(\frac{\phi-\phi'}{2}\right)\right|}{k}} \left[1 + \frac{j}{4m_1^3\cos^3\left(\frac{\phi-\phi'}{2}\right)} \right] \right]$$

$$\left. e^{j\xi_1^3/12}\, e^{j\pi/4} \right] \left[e^{-j\xi_1^3/12}\, e^{-j\pi/4} \right] \Bigg] = -\cos\left(\frac{\phi-\phi'}{2}\right) \quad . \tag{A.18}$$

This term may be modified for the general case, i.e., s and s' finite, by multiplying by the transition function $F(X_1)$ which takes into account the necessary range dependence. Also for grazing incidence ($\phi'=0$), the parameter X_1 is reduced by a factor of four to insure continuity at the shadow boundary.

Hence, in the lit region ($0<\phi<\pi$), the field for a source mounted on a perfectly conducting planar surface smoothly terminated by a circular cylinder is given by

$$\vec{H}(Q) = \hat{z}H^i(Q_J)D_h \frac{e^{-jks}}{\sqrt{s}} \tag{A.19}$$

where $H^i(Q_J)$ is the field incident on the junction at point Q_J, s is the distance from Q_J to the field point, and the appropriate diffraction coefficient is

$$D_h = \frac{-e^{-j\pi/4}}{\sqrt{2\pi k}} \frac{\cos\left(\frac{\phi-\phi'}{2}\right)F(X_1) + C_h(\xi_2)F(X_2)}{\cos\phi + \cos\phi'} \tag{A.20}$$

$$C_h(\xi_2) = \sqrt{\frac{2\cos\left(\frac{\phi-\phi'}{2}\right)}{a_2}} \left[1/2\sqrt{\frac{L}{\pi X}}\, F(X) + m_2\sqrt{\frac{2}{k}}\, q^*(\xi_2)\right] \cdot e^{-j\pi/4 - j(\xi_{1,2})^3/12} \tag{A.21}$$

$$\xi_2 = -2m_2 \cos\left(\frac{\phi-\phi'}{2}\right) \tag{A.22}$$

$$m_2 = (1/2ka_2)^{1/3} \tag{A.23}$$

$$L = \frac{ss'}{s + s'} \tag{A.24}$$

$$X = 2kL \cos^2\left(\frac{\phi-\phi'}{2}\right) \tag{A.25}$$

$$X_1 = \frac{kL(\cos\phi + \cos\phi')^2}{8\cos^2\left(\frac{\phi-\phi'}{2}\right)} \tag{A.26}$$

and

$$X_2 = \frac{ka_2\,(\cos\phi + \cos\phi')^2}{4\cos\left(\frac{\phi-\phi'}{2}\right)\left[1+\left(\frac{1}{s} + \frac{1}{s'}\right)\frac{a_2}{2}\cos\left(\frac{\phi-\phi'}{2}\right)\right]} \tag{A.27}$$

C-2

The functions F(x) and $q^*(x)$ are given in Equations (A.8) through (A.11). The geometry is shown in Figure 20.

In the shadow region ($\pi<\phi<2\pi$), there is no incident field, and the diffracted field is a creeping wave field. It can be described by the diffraction coefficient of Pathak, Burnside, and Marhefka [2] but needs to be multiplied by an appropriate constant which is chosen to insure field continuity at the shadow boundary. Hence, in the shadow region ($\pi<\phi<2\pi$), the field for a source mounted on a perfectly conducting planar surface smoothly terminated by a circular cylinder is given by

$$\vec{H}(Q) = \hat{z}H^i(Q_J)\ C\ \tau_h \frac{e^{-jks^d}}{\sqrt{s^d}} \tag{A.28}$$

where s^d is the distance from the creeping wave launch point Q_J to the field point and

$$\tau_h = m_2\ e^{-jkt}\sqrt{\frac{2}{k}}\left|\frac{F(\chi^d)}{2\xi\sqrt{\pi}} - q^*(\xi)\right|\ e^{-j\pi/4} \tag{A.29}$$

$$m_2 = (1/2ka_2)^{1/3} \tag{A.30}$$

$$t = a_2|\phi_2 - \phi_1| \tag{A.31}$$

$$\xi = \frac{m_2 t}{a_2} = m_2\ |\phi_2 - \phi_1| \tag{A.32}$$

$$\chi^d = \frac{ks'\ s^d}{s' + s^d}\frac{\xi^2}{2m_2^2} \tag{A.33}$$

The geometry is shown in Figure 21. The constant C is the ratio of the field $H_L(Q)$ in the lit region to the field $H_S(Q)$ in the shadow region, both evaluated at the shadow boundary SB such that

$$C = \frac{H_L(Q)}{H_S(Q)}\bigg|_{SB} = \frac{H^i(Q) + H^i(Q_J)D_h \frac{e^{-jks}}{\sqrt{s}}}{H^i(Q_J)\tau_h \frac{e^{-jks^d}}{\sqrt{s^d}}} \quad . \tag{A.34}$$

Clearly, as one approaches the shadow boundary,

$$H^i(Q_J)C\tau_h \frac{e^{-jks^d}}{\sqrt{s^d}} = \frac{H_L(Q)}{H_S(Q)}\bigg|_{SB} \quad H_S(Q) \rightarrow H_L(Q) = H^i(Q) + H^i(Q_J)D_h \frac{e^{-jks}}{\sqrt{s}} \tag{A.35}$$

and hence, the field is continuous.

The resulting diffraction coefficient for a source mounted on a perfectly conducting planar surface smoothly terminated by a circular cylinder is given by

$$D_{PC} = \begin{cases} \dfrac{-e^{-j\pi/4}}{\sqrt{2\pi k}} \dfrac{\cos\left(\frac{\phi-\phi'}{2}\right) F(X_1) + C_h(\xi_2)F(X_2)}{\cos\phi + \cos\phi'} & \text{in the lit region } (0<\phi<\pi) \\ \dfrac{H_L(Q)}{H_S(Q)}\bigg|_{Sb} m_2 e^{-ejkt} \sqrt{\dfrac{2}{k}} \left[\dfrac{F(X^d)}{\xi\sqrt{\pi}} - q^*(\xi)\right] e^{-j\pi/4} & \text{in the shadow region } (\pi<\phi<2\pi) \end{cases}$$

where the various parameters are as defined previously.

For suitable dimensions, the coefficient D_{pc} agrees quite well with the numerically derived diffraction coefficient of Burnside and Chuang [10] as shown in Figures A.1 and A.2. Note that both the magnitude and phase of the diffraction coefficients divided by the source distance s' are compared as both the cylinder radius a_2 and the source distance s' are varied. Clearly, the agreement is good for $a_2 > 0.5\lambda$ and $s' > 1.5\lambda$. For the dimensions typically encountered in an aperture-matched horn design, the diffraction coefficient D_{pc} is an excellent engineering approximation. Horns of smaller dimensions may be easily handled with the moment method.

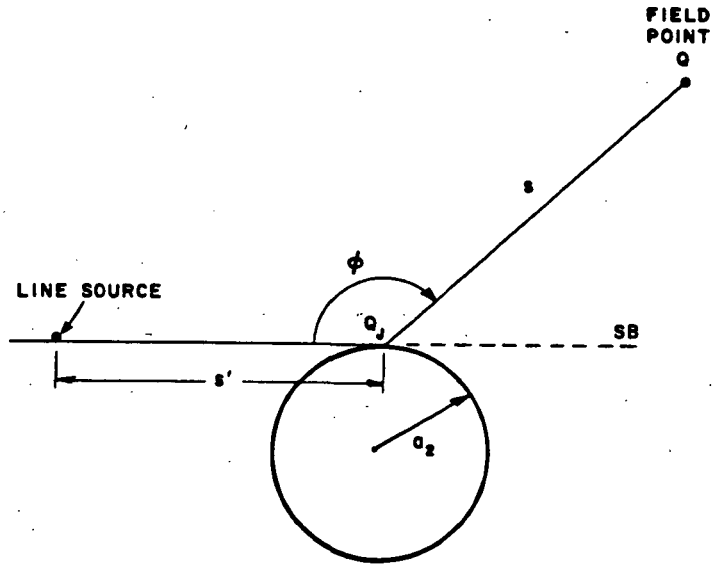

(a). Two-dimensional geometry. $s' = 3\lambda$.

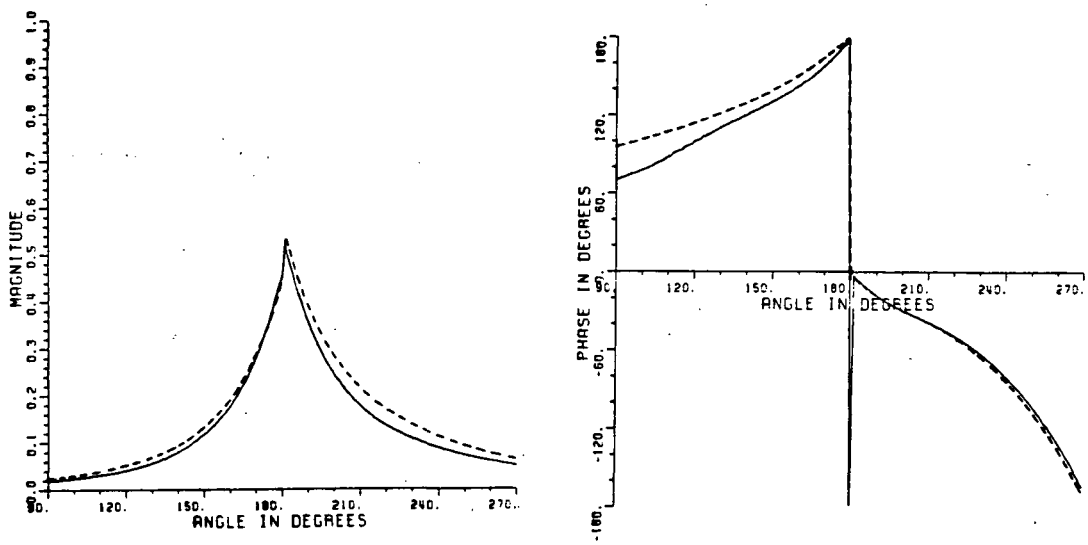

(b). Magnitude and phase of $D_{pc}/\sqrt{s'}$ for $a_2 = 0.5\lambda$.
(MM _____ and UTD -----.)

Figure A.1. Comparison of UTD diffraction coefficient and numerically derived diffraction coefficient of Burnside and Chuang as the radius of curvature (a_2) of the cylinder is varied.

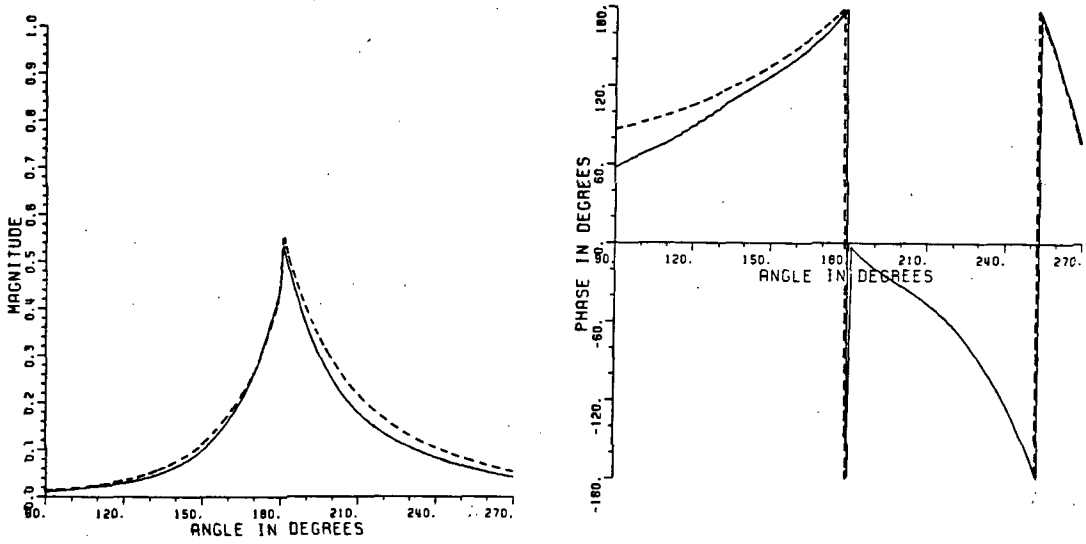

(c). Magnitude and phase of $D_{PC}/\sqrt{s^r}$ for $a_2 = 1.0\lambda$.
(MM _____ and UTD -----.)

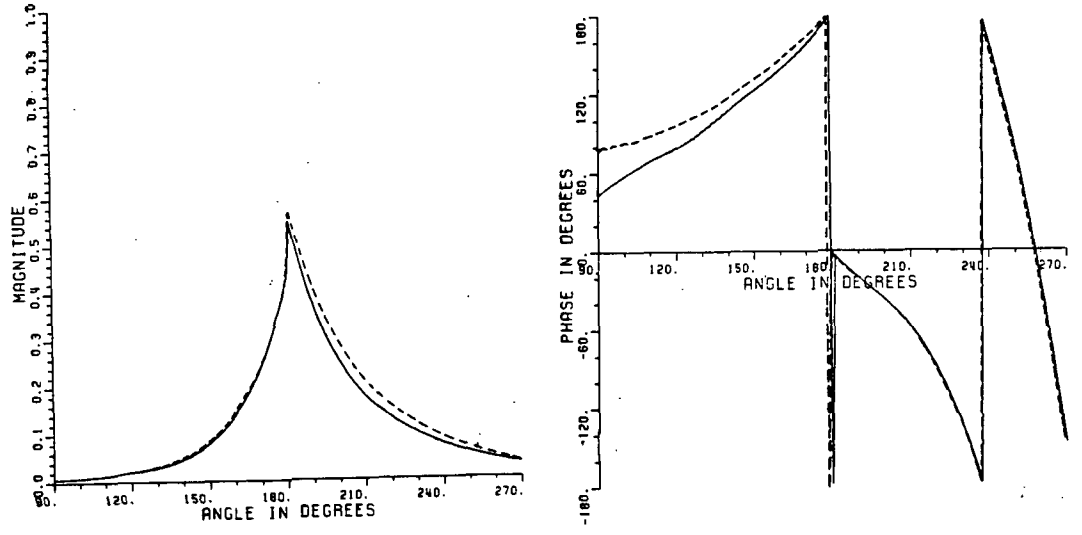

(d). Magnitude and phase of $D_{PC}/\sqrt{s^r}$ for $a_2 = 2.0\lambda$.
(MM _____ and UTD -----.)

Figure A.1. (Continued).

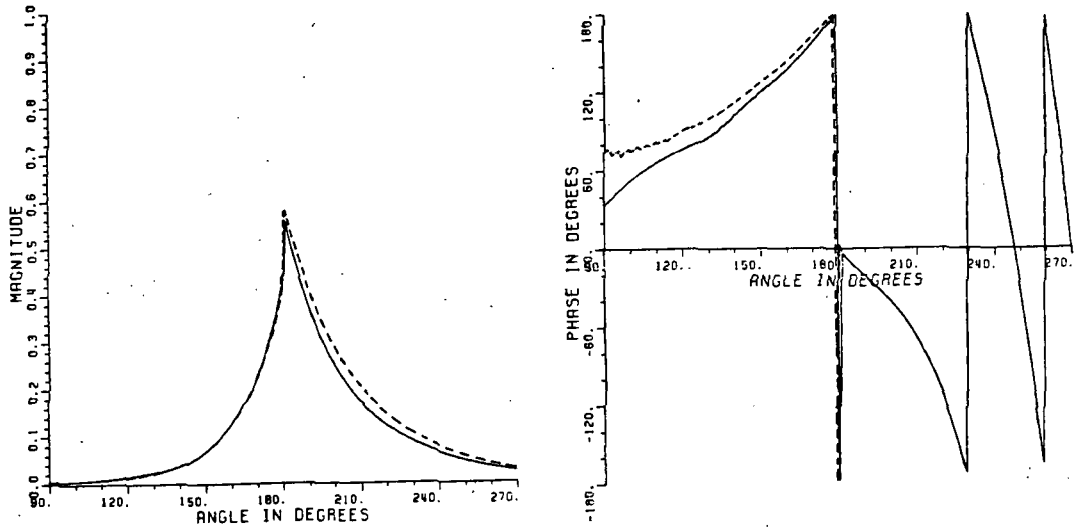

(e). Magnitude and phase of $D_{pc}/\sqrt{s^t}$ for $a_2 = 3.0\lambda$. (MM _____ and UTD -----.)

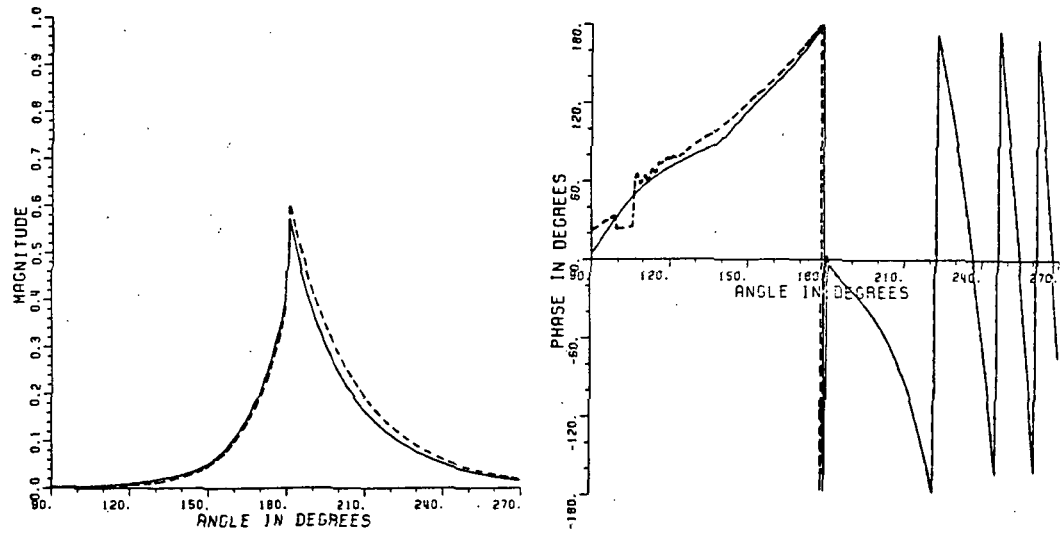

(f). Magnitude and phase of $D_{pc}/\sqrt{s^t}$ for $a_2 = 5.0\lambda$. (MM _____ and UTD -----.)

Figure A.1. (Continued).

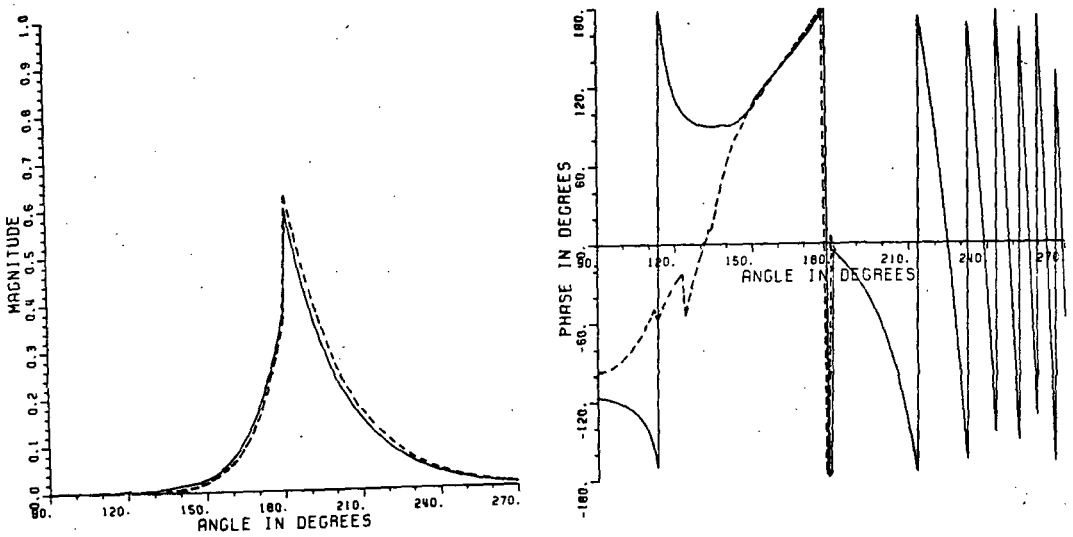

(g). Magnitude and phase of $D_{PC}/\sqrt{s^T}$ for $a_2 = 10.0\lambda$. (MM _____ and UTD -----.)

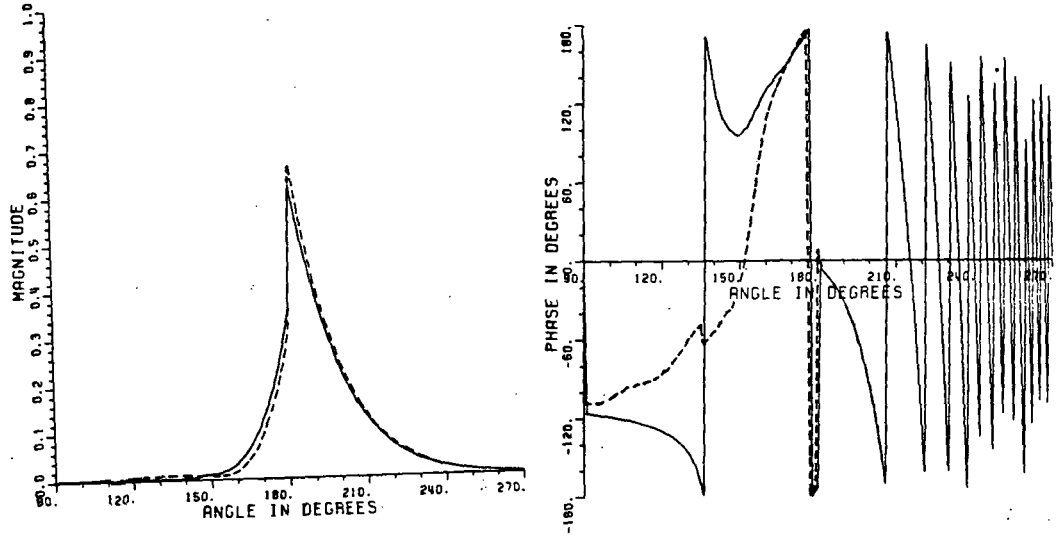

(h). Magnitude and phase of $D_{PC}/\sqrt{s^T}$ for $a_2 = 20.0\lambda$. (MM _____ and UTD -----.)

Figure A.1. (Continued).

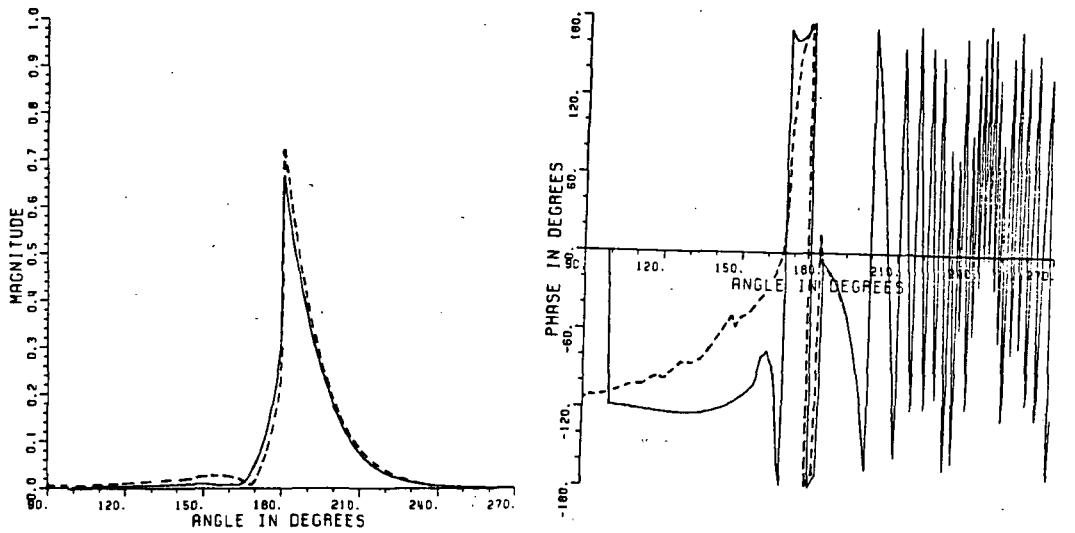

(i). Magnitude and phase of $D_{pc}/\sqrt{s^t}$ for $a_2 = 50.0\lambda$. (MM _____ and UTD -----.)

Figure A.1. (Continued).

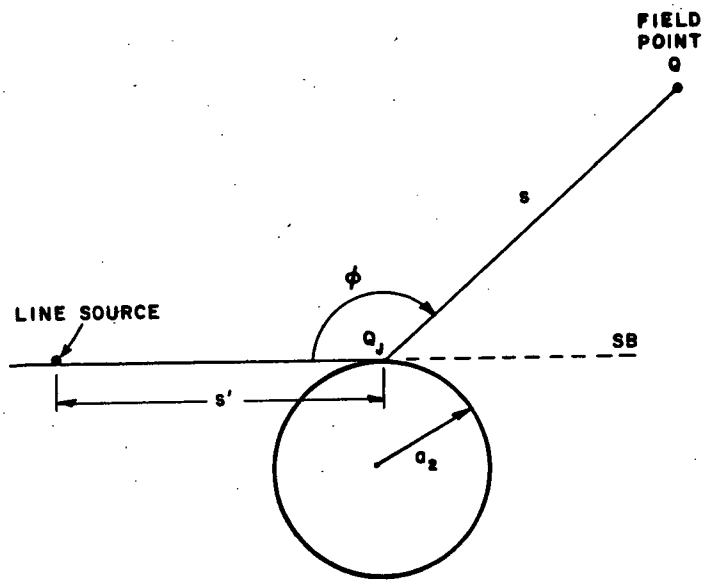

(a). Two-dimensional geometry. $a_2 = 3\lambda$.

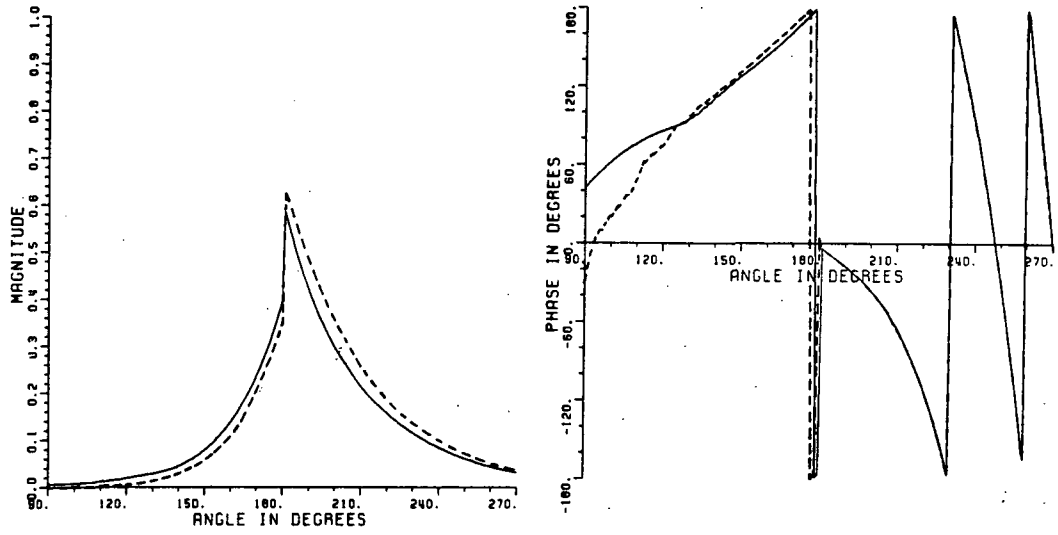

(b). Magnitude and phase of $D_{pc}/\sqrt{s'}$ for $s' = 1.5\lambda$.
(MM _____ and UTD -----.)

Figure A.2. Comparison of UTD diffraction coefficient and numerically derived diffraction coefficient of Burnside and Chuang as the source distance (s') is varied.

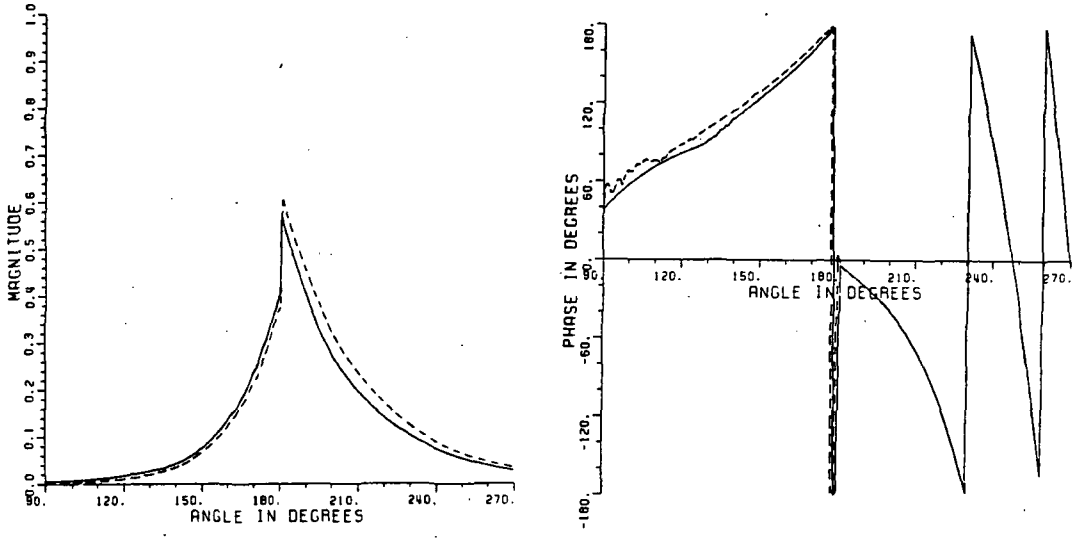

(c). Magnitude and phase of $D_{PC}/\sqrt{s'}$ for $s' = 1.0\lambda$. (MM _____ and UTD -----.)

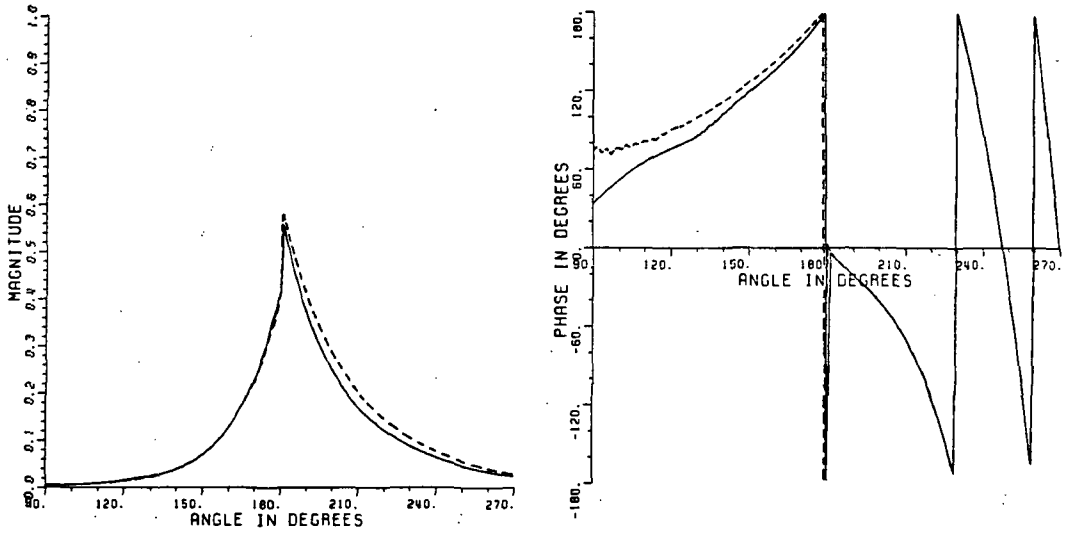

(d). Magnitude and phase of $D_{PC}/\sqrt{s'}$ for $s' = 2.0\lambda$. (MM _____ and UTD -----.)

Figure A.2. (Continued).

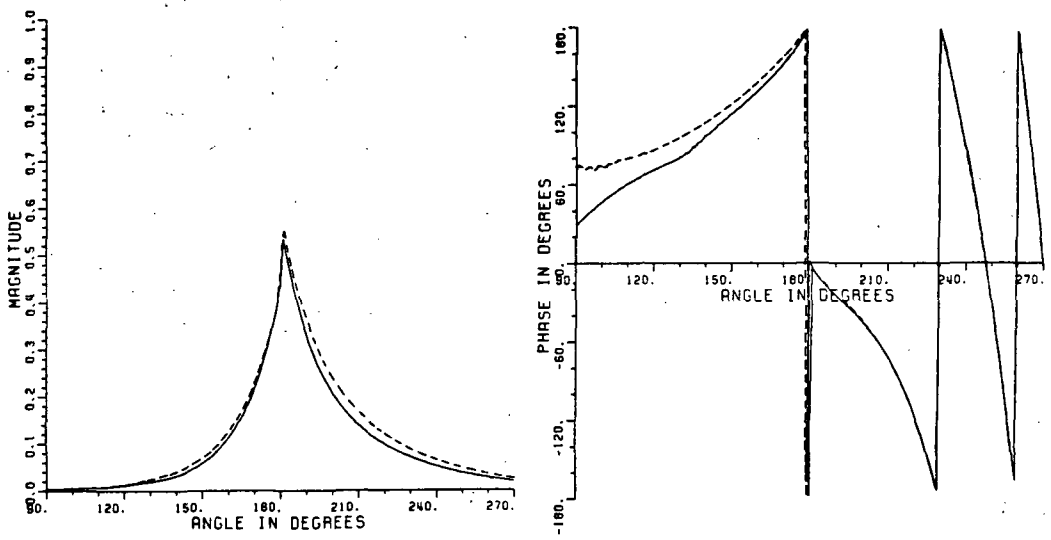

(e). Magnitude and phase of $D_{pc}/\sqrt{s'}$ for s' = 3.0λ.
(MM _____ and UTD -----.)

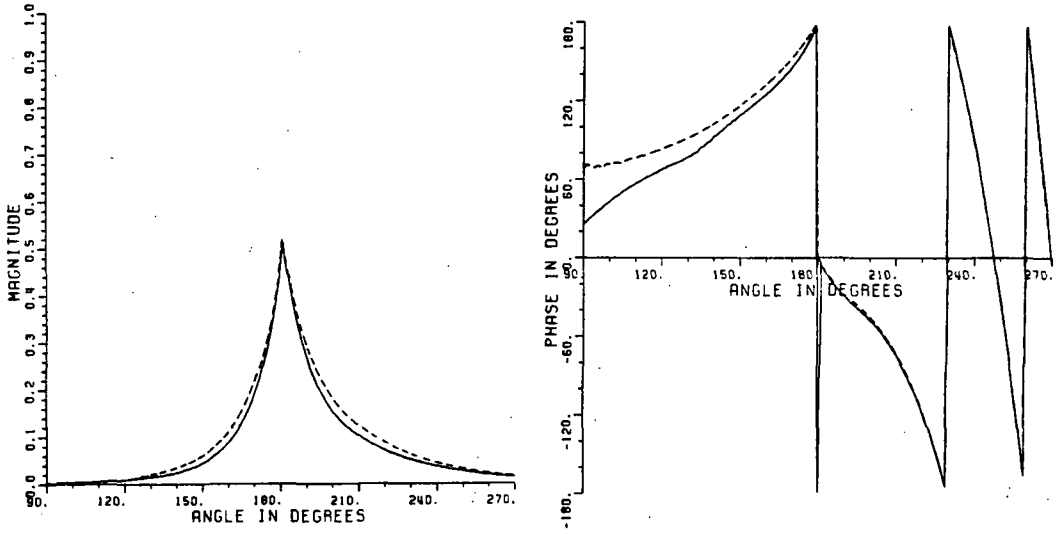

(f). Magnitude and phase of $D_{pc}/\sqrt{s'}$ for s' = 5.0λ.
(MM _____ and UTD -----.)

Figure A.2. (Continued).

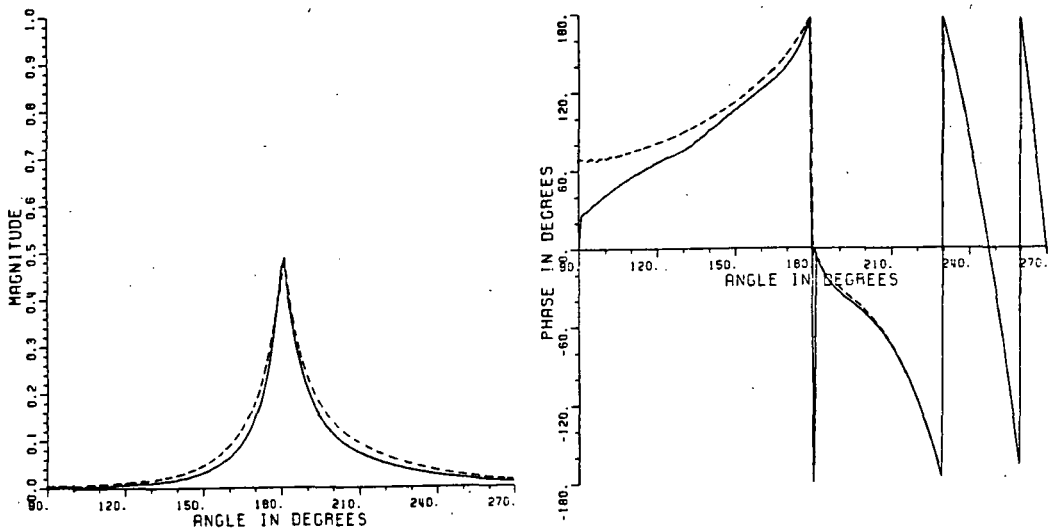

(g). Magnitude and phase of $D_{PC}/\sqrt{s'}$ for s' = 10.0λ. (MM _____ and UTD -----.)

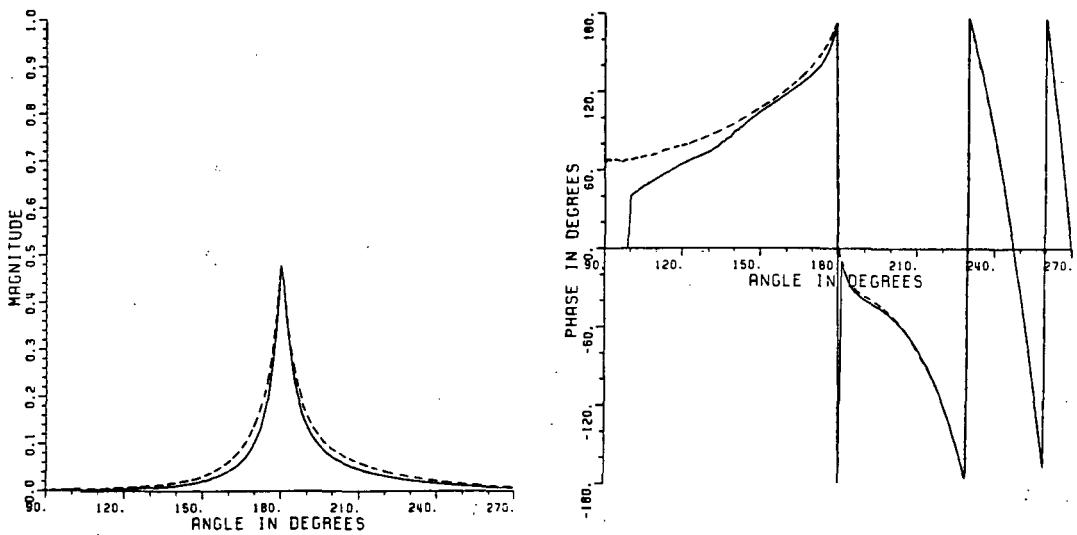

(h). Magnitude and phase of $D_{PC}/\sqrt{s'}$ for s' = 20.0λ. (MM _____ and UTD -----.)

Figure A.2. (Continued).

REFERENCES

[1] Pathak, P.H. and R.G. Kouyoumjian, "The Dyadic Diffraction Coefficient for a Perfectly Conducting Wedge", Report 2183-4, June 1980, The Ohio State University ElectroScience Laboratory, Department of Electrical Engineering; prepared under Contract AF19(628) - 5929 for Air Force Cambridge Research Laboratories.

[2] Pathak, P.H., W.D. Burnside, and R.J. Marhefka, "A Uniform GTD Analysis of the Diffraction of Electromagnetic Waves by a Smooth Convex Surface", IEEE Trans. on Antennas and Propagation, Vol. AP-28, No. 5, September 1980.

[3] Veruttipong, T., "Diffraction at Edges and Convex Surfaces Illuminated by Fields with a Rapid Spatial Variational", Ph.D. Dissertation, The Ohio Sate University ElectroScience Laboratory, Department of Electrical Engineering, Columbus, Ohio, 1982.

[4] Russo, P.M., R.C. Rudduck, and L. Peters, Jr., "A Method for Computing E-Plane Patterns of Horn Antennas", IEEE Trans. on Antennas and Propagation, Vol. AP-13, No. 2, March 1965.

[5] Yu, J.S., R.C. Rudduck and L. Peters, Jr., "Comprehensive Analysis for E-Plane of Horn Antennas for Edge Diffraction Theory", IEEE Trans. on Antennas and Propagation, Vol. AP-14, March 1966.

[6] Yu, J.S. and R.C. Rudduck, "H-Plane Pattern of a Pyramidal Horn", IEEE Trans. on Antennas and Propagation, Vol. AP-17, No. 5, September 1969.

[7] Rumsey, V.H., "Reaction Concept in Electromagnetic Theory", Physical Review, Vol. 94, June 15, 1954, pp. 1483-1491.

[8] Schellkunoff, S.A., "On Diffraction and Radiation of Electromagnetic Waves", Physical Review, Vol. 56, August 15, 1939.

[9] Richmond, J.H., "An Integral-Equation Solution for TE Radiation and Scattering from Conducting Cylinders", Report 2902-7, October 1972, The Ohio State University ElectroScience Laboratory, Department of Electrical Engineering; prepared under Grant NGL 36-008-138 for National Aeronautics and Space Administration Langley Research Center.

[10] Chuang, C.W. and W.D. Burnside, "A Diffraction Coefficient for a Cylindrically Truncated Planar Surface", IEEE Trans. on Antennas and Propagation, Vol. AP-28, No. 2, March 1980.

[11] Burnside, W.D. and C.W. Chuang, "An Aperture-Matched Horn Design", IEEE Trans. on Antennas and Propagation, Vol. AP-30, No. 4, July 1982.

[12] Pathak, P.H., C.D. Chuang, and S. Shrikanth, "Diffraction by a Perfectly Conducting Surface with a Discontinuity in Surface Curvature", Joint Services Electronics Program, Fifth Annual Report 710816-12, The Ohio State University ElectroScience Laboratory, Department of Electrical Engineering; prepared under Contract N00014-78-C-0049 for Department of Navy, Office of Naval Research.